TECHNISCHE
UNIVERSITÄT
WIEN
Vienna University of Technology

Diploma Thesis

Further development of measurement methods for the robust determination of climatic conditions in rail vehicles under consideration of the occurring environmental influences

carried out for the purpose of obtaining the degree of Diplom-Ingenieur (Dipl.-Ing.),

submitted at TU Wien

Faculty of Mechanical and Industrial Engineering

by

Florian Kerschbaumer, BSc

Mat.No.: 12022469

under the supervision of

Privatdoz. Dipl.-Ing. Dr.techn. Christoph Reichl,

Institute of Fluid Mechanics and Heat Transfer, E322

Petra Pilz, MSc and

Rail Tec Arsenal

Nico Umlauf

Rail Tec Arsenal

April, 2025

Affidavit

I, Florian Kerschbaumer, BSc, hereby declare under oath:

1. I have authored this master thesis independently and have not used any sources or aids other than those referenced and acknowledged within the thesis.
2. All data, figures, and concepts presented in this thesis are the results of my own work and research unless otherwise stated. Any assistance received in the completion of this work has been acknowledged in the thesis.
3. This thesis has not been submitted, either in whole or in part, for any other academic degree at this or any other institution.
4. I have acknowledged all sources of information in compliance with academic standards and have ensured that no content plagiarizes any previous work.
5. I utilized Artificial Intelligence to improve the language and clarity of my writing. The AI tools used were applied solely for the purpose of enhancing the readability and precision of the text, without altering the content or the original ideas presented in the thesis.
6. I am aware that any false declaration may result in consequences as per the regulations of the university.

_____   _____
(Place, Date)   (Signature)

Acknowledgements

I would like to express my sincere gratitude to my thesis supervisor, Privatdoz. Dipl.-Ing. Dr.techn. Christoph Reichl, for giving me the opportunity to work on this topic. Your feedback and continuous support during our weekly meetings have been crucial in shaping this thesis.

I am also deeply grateful to Rail Tec Arsenal for the opportunity to contribute to the improvement of this globally unique facility. Special thanks go to my colleagues at Rail Tec Arsenal for their engaging discussions and assistance in conducting the experiments, in particular Petra Pilz, MSc, and Nico Umlauf for their warm welcome, constant support, and constructive feedback during the experimental setup. Their expertise and collaboration were crucial to the success of this work. It was truly a pleasure to work with such a team.

Finally, I would like to thank my family for their support throughout my studies and for allowing me to pursue my academic journey. I would also like to thank my fellow students and friends for making my time at university an unforgettable and enriching experience. Without all of you, the successful and timely completion of my studies would not have been possible.

Abstract

Rail transport in Europe, particularly in Austria, will play a central role in the decarbonization of the transportation sector in the coming years. To facilitate this transition, an expansion of rail services and the commissioning of new railway vehicles are necessary. During the acceptance process of railway vehicles by operators, the thermal comfort of passengers, which is largely influenced by HVAC systems, is a crucial factor. This comfort is assessed under conditions that closely replicate real-world scenarios in the climatic wind tunnel of the Rail Tec Arsenal. To determine comfort parameters, sensors are used to measure air temperature, surface temperature, relative humidity, CO_2 concentration, and airflow velocities, which are subjected to the same climatic conditions as passengers.

This thesis focuses on investigating the potential impact of these climatic conditions on the sensors used. Relevant standards governing the test conditions for long-distance railway vehicles (EN 13129) and the measurement of physical parameters in ambient environments (ISO 7726) are analysed regarding specific requirements for minimizing environmental influences on sensor performance.

A combination of experimental investigations and CFD simulations showed a significant impact of solar radiation on temperature sensors. As a result, new sensor designs were developed and tested for their effectiveness on railway vehicles in the climatic wind tunnel.

Further investigations revealed a substantial influence of solar radiation on humidity sensors. To mitigate this effect, a radiation shield was designed that minimizes the effect without introducing unwanted side effects. In contrast, no influence of solar radiation on the measurement of CO_2 concentration in the air could be detected.

Additionally, the effect of temperature sensors placed near an anemometer on velocity measurements was investigated. The impact of different sensor sizes was confirmed.

A partial influence of temperature on the measurement of airflow velocity was observed.

This thesis outlines specific measures that can be implemented to reduce climatic influences on measurement sensors. Finally, further potential investigations are proposed.

Kurzfassung

Der Schienenverkehr in Europa, insbesondere in Österreich, wird in den kommenden Jahren eine zentrale Rolle bei der Dekarbonisierung des Verkehrssektors einnehmen. Um diesem Wandel gerecht zu werden, ist eine Erweiterung des Schienenangebots sowie die Indienststellung neuer Schienenfahrzeuge erforderlich. Bei der Abnahme von Schienenfahrzeugen durch die Betreiber spielt der thermische Komfort der Fahrgäste durch die HVAC Systeme eine entscheidende Rolle. Dieser wird unter möglichst realitätsnahen Bedingungen im Klima-Windkanal des Rail Tec Arsenal überprüft. Zur Erfassung der Behaglichkeitsparameter kommen Sensoren zur Messung der Lufttemperatur, der Oberflächentemperatur, der relativen Luftfeuchte, des CO_2-Gehalts sowie der Strömungs- geschwindigkeiten zum Einsatz, welche den selben klimatischen Bedingungen wie die Fahrgäste ausgesetzt sind.

Diese Arbeit widmet sich der Untersuchung der potenziellen Auswirkungen dieser klimatischen Bedingungen auf die verwendeten Sensoren. Dazu werden die relevanten Normen zur Festlegung der Testbedingungen für Schienenfahrzeuge im Fernverkehr (EN 13129) sowie für die Messung physikalischer Größen im Umgebungsklima (ISO 7726) hinsichtlich spezifischer Vorgaben zur Minderung von Umgebungseinflüssen auf die Sensorik analysiert.

Durch eine Kombination aus experimentellen Untersuchungen und CFD-Simulationen konnte ein deutlicher Einfluss der solaren Strahlung auf die Temperatursensoren nachgewiesen werden. Infolgedessen wurden neue Sensorkonzepte entwickelt und im Klima-Windkanal an Schienenfahrzeugen auf ihre Wirksamkeit hin überprüft.

Weitere Untersuchungen zeigten einen signifikanten Einfluss der solaren Strahlung auf die Feuchtesensoren. Zur Reduktion dieses Effekts wurde ein Strahlungsschutz entworfen, der die Störeinflüsse minimiert, jedoch keine anderen unerwünschten Nebeneffekte hat. Im Gegensatz dazu konnte kein Einfluss der solaren Strahlung auf die Messung des CO_2-Gehalts der Luft festgestellt werden.

Zusätzlich wurde der Einfluss von Temperatursensoren in der Nähe eines Strömungsanemometers auf die Geschwindigkeitsmessung untersucht. Der Unterschied verschieden großer Sensoren konnte nachgewiesen werden.

Ein Einfluss der Temperatur auf die Messung der Strömungsgeschwindigkeit konnte teilweise nachgewiesen werden

Diese Arbeit zeigt, welche konkreten Maßnahmen zur Verringerung der klimatischen Einflüsse auf die Messsensoren gemacht werden können. Abschließend werden weitere potenzielle Ansätze zur Untersuchung vorgeschlagen.

Contents

List of Figures

List of Tables

Nomenclature

Roman symbols

$\boldsymbol{I}$	unit tensor	1
$\dot{q}$	heat flux density	$\mathrm{W/m^2}$
$\dot{Q}_{\mathrm{gen}}$	source term	$\mathrm{W/m^3}$
$\boldsymbol{x}$	direction vector	m
a	thermal diffusivity	$\mathrm{m^2/s}$
c	speed of light, $c \approx 2.9979 \times 10^8\,\mathrm{m/s}$	m/s
c_p	specific heat capacity	$\mathrm{J\,kg^{-1}K^{-1}}$
E	total energy	J
g	gravitational constant, $g \approx 9.81\,\mathrm{m/s^2}$	$\mathrm{m/s^2}$
h	Planck's constant, $h \approx 6.6261 \times 10^{-34}\,\mathrm{J\,s}$	J s
h	specific enthalpy	J/kg
I	spectral intensity	$\mathrm{W/m^2}$
k	Boltzmann's constant, $k \approx 1.3806 \times 10^{-23}\,\mathrm{J/K}$	J/K
$K_{a\lambda}$	absorption coefficient	1
$K_{s\lambda}$	scattering coefficient	1
L	characteristic length scale	m
p	pressure	Pa
Q_{12}	heat transported from state 1 to 2	J
T	temperature	°C
t	time	s
t_a	ambient temperature	°C
U	inner energy	J
v	velocity	m/s
W_{12}	work done during state 1 to 2	J

Greek symbols

α	absorption coefficient	1
α	heat transfer coefficient	$\mathrm{W\,m^{-2}K^{-1}}$
β	thermal expansion coefficient	$1/\mathrm{K}$
$\boldsymbol{\tau}$	viscous stress tensor	Pa
ϵ	emissivity coefficient	1
λ	thermal conductivity	$\mathrm{W\,m^{-1}K^{-1}}$
λ	wavelength	m
ν	frequency	$1/\mathrm{s}$
ν	kinematic viscosity	$\mathrm{N\,s\,m^{-2}}$
Φ	phase function	1
ρ	density	$\mathrm{kg/m^3}$
ρ	reflective coefficient	1
σ	Stefan-Boltzmann constant, $\sigma \approx 5.67 \times 10^{-8}\,\mathrm{W\,m^{-2}K^{-4}}$	$\mathrm{W\,m^{-2}K^{-4}}$
τ	transmittance coefficient	1
$\boldsymbol{\Omega}$	direction vector	m
$\boldsymbol{\Omega}'$	direction vector	m

Indices

λ	wavelength dependent
ν	frequency dependent
a	absorbing
e	emitting
W	wall

Dimensionless numbers

Gr	Grashof number
Nu	Nusselt number
Pr	Prandtl number
Ra	Rayleigh number
Re	Reynolds number

Abbreviations

CFD   Computational Fluid Dynamics

CWT   Climatic Wind Tunnel

DNS   Direct Numerical Simulation

DO   Discrete Ordinates

FEM   Finite Element Method

FVM   Finite Volume Method

HVAC   Heating, Ventilation and Air Conditioning

LWT   Large Wind Tunnel

MP   Measurement position

RTA   Rail Tec Arsenal

RTE   Radiative Transport Equation

SWT   Small Wind Tunnel

1. Introduction

The transportation sector is one of the largest contributors to global greenhouse gas emissions, accounting for approximately 25% of the total CO_2 emissions worldwide [1]. As global climate change continues to intensify, an urgent shift away from fossil fuels toward more sustainable modes of transportation is needed. Railways, with their energy efficiency and primary reliance on electrified systems, represent one of the most environmentally friendly options and can play a crucial role in achieving national and international climate goals.

In Europe, particularly in Austria, the railway sector has gained significant attention due to its potential to reduce CO_2 emissions and support the transition to a low-carbon economy. A crucial aspect of improving the sustainability of rail systems is the optimization of climate control systems within trains, such as Heating, Ventilation and Air Conditioning (HVAC). These systems, which directly impact energy consumption and passenger comfort, can account for up to 20% to 40% of the total energy used by trains [2]. Consequently, optimizing HVAC performance under varying operating conditions represents a key objective for railway vehicle operators.

However, the optimization process is complex due to many influencing factors, including ambient temperature, humidity, airflow velocity, passenger load, and solar radiation. At the same time, passenger comfort should not be affected, making the use of real-life tests performed under controlled conditions essential. Such testing can be carried out in the Vienna Climatic Wind Tunnel (CWT), with the Rail Tec Arsenal (RTA) being the operator of the testing facility.

1.1. Vienna Climatic Wind Tunnel

The Vienna Climatic Wind Tunnel is a globally unique facility designed for testing rail vehicles and aviation components under temperatures ranging from -45°C to +60°C and wind speeds reaching up to 280 km/h. Commissioned in 2002, the facility was initially intended for rail vehicle assessments only. Over the years, it has expanded its capabilities to include various icing tests for the aviation sector. The facility features two wind tunnels: the Small Wind Tunnel (SWT) for testing vehicles up to 33.8 metres in length and the Large Wind Tunnel (LWT) for vehicles up to 100 metres, a cross section presented in Fig. 1.1. Both tunnels are equipped with a solar simulation panel on one side wall, enabling the testing of vehicle subsystems, air conditioning performance, and passenger comfort under solar radiation according to standards such as EN 13129, including simulating sensible and latent heat emitted from passengers with radiators and humidifiers [3].
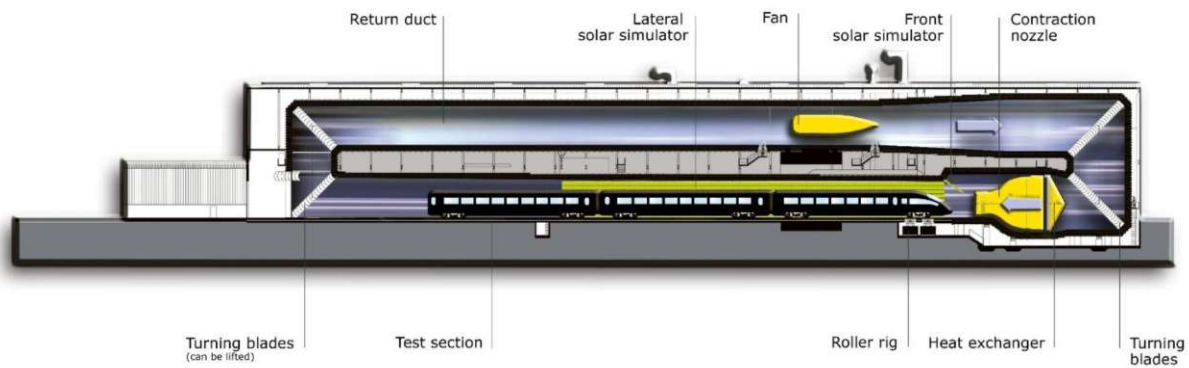
Figure 1.1.: Cross section of the Large Wind Tunnel (LWT) at RTA [4].

1.2. Related work

Prior to this thesis, a bachelor's thesis [5] was completed in collaboration with RTA focusing on a literature review of various sensor types and their functionalities, aimed at identifying potential environmental factors that could affect sensor measurements. Additionally, first measurements were carried out to detect the presence of such environmental influences. However, the resolution and understanding of the physics behind these issues received limited attention, and several issues remained unresolved, as new topics emerged during the course of the experiments, which will be analyzed and addressed within the scope of this thesis.

1.3. Thesis outline

The thesis is structured with an introduction (Chapter 2) to the theoretical physical processes required to understand the following chapters. Chapter 3 provides an overview of the standards employed at RTA to assess passenger comfort in rail vehicles, while Chapter 4 details the sensors used at RTA for determining the relevant physical quantities for this assessment. Chapters 5 through 9 focus on the analysis of various external influences on the sensor types employed, with each chapter addressing a specific influence. In the final chapter (Chapter 10), conclusions are drawn based on the findings, and recommendations for future research topics are provided.

2. Theoretical background

This chapter aims to present an overview of the key theoretical concepts relevant to this thesis. It starts with an introduction to heat transfer, with a particular emphasis on the mechanisms of radiation. Subsequently, the fundamental equations underlying Computational Fluid Dynamics (CFD) are discussed. Finally, the theoretical considerations about the flow around a circular cylinder are analyzed.

2.1. Heat transfer

Heat transfer refers to the energy exchange between objects in response to temperature differences, in accordance with the second law of thermodynamics, which states that heat flows from regions of higher to lower temperature. This transfer occurs through three primary mechanisms:

- Conduction
- Convection
- Radiation

Each mechanism is described by specific physical principles, differential equations, and dependencies, all of which must be considered to perform an accurate thermal analysis. These principles are outlined in this section.

2.1.1. Conduction

Conduction describes the transfer of thermal energy within a material or between materials in direct contact, driven by atomic and molecular interactions. Fourier's law describes this relationship, stating that the heat flux density $\dot{\boldsymbol{q}}$ is directly proportional to the temperature gradient ∇T:

$$\dot{\boldsymbol{q}} = -\lambda \, \nabla T \tag{2.1}$$

The negative sign indicates that heat flows in the opposite direction of the temperature gradient. Here, λ represents the thermal conductivity of the material, which is simplified to a scalar value under the assumption of isotropic and temperature-independent properties.

The first law of thermodynamics:

$$\Delta U = Q_{12} - W_{12} \tag{2.2}$$

3

and the conservation of energy principle allows for the derivation of the transient heat conduction equation for a solid body, as derived in [6]:

$$\rho \, c_p \, \frac{\partial T}{\partial t} - \nabla \cdot (\lambda \, \nabla T) = \dot{Q}_{\text{gen}} \tag{2.3}$$

This equation assumes a stationary, isotropic, and incompressible material with temperature independent material properties c_p and λ. Internal heat sources are considered through the source term $\dot{Q}_{\text{gen}}$. The equation is a linear partial differential equation with a first-order time derivative and a second-order spatial derivative. While analytical solutions are feasible under certain boundary and initial conditions, complex cases generally require numerical approaches, such as Finite Element Method (FEM) or Finite Volume Method (FVM) solvers.

2.1.2. Convection

Convection describes the energy transport with a fluid, including the energy transport by conduction in the fluid and the transport of energy through the macroscopic motion of the fluid itself. Thus, in addition to the material properties, fluid velocity and turbulence characteristics significantly influence heat transfer. Convective heat transfer is particularly important near walls, where the fluid field and the thermal field interact. A distinction is made between forced convection, driven by an external pressure gradient, and natural convection, which arises from density variations that induce fluid flow. Near walls, a boundary layer forms, which may exhibit laminar, turbulent, or mixed flow characteristics [7]. The theory of boundary layers was first proposed by Ludwig Prandtl in 1904 [8]. Given the complexity of the interactions between the flow and temperature fields, a simplified relationship between the wall temperature T_W and the fluid temperature T_∞ can be given by:

$$\dot{q} = \alpha \, (T_W - T_\infty) \tag{2.4}$$

In this formulation, the complexities of convective heat transfer are captured by the heat transfer coefficient α, which depends on thermal fluid properties, flow parameters (e.g., velocity, turbulence intensity), wall geometry, and surface roughness. When the temperature profile is known, α can be calculated, otherwise, it is often determined empirically for certain flow conditions. Dimensional analysis enables the reduction of these parameters, representing α via the dimensionless Nusselt number, defined as:

$$\text{Nu} = \frac{\alpha \, L}{\lambda} \tag{2.5}$$

where L is a characteristic length specific to the problem and λ is the thermal conductivity. The Nusselt number behavior varies fundamentally between forced and natural convection. In forced convection, the flow itself is characterized by the Reynolds number:

$$\text{Re} = \frac{v \, L}{\nu} \tag{2.6}$$

where v is the characteristic velocity and L is a characteristic length, being context dependent. ν is the kinematic viscosity of the fluid. In natural convection cases, the flow regime is described by the Grashof number:

$$\text{Gr} = \frac{L^3 \, g \, \beta \, \Delta T}{\nu^2} \tag{2.7}$$

where g is the gravitational acceleration, β is the thermal expansion coefficient, and $\Delta T = T_W - T_\infty$ represents the temperature difference between the wall and fluid. Dimensional analysis also introduces the Prandtl number, which relates fluid flow properties to thermal diffusion:

$$\text{Pr} = \frac{\nu}{a} \tag{2.8}$$

where $a = \lambda/\rho \, c_p$ represents the thermal diffusivity. Using these quantities, the dimensionless heat transfer coefficient, the Nusselt number, is expressed for forced convection as:

$$\text{Nu} = f_1 \left(\text{Re}, \text{Pr} \right) \tag{2.9}$$

and for natural convection as:

$$\text{Nu} = f_2 \left(\text{Gr}, \text{Pr} \right) \tag{2.10}$$

Closely related to the Grashof number, the Rayleigh number characterizes the flow regime (laminar or turbulent) in a fluid in a natural convection case:

$$\text{Ra} = \text{Gr} \, \text{Pr} = \frac{\beta \, \Delta T \, L^3 \, g}{\nu \, \alpha} \tag{2.11}$$

In many engineering contexts, power-law correlations for the Nusselt number are used for an analytical analysis, expressed as:

$$\text{Nu} = C \, \text{Re}^m \, \text{Pr}^n \tag{2.12}$$

where C, m, and n are empirically determined constants for specific flow conditions [9].

2.1.3. Radiation

Radiation refers to the transfer of energy through electromagnetic waves. Unlike conduction and convection, radiation does not require a medium and is solely dependent on the properties of the emitting surface and its surrounding environment.

The intensity of radiative energy emission from a body is a function of its temperature, surface characteristics, and the wavelength of the emitted radiation. Quantities such as spectral and total radiation intensities enable understanding of the energy distribution emitted or absorbed by surfaces across a range of wavelengths.

The Stefan-Boltzmann law represents the fundamental principle of radiation, expressed as:

$$\dot{q}_e = \sigma \, T^4 \tag{2.13}$$

This law indicates that the emitted radiative heat flux is proportional to the fourth power of the absolute temperature, where $\sigma \approx 5.67 \times 10^{-8}\,\mathrm{W\,m^{-2}K^{-4}}$ is the Stefan-Boltzmann constant. This equation is applicable for an ideal black body. In real-world scenarios, surfaces are typically modeled as gray bodies, which emit radiation at a fraction of the intensity of a black body. This fraction is quantified by the emissivity ϵ, a dimensionless coefficient ranging from $0 \leq \epsilon \leq 1$, representing the efficiency of radiation emission relative to a black body. Accordingly, the Stefan-Boltzmann law for gray bodies becomes:

$$\dot{q}_e = \epsilon\,\sigma\,T^4 \tag{2.14}$$

with $\dot{q}_e$ being the emitted heat flux. When radiative energy emitted by one body impacts another, the receiving body absorbs energy according to:

$$\dot{q}_a = \alpha\,\dot{q}_e \tag{2.15}$$

with $\dot{q}_a$ being the absorbed heat flux. The absorption coefficient α depends on both the temperature of the emitting source and the receiving surface temperature. Both ϵ and α are typically considered as average values over all relevant wavelengths and directions. Radiation that is not absorbed by a surface is either reflected (fraction ρ) or transmitted (fraction τ), satisfying the following balance:

$$\rho + \tau + \alpha = 1 \tag{2.16}$$

For a blackbody, $\alpha = 1$, while an ideal mirror would have $\rho = 1$.

Kirchhoff's law defines a key relationship for surfaces in thermal equilibrium, stating that:

$$\alpha_\nu = \epsilon_\nu \tag{2.17}$$

for a given wavelength and temperature. In the case of a gray body, where the emissivity ϵ is independent of the wavelength, Kirchhoff's law simplifies to:

$$\alpha = \epsilon \tag{2.18}$$

Thus, Eq. (2.14) and Eq. (2.15) hold only for gray bodies.

Planck's law describes the spectral intensity emitted by a black body as a function of frequency ν and temperature T per unit area, given by:

$$I_\nu = \frac{2\,h\,\nu^3}{c^2}\frac{1}{e^{h\,\nu/k\,T} - 1} \tag{2.19}$$

where $c \approx 2.9979 \times 10^8\,m/s$ is the speed of light, $k \approx 1.3806 \times 10^{-23}\,\mathrm{J/K}$ is Boltzmann's constant, and $h \approx 6.6261 \times 10^{-34}\,\mathrm{J\,s}$ is Planck's constant. Integrating the spectral intensity over all wavelengths provides the total radiation intensity:

$$I = \int_0^\infty I_\nu\,d\nu \tag{2.20}$$

representing the emission from a point on a plane surface into the half-space. The normal emission I_n is the intensity emitted perpendicular to the surface, while, according to Lambert's cosine law, the intensity emitted at an angle β to the normal is given by $E_\beta = E_n \cos \beta$. Integration over the half-space yields $I = \pi I_n$, indicating that the total radiant emittance is π times the normal intensity. Lambert's law applies strictly to black bodies with diffuse reflection and emission, excluding mirror-like reflections (e.g., polished metal surfaces). At all presented equations the frequency ν can be replaced by the wavelength $\lambda = c/\nu$ [7].
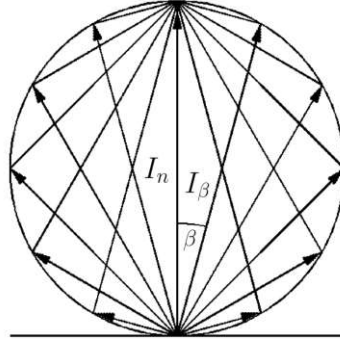
Figure 2.1.: Illustration of Lambert's Cosine Law (adapted from [7])

2.2. Computational Fluid Dynamics (CFD)

In the following sections, the fundamental equations governing fluid mechanics are presented for an understanding of the foundations of the numerical models used in this thesis. These descriptions are based on several references [10–17].

2.2.1. Conservation equations

The conservation equations of mass, momentum, and energy form the basis for analyzing fluid flow. These equations mathematically express the conservation principles, describing how fluid properties vary over space and time within a control volume. In CFD, these laws are discretized and solved numerically, enabling the simulation of fluid dynamics under various conditions.

The conservation of mass principle, asserting that mass is neither created nor destroyed in a fluid system, is fundamental. For any control volume, the rate of mass increase within the volume must equal the net flux of mass across its boundary. In differential form, the continuity equation is expressed as:

$$\frac{\partial \rho}{\partial t} + \nabla \cdot (\rho \, \boldsymbol{v}) = S_M \tag{2.21}$$

where S_M denotes a source term. In the absence of sources, this reduces to the common form of the continuity equation:

$$\frac{\partial \rho}{\partial t} + \nabla \cdot (\rho \, \boldsymbol{v}) = 0 \tag{2.22}$$

The complete description of fluid motion requires the momentum balance, or Navier-Stokes equation, given by:

$$\frac{\partial \left(\rho\, \boldsymbol{v}\right)}{\partial t} + \nabla \cdot \left(\rho\, \boldsymbol{v}\, \boldsymbol{v}\right) = -\nabla p + \nabla \cdot \boldsymbol{\tau} + \rho\, \boldsymbol{g} + \boldsymbol{F} \tag{2.23}$$

where p is the fluid pressure, $\boldsymbol{F}$ represents external body forces, and $\boldsymbol{\tau}$ is the viscous stress tensor. For a Newtonian fluid, $\boldsymbol{\tau}$ is defined as:

$$\boldsymbol{\tau} = \mu \left(\nabla \boldsymbol{v} + (\nabla \boldsymbol{v})^{T}\right) - \frac{2}{3} \mu \nabla \cdot \boldsymbol{v}\, \boldsymbol{I} \tag{2.24}$$

where μ is the molecular viscosity and $\boldsymbol{I}$ is the unit tensor. Inserting Eq. (2.24) into Eq. (2.23) yields:

$$\underbrace{\frac{\partial \left(\rho\, \boldsymbol{v}\right)}{\partial t}}_{\text{I}} + \underbrace{\nabla \cdot \left(\rho\, \boldsymbol{v}\, \boldsymbol{v}\right)}_{\text{II}} = \underbrace{-\nabla p}_{\text{III}} + \underbrace{\nabla \cdot \mu \left(\nabla \boldsymbol{v} + (\nabla \boldsymbol{v})^{T}\right)}_{\text{IV}} - \underbrace{\nabla \cdot \left(\frac{2}{3} \mu \nabla \cdot \boldsymbol{v}\, \boldsymbol{I}\right)}_{\text{V}} + \underbrace{\rho\, \boldsymbol{g}}_{\text{VI}} + \underbrace{\boldsymbol{F}}_{\text{VII}}$$
$$\tag{2.25}$$

The individual terms represent:

   I. Temporal change in momentum

  II. Convective transport of momentum

 III. Pressure gradient force

 IV. Viscous diffusion of momentum

  V. Bulk viscosity (vanishes for incompressible flow)

 VI. Gravitational force

VII. Other external body forces

The conservation of energy states that the rate of energy change within a control volume equals the net flux across its boundaries plus the work done by forces acting on the fluid. The total energy E is defined as:

$$E = h - \frac{p}{\rho} + \frac{|\boldsymbol{v}|^{2}}{2} \tag{2.26}$$

Using Fourier's law (Eq. (2.1)) and including an energy source term $\dot{S}_{E}$, the energy equation becomes:

$$\underbrace{\frac{\partial \left(\rho\, E\right)}{\partial t}}_{\text{I}} + \underbrace{\nabla \cdot \left(\boldsymbol{v}\left(\rho\, E + p\right)\right)}_{\text{II}} = \underbrace{\nabla \cdot \lambda \nabla T}_{\text{III}} + \underbrace{\nabla \cdot \boldsymbol{\tau}\, \boldsymbol{v}}_{\text{IV}} + \underbrace{\dot{S}_{E}}_{\text{V}} \tag{2.27}$$

The terms in Eq. 2.27 represent:

    I. Rate of change in internal energy

   II. Convective transport of energy

  III. Energy flux due to heat conduction

  IV. Viscous dissipation

   V. Energy sources/sinks

The continuity Eq. (2.22), Navier-Stokes Eq. (2.25), and energy Eq. (2.27) form a set of five equations with six unknowns, requiring an additional equation relating two thermodynamic quantities to fully define the system. As there is no universal equation of state for all fluids, it must be defined problem dependent. For an ideal gas, the ideal gas law can be used which is expressed as:

$$\frac{p}{\rho} = R\,T \tag{2.28}$$

with $R \approx 287\,\mathrm{J\,kg^{-1}K^{-1}}$ being the specific gas constant for air at $20\,^{\circ}\mathrm{C}$.

2.2.2. Radiation modelling

ANSYS Fluent, a commercial CFD solver, offers a broad range of radiation models, each designed with specific functionalities and computational capabilities. In this thesis, the Discrete Ordinates (DO) model has been selected due to its support for features such as the definition of semi-transparent walls and non-gray radiation, alongside its moderate computational costs under typical discretizations. The DO model also allows a user-defined mix of specular and diffuse reflection on surfaces.

The modeling of radiation involves the scalar Radiative Transport Equation (RTE), which describes the radiation intensity I_λ at a given position $\boldsymbol{x}$ in a direction $\boldsymbol{\Omega}$:

$$\underbrace{\boldsymbol{\Omega} \cdot \nabla I_\lambda}_{\text{I}} + \underbrace{(K_{a\lambda} + K_{s\lambda})\,I_\lambda}_{\text{II}} = \underbrace{K_{a\lambda}\,n^2\,\frac{\sigma\,T^4}{\pi}}_{\text{III}} + \underbrace{\frac{K_{s\lambda}}{4\pi} \int_{4\pi} I_\lambda(\boldsymbol{x}, \boldsymbol{\Omega}')\,\Phi(\boldsymbol{\Omega}, \boldsymbol{\Omega}')\,d\boldsymbol{\Omega}'}_{\text{IV}} \tag{2.29}$$

In this equation $K_{a\lambda}$ and $K_{s\lambda}$ represent the wavelength-dependent absorption and scattering coefficients of the medium, respectively, n denotes the optical thickness of the medium and $\Phi(\boldsymbol{\Omega}, \boldsymbol{\Omega}')$ is the phase function, which characterizes the scattering behavior by defining the angular distribution of scattered radiation, as described in [16].

The terms in Eq. 2.27 represent:

    I. Represents the directional change in radiation intensity

   II. Attenuation (absorption and scattering losses)

  III. Thermal emission from the medium

  IV. Scattering of radiation into the direction $\boldsymbol{\Omega}$ from other directions $\boldsymbol{\Omega}'$

When non-gray radiation is modeled, the RTE must be solved for each wavelength band defined. Within the DO model framework, the total radiation intensity I_{tot} is obtained by a weighted sum of the intensity I_λ and the discrete wavelengths λ_k, expressed as:

$$I_{tot} = \sum_k I_\lambda \, \Delta\lambda_k \tag{2.30}$$

Boundary conditions are then applied individually to each wavelength band.

In Fluent each octant of the angular space 4π is divided into $N_\theta \times N_\phi$ solid angles, where θ and ϕ are the polar and azimuthal angles, respectively. Both angles are spaced uniformly with increments $\Delta\theta$ and $\Delta\phi$. For three-dimensional modeling, the RTE must be solved for each discretized direction, yielding $8N_\theta N_\phi$ directional calculations per wavelength band. Specific numerical considerations and optimizations arising from this discretization are described in the Fluent Theory Guide [16].

2.3. Flow past a circular cylinder

This setup is widely recognized in the literature as a reference case for validating various CFD simulation configurations and turbulence models against experimental data. The following section provides an overview of the obtained results relevant for this thesis.

Different Reynolds numbers lead to distinctly varying downstream flow behavior, as illustrated in Fig. 2.2. For Re numbers below 5, the flow remains attached and can be described within the creeping flow theory. As the Re number increases, a pair of steady vortices is generated. In the range of $40 \leq \text{Re} < 200$, a laminar vortex street is observed. As the Re number increases further, the wake transitions into a turbulent state, becoming fully turbulent at Re = 300. This turbulent wake regime persists up to Re = 3×10^5. At higher Re numbers, additional flow patterns emerge, which are not relevant to the scope of this thesis.
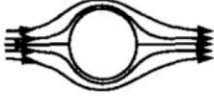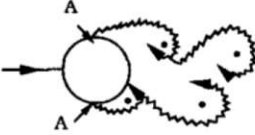
Flow pattern	Reynolds Number	Flow regime
a)	$Re < 5$	No separation. Creeping flow
b)	$5 < Re < 40$	A fixed pair of symmetric vortices
c)	$40 < Re < 200$	Laminar vortex street
d)	$200 < Re < 300$	Transition to turbulence in the wake
e)	$300 < Re < 3 \times 10^5$ Sub-critical	Wake completely turbulent. A: Laminar boundary layer separation

Figure 2.2.: Flow regimes around a circular cylinder at various Reynolds numbers [18].

For this thesis, the wake length downstream of the cylinder at different Re numbers is of particular interest. While many studies focus on a Re number of 3900 for comparison purposes, additional simulations and experiments are available for other Re numbers [19, 20].

Fig. 2.3 compares the recirculation length, defined as the distance along the centerline downstream where the temporally averaged velocity changes sign, at various Re numbers. It is evident that the recirculation length varies significantly, indicating distinct wake behaviors across different flow regimes. Additionally, the length at which the velocity fully recovers to its pre-cylinder value is substantially larger than the recirculation length.
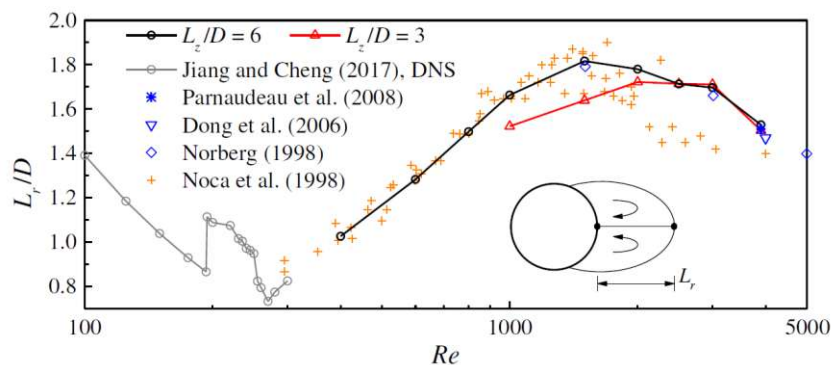
Figure 2.3.: Recirculation length as a function of Reynolds numbers, determined through various CFD simulations and experiments [21].

3. Standards

Most vehicles, particularly railway vehicles evaluated in the RTA facility, must comply with various test criteria to maintain passenger comfort which are specified in standards to gain approval. The standards for railway vehicles include EN 13129 *"Railway applications - Air conditioning for main linerolling stock - Comfort parameters and type tests"* [3], EN 14750 *"Railway applications - Air conditioning for urban and suburban rolling stock"* [22], and EN 14813 *"Railway applications - Air conditioning for driving cabs"* [23], each applicable to different types of vehicles (e.g., subways, tramways, regional transportation vehicles, long-distance transportation vehicles) maintaining passenger and employee comfort. The most recent standard is EN 13129, last revised in 2016. It is particularly relevant to this thesis due to its stringent regulations and will be discussed further in the next section. Similarly, the measurement equipment must adhere to various requirements specified in ISO 7726 *"Ergonomics of the thermal environment – Instruments for measuring and monitoring physical quantities"* [24]. This standard defines the physical quantities related to human comfort and the necessary measurement equipment specifications along with their accuracy, which will be described further in Section 3.2.

3.1. EN 13129 "Railway applications - Air conditioning for main linerolling stock - Comfort parameters and type tests" [3]

This standard is relevant for long-distance transport vehicles with passenger travel times over one hour [22]. It outlines the testing procedures and quality thresholds for evaluating vehicles under various climatic conditions. The operational and extreme conditions applicable for testing are determined by the countries where the vehicle operates, leading to Europe being divided into three summer and three winter climatic zones, each with distinct maximum and minimum conditions such as temperature levels and solar radiation intensity. Additionally, the standard defines quality levels q1 and q2 for certain parameters and tests, with q1 being the more stringent limit vehicle manufacturers aim to achieve. Depending on the vehicle's performance in a test case, a vehicle may meet the q2 quality level but fails to meet q1 for a specific test scenario and comfort parameter. In the end, an overall conformity level CL is calculated with these quality levels.

3.1.1. Measured comfort parameters

The parameters used to assess passenger comfort are as follows:

- air temperature
- air speed
- relative humidity
- surface temperatures

Furthermore, external climatic conditions, such as solar radiation, indirectly influence these parameters. However, the standard does not take them explicitly into account.

Since surface temperature measurements were not analyzed in the scope of this thesis, they will not be discussed further.

3.1.2. Test procedure

EN 13129 outlines a comprehensive set of tests to ensure passenger comfort in various conditions. It specifies a total of 68 tests, each of them typically lasting one hour. Some tests apply exclusively to vehicles with compartments, while others are not mandatory. The parameters that can vary include:

- mean temperature in the climatic chamber
- relative humidity in the climatic chamber
- passenger load
- solar radiation
- wind speed

The criteria for passenger comfort assessment depend on the specific test. For instance, in a door opening test, only the mean interior temperature needs to be evaluated, other measured quantities are not considered.

3.1.3. Passenger comfort assessment

The assessment of passenger comfort to determine a conformity level is based on the following parameters:

- range of the arithmetic mean of the interior air temperatures measured 1.1 m above the floor with respect to the target temperature to be achieved by the room air
- range of the horizontal extreme air interior temperatures
- range of the vertical extreme interior air temperatures for seated and standing passengers
- surface temperatures
- humidity
- air speed
- quality of regulation

Upon the completion of all tests, an overall conformity level CL is determined using a formula with various weighting factors for all tests. Based on the results, the tested vehicle is classified into one of the following categories:

- Level A: $97\% \leq \text{CL} \leq 100\%$
- Level B: $93\% \leq \text{CL} < 97\%$
- Level C: $85\% \leq \text{CL} < 93\%$
- Below 85% or if at minimum one parameter fails the q2 limit at a certain test case, the standard is not conformed to.

An obligatory overall conformity level is commonly specified in procurement contracts by railway companies. Failure to meet this level may result in significant fines for the suppliers.

3.2. EN ISO 7726 "Ergonomics of the thermal environment – Instruments for measuring and monitoring physical quantities" [24]

It is important to note that the current valid standard is EN ISO 7726 in the version of 2001. Although a revised version is under development with several proposed changes, it remains in draft status and has not yet been officially released. Consequently, the 2001 version remains the reference for this thesis, unless otherwise specified.

EN ISO 13129 [3], Ch. 15, defines the required accuracy of measurement instruments by referring to the two quality classes specified in EN ISO 7726: Class C (comfort) and Class S (stress). Tbl. 3.1 provides a summary of the measurement classes for sensors as required by EN 13129.

Measuring quantity	Class
Air temperature	Class S
Relative humidity	Class C
Air speed	Class C

Table 3.1.: Required sensors measurement classes according to EN ISO 13129 for the measurement in rail vehicles.

In measurement technology, it is essential to differentiate between the accuracy of measuring the physical quantity, which can be influenced by external factors during the measurement process (e.g., solar radiation), and the intrinsic accuracy of the sensor itself under controlled conditions. ISO 7726 Tbl. 2 defines the required accuracies of the sensor itself and offers guidance on the appropriate application of measurement devices to minimize the influence of external factors. The external measurement uncertainty must be specified by the user of the measurement device and should account for additional factors such as solar radiation or sensor positioning.

In the following paragraphs, the most important statements from the standard relevant to this thesis are summarized.

3.2.1. Air temperature

Air temperature sensors measure the physical quantity temperature, denoted by the symbol t_a, and must comply for EN ISO 13129 with the standards class S, with a measuring range of $-60\,°\text{C}$ to $150\,°\text{C}$. The required sensor accuracy is $\pm(0.6\,°\text{C}+0.01\cdot|t_a|°C)$, with a desirable accuracy of $\pm(0.15\,°\text{C}+0.002\cdot|t_a|°C)$. It is important to note that a temperature sensor only measures its own temperature, which may differ from the actual temperature of the surrounding medium (e.g., air) due to external influences such as solar radiation. Therefore, minimizing these effects is essential for accurate measurements.

ISO 7726 suggests several measures to minimize the effects of solar radiation: reducing the emission factor of the sensor, lowering the temperature difference between the sensor and the surrounding by applying thin sheets of reflective material and maintaining an airspace large enough for natural convection, or increasing heat transfer by enhancing air velocity around the sensor with forced ventilation and a simultaneously reduction in sensor size. Additionally, it is crucial to reduce the thermal inertia of the sensor to decrease the period to reach a thermal equilibrium. The shortest measurement time should not be less than 3.5 time-constants of the sensor. To obtain a faster-responding temperature sensor, one can reduce the heat capacity by decreasing the sensor mass, using materials with lower heat capacity, or improving convective heat transfer.

3.2.2. Relative humidity

According to ISO 7726, only the measurement of absolute humidity, expressed as the partial pressure of water vapor, is specified. Since the direct measurement of relative humidity is typically performed, it is necessary to convert the data from ISO 7726 into relative humidity values based on temperature. Tbl. 3.2 presents the measurement range and required accuracy for a temperature range from $18\,°\text{C}$ to $30\,°\text{C}$, calculated using the Antoine equation to determine the saturation pressure [25].

Temperature [$°C$]	Saturation pressure [Pa]	Measurement range [$\% RH$]	Required accuracy [$\% RH$]
18	2056	24.32 - 100.00	7.30
19	2189	22.84 - 100.00	6.85
20	2330	21.46 - 100.00	6.44
21	2478	20.18 - 100.00	6.05
22	2634	18.98 - 100.00	5.69
23	2800	17.86 - 100.00	5.36
24	2974	16.81 - 100.00	5.04
25	3158	15.83 - 95.00	4.75
26	3351	14.92 - 89.52	4.48
27	3555	14.06 - 84.39	4.22
28	3769	13.27 - 79.59	3.98
29	3995	12.52 - 75.10	3.76
30	4232	11.82 - 70.89	3.54

Table 3.2.: Calculated measurement range and required sensor accuracy based on water vapor saturation pressure.

3.2.3. Air speed

Determining the air speed v_a in class C requires a sensor accuracy of $\pm(0.1+0.05 \cdot v_a)\,\text{m/s}$, with a desirable accuracy of $\pm(0.05 + 0.05 \cdot v_a)\,\text{m/s}$. The measurement range is from $0.05\,\text{m/s}$ to $1\,\text{m/s}$. These accuracies must be guaranteed for any flow direction within a solid angle of 3π. This implies that these accuracy criteria do not need to be met for directions coming from one-quarter of a sphere's surface. For example, in the case of hot sphere anemometers, flow coming from the direction of the shaft usually does not meet the accuracy requirement. Fig. 3.1 illustrates this angular dependency of a hot sphere anemometer.

3.3. EN 13182 "Ventilation for buildings - Instrumentation requirements for air velocity measurements in ventilated spaces (including corrigendium AC:2002)" [26]

In the course of this work, a previously unconsidered but interesting standard emerged — EN 13182. This standard defines parameters for air speed measurements in buildings. Although the application is very similar to measurements in railway vehicles, it has never been referenced at RTA. According to the standard, three types of common areas are defined, and a railway coach can be classified as common area C. Tbl. 2 of [26] specifies that the range of the average speed is between 0.1 and 0.5 m/s, the degree of turbulence is between 20% and 80%, the frequency of the airflow is less than 1 Hz, and the temperature
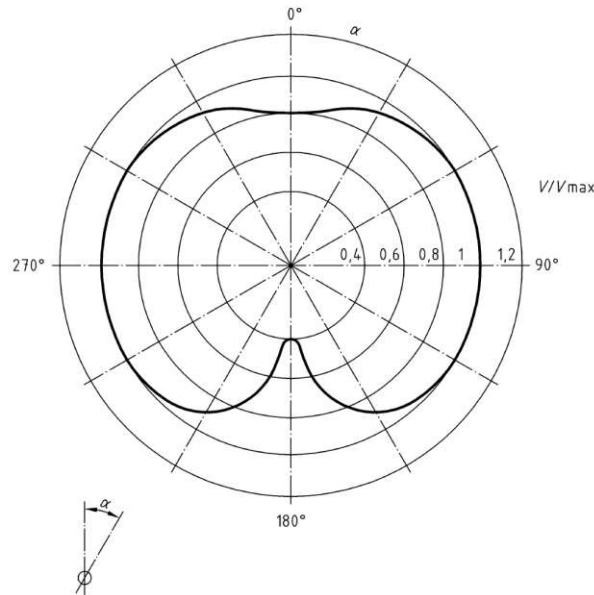
Figure 3.1.: Angular dependency of a hot sphere anemometer [24]. The shaft of the anemometer is positioned at an angle of $\alpha = 180°$.

range is between 18 and 35 °C. Therefore, the necessary requirements for the air speed probes are defined in Fig. 1 of [26] as follows: a range of average speed from 0.05 to 1 m/s, a temperature range of 18 to 35 °C, an upper frequency f_{up} of 1 Hz, a minimum measurement length of 180 s, and a sampling frequency of at least 5 Hz. Furthermore, Ch. 6.4 of this standard states that the supplier of the measurement devices must provide deviations from the real value in a speed range from 0.05 to 0.25 m/s (at higher speeds forced convection dominates) with dividing intervals of 0.05 m/s under the following conditions:

- Measuring probe horizontally with flow streaming vertically downwards
- Measuring probe horizontally with flow streaming vertically upwards
- Measuring probe vertically with flow streaming horizontally

Nevertheless the supplier of the air speed probes at RTA couldn't provide this data. Due to the probe's shaft and constructional details, a measuring probe has directional sensitivity, as explained in Sec. 3.2.3.

Difference between EN 13129 and EN 13182

Although EN 13182 defines limits for a minimum sampling frequency, these are not relevant for tests performed according to EN 13129. The absence of turbulence intensity limits in EN 13182 mean that high sampling frequencies and fast response times are not required. The measuring device can have a higher time constant and therefore mitigate the noisy instantaneous velocity. Subsequently, the signal will be averaged over a period of at least three minutes. EN 13129 does not mention turbulence intensity and, consequently, does not consider it in the assessment of passenger comfort. However, turbulence intensity can significantly influence the sensation of draught, as stated in various papers [27, 28], and may should be considered in a revised version of EN 13129.

4. Currently used sensors

This chapter provides an overview of the sensor types employed at RTA that are relevant to the scope of this thesis. A comprehensive explanation of the physical principles underlying these sensor types is available in the literature, as well as in the previously performed bachelor's thesis [5].

4.1. Temperature sensors

At RTA, Pt100 resistance thermometers are currently used. Two different types of them are used based on the measurement location: larger sensors, referred to as room temperature sensors, are used to measure the room temperature in compartments, while smaller sensors, known as channel temperature sensors, are utilized in ducts and in applications where localized temperature measurements of a fluid are required. Fig. 4.1 illustrates both types.

Figure 4.1.: Temperature sensors used at RTA. Left: Room temperature sensor. Right: Channel temperature sensors.

4.1.1. Room temperature sensors

The Pt100 sensing element is fixed within a five-pin plug known as a Tuchel plug (DIN 41624 [29]). To protect the sensor against solar radiation, the sensor is encased in a

brass sleeve coated with a chromium layer. The Pt100 sensing element is secured in the strain relief of the plug and connected to the measurement system via a four-wire circuit, ensuring high accuracy. Two slightly different designs of the Pt100 sensing element are currently in use: an older version with a diameter of 3 mm and an increased diameter section at the wire side, and a newer design with a constant diameter of 3 mm [30]. Fig. 4.2 shows a disassembled sensor along with the two possible sensing elements.
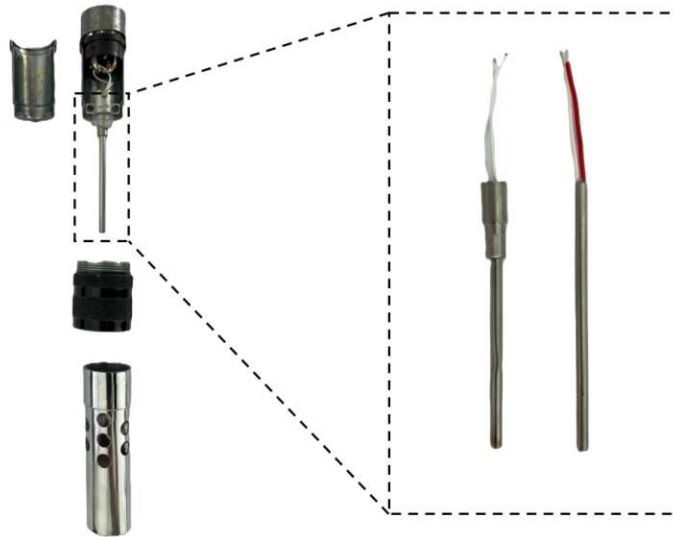
Figure 4.2.: Temperature sensors used at RTA. Left: Disassembled room temperature sensor. Right: Different sensing elements used at RTA.

4.1.2. Channel temperature sensors

This sensor type does not have a custom-built fixation within the plug. Instead, the Pt100 sensing element is directly connected to the wire using a shrink hose. It lacks solar radiation protection, as it is primarily used in areas without significant exposure to solar radiation. Similar to the previous design, this sensor is connected to the measurement system using a four-wire circuit.

4.2. Relative humidity sensors

Currently, three different sensor types are in use, as depicted in Fig. 4.3. The largest and oldest, the MP103A, is exclusively used for measuring relative humidity in compartments. The second type, the XD33A, is the latest model introduced and features a smaller diameter, also primarily used for relative humidity measurements in compartments. The smallest sensor, the EE08, is mainly utilized to measure relative humidity in airflow channels of vehicles, but it is also used in compartments when other sensor types are not available.

Figure 4.3.: Relative humidity sensors used at RTA. Left: XD33A. Middle: MP103A. Right: EE08.

4.3. CO_2 concentration sensors

Although EN 13129 [3] and the other standards referenced in Ch. 3 do not explicitly mention CO_2 concentration measurements inside vehicles, this is performed at RTA to determine the minimum fresh air rate mentioned in EN 13129. Furthermore, modern vehicle air conditioning systems are equipped to monitor CO_2 levels, enabling the system to adjust airflow based on passenger load. In the RTA wind tunnel CO_2 from an external tank is injected into the vehicle through pipelines. The measurement of CO_2 concentration within the compartment is achieved using the GMP252 CO_2 sensing probe from Vaisala, as illustrated in Fig. 4.4. The probe has a broad measurement range of 0 to $10\,000$ ppm and employs a heated sensor head to prevent condensation. Additionally, the sensor is temperature-compensated [31, 32].

Figure 4.4.: CO$_2$ sensor used at RTA.

4.4. Air speed sensors

Airspeed measurements in vehicles are carried out using the TSI 8475 omnidirectional hot sphere anemometer. This temperature-compensated device offers several selectable measurement ranges, with an accuracy of $\pm 3\%$ plus 1% of full scale at the selected range, for temperatures between $20\,°C$ and $26\,°C$. Outside this range, but within the temperature compensation limits of $0\,°C$ to $50\,°C$, an additional 0.5% per $°C$ outside the standard range must be added to the accuracy. The directional sensitivity is rated at $+5\%/-20\%$ of the readings regardless of the flow direction, and within $3\pi\,\mathrm{sr}$, the sensitivity is $+0\%/-0.05\%$ [33].

The SWEMA03 hot sphere anemometer is used as a reference for calibrating the TSI anemometer in the flow channel, as described in Section 9.1. The SWEMA03 anemometer provides higher accuracy than the TSI device and has the capability to measure the turbulence intensity of a flow, although this functionality is not utilized at RTA. Moreover, the SWEMA03 can measure and transmit temperature data to the recording system.
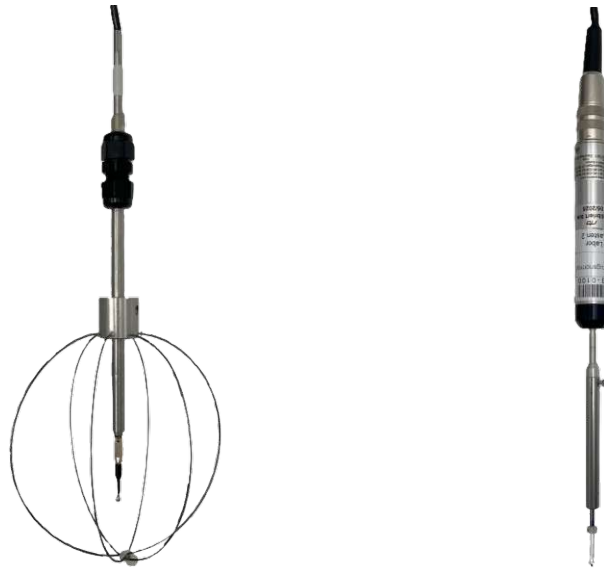
Figure 4.5.: Omnidirectional anemometer used at RTA. Left: TSI 8475 with metal cage. Right: SWEMA03.

5. Influence of solar radiation on temperature sensors

This chapter investigates the influence of radiation on room temperature sensors and proposes a new design aimed at reducing this effect. When temperature sensors are exposed to heat sources, they measure a value between the ambient air temperature and the mean radiant temperature. To mitigate the impact of radiation, technical protective measures are essential and were analyzed in this thesis [24].

An initial series of measurements in the test room was performed using the original sensor design. This was followed by an iterative design process aimed at improving the sensors performance under solar radiation. At key development stages, the test room results were validated in a vehicle within the climatic wind tunnel. Simultaneously, CFD models of both the current design and the most promising new designs were developed to better understand the underlying physical processes.

5.1. Experimental setups

The following chapter describes the setups used to determine the influence of radiation on temperature measurement. Initially, experiments were carried out in a controlled test room environment, allowing for the evaluation of different radiation shields under constant conditions. Subsequently, the developed radiation shields were validated in a vehicle in the wind tunnel. Conclusions were drawn, and following an iterative improvement process in the test room, another validation setup in the wind tunnel was performed. It is important to note that these measurements were performed concurrently with the customer's measurements, and therefore, the measurement conditions were predetermined.

A temperature sensor is expected to display the same temperature regardless of the radiation present [24]. Since radiation from the solar simulation both in the wind tunnel and the test room inherently increases the temperature of an object, it is assumed that lower temperature values are closer to the ambient temperature, as if no radiation would be present. This assumption is fundamental for interpreting all measurements presented in this chapter.

5.1.1. Test room setup

Tests were performed to evaluate different radiation shields in a controlled environment with the objective of obtaining high-quality and repeatable results. Temperature sensors,

23

equipped with different radiation shields, were positioned in front of the solar simulation lamp inclined at an angle of 30°. The sensors were placed at a height of 0.8 meters with a perpendicular distance of 0.95 meters from the center of the lamp. A glass pane, identical to the one protecting the lamps in the wind tunnel, was placed directly in front of the lamp. The BF Engineering lamp (BF HQI) with a nominal radiation intensity of 1000 W was controlled via a control unit (Rack/BF4X100L). A reference sensor (HMP75B), connected to an HMI75 indicator, was placed in a shaded area behind the lamp to record the ambient temperature without direct radiation exposure. The goal was to ensure that the heat generated by the lamp would be distributed via convection and ventilation, allowing the reference sensor to measure the same temperature as the tested sensors, but without the influence of radiation.

In some experiments, a pyranometer (SMP85) was used to monitor the lamp's performance during the initial warm-up phase. In certain cases, a thermal imaging camera (FLIR T660) was used to gain insights into the temperature distribution of the radiation shields, as dicussed in Sec. 5.2.2. Fig. 5.1 shows the schematic setup in the test room.

All measurement devices were connected to a data acquisition system (NI-Box), which transmitted the data via Ethernet to the logging system Talent (ReACT Talent Operator Interface 4.0.284). These devices and software systems were utilized in all experiments carried out for this thesis.
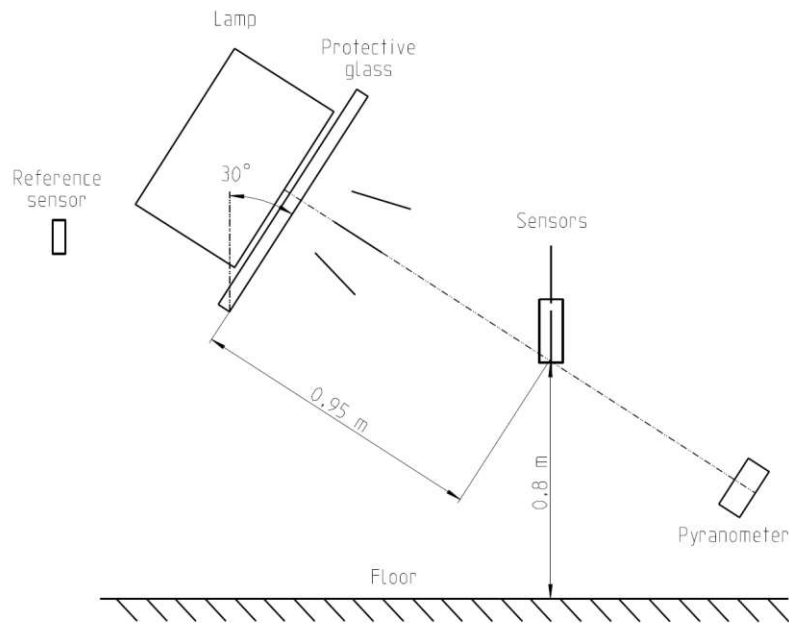
Figure 5.1.: Schematic representation of the cross section of the test room setup.

5.1.2. Development of the new sensor

As outlined in the subsequent sections, the development of a new radiation shield for the existing temperature sensors proved insufficient. Consequently, a new significantly smaller sensor housing was developed. This section presents the design of the new sensor.

The development specification required the reuse of the existing Pt100 sensing elements due to their high cost and widespread deployment at RTA. Thus, it was necessary to integrate these elements into the new sensor design. Two configurations of Pt100 sensing elements, used at RTA, needed to be integrated, as illustrated earlier in Fig. 4.2 (Right). After several design iterations, a compact, economical, and functionally robust sensor design with minimized radiation sensitivity has been developed. The finalized designs can be seen in Fig. 5.2, which depicts the Pt100 element with a constant diameter, and Fig. 5.3, illustrating the Pt100 element with an increased diameter section.

Both sensor designs, similar to the current sensor configuration, utilize a plug as the housing for the sensing element. The Renk DIN plug [34] was selected for its compact size, light weight, and high availability. In the design with a constant diameter of the Pt100 element it is housed in a 3D-printed component and secured using a heat-set insert and a screw. The connection of the Pt100 element's two wires to the shielded 4-core cable (forming a 4-wire circuit) is achieved by soldering three wires into each of the two brass tubes. These brass tubes are then inserted into the 3D-printed part. A strain relief grips the cable along with its shield and holds the assembly together. The strain relief snaps into the 3D-printed part, which has a threaded hole for securing the strain relief and other components in the housing. Fig. 5.2 illustrates the disassembled sensor.
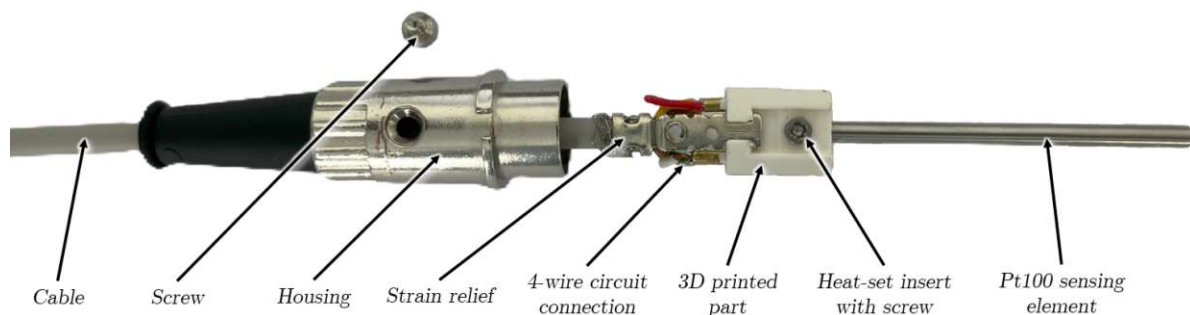
Figure 5.2.: Disassembled new sensor with a Pt100 sensing element of constant diameter. For assembly, the entire package is inserted into the housing and then secured with the screw.

The design with the increased diameter differs slightly from the previous configuration. In this version, the Pt100 element is secured in one direction by an enlarged diameter at the housing. Additionally, a portion of the material is heated with a soldering iron to secure the element tightly on the other side, as the use of a heat-set insert was not feasible due to space constraints. The other components remain identical to the constant diameter design. Fig. 5.3 depicts the disassembled sensor with the increased diameter configuration.

Cable   Screw   Housing   Strain relief   4-wire circuit connection   3D-printed part   Pt100 sensing element
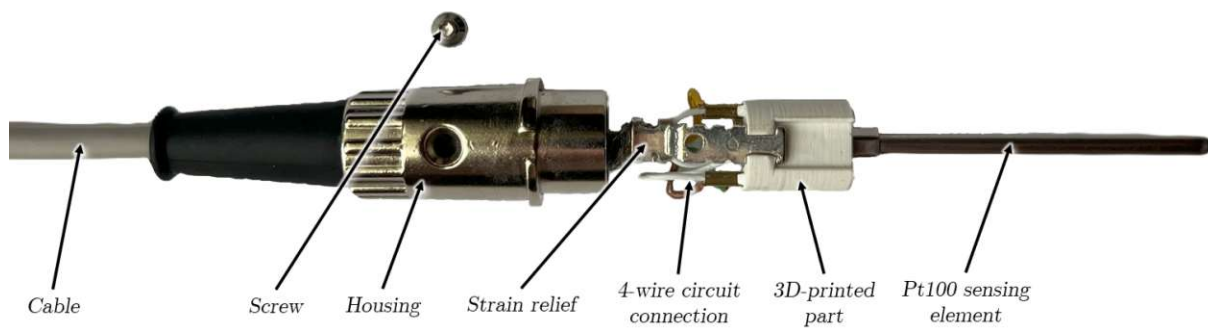
Figure 5.3.: Disassembled new sensor with a Pt100 sensing element with an increased diameter section. For assembly, the entire package is inserted into the housing and then secured with the screw.

5.1.3. Different sensor and radiation shield configurations

All sensor and radiation shield configurations were developed through an iterative process in the test room. Initially, the focus was on applying a new radiation shield to the currently used sensor (see Fig. 5.4). However, achieving optimal results with the existing sensors would require an impractically large radiation shield. Consequently, a significantly smaller sensor was developed, incorporating alternative radiation protection strategies, as shown in the previous section. First, the same tube-based concept was implemented using various materials and coatings (see Fig. 5.5), followed by the development of a much more compact configuration (see Fig. 5.6).

Figure 5.4.: Selection of the tested radiation shield configurations for the currently used temperature sensor.

Figure 5.5.: Selection of the tested radiation shield configurations for the newly developed temperature sensor.

Figure 5.6.: Selection of the tested radiation shield configurations for the newly developed temperature sensor after the first validation.

5.1.4. Validation setup in a bus

To validate the intermediate performance of the developed radiation shields, a test setup was installed in a bus. Two different measurement positions were selected, both equipped with the same sensor types and radiation shields, as illustrated in Fig. 5.7. For comparison purposes, the distance of the two measurement positions from the window of the bus was identical, as was the arrangement of the sensors. No shaded reference sensor was used because it was deemed impossible to ensure that the reference sensor would measure the same air temperature as without exposure to radiation. Therefore, the differences between sensor type A and the other sensors are analyzed.

Figure 5.7.: Two identical measurement positions with measurement position 1 in the middle of the bus and measurement position 2 in the back of the bus. Photo taken in the preparation hall.

The sensors listed in Tbl. 5.1 were deployed in the vehicle. The corresponding measurement results are linked to the sensors through their assigned identification numbers (measurement configuration).

Abbreviation	Sensor number	Radiation shield	Position[1]	Measurement Position
AT01	00-1005	Standard	1	1
AT02	00-0236	Cylinder	2	1
AT03	LT14 (new built)	Cylinder	3	1
AT04	LT08 (new built)	Cylinder	4	1
AT05_Ext	00-1056	Standard	5	1
AT11	00-1010	Standard	1	2
AT12	00-0234	Cylinder	2	2
AT13	LT16 (new built)	Cylinder	3	2
AT14	LT15 (new built)	Cylinder	4	2

[1] The sensor positions are sequentially numbered from the front to the rear of the bus.

Table 5.1.: Sensors used in the validation setup in the bus.

Sensor type B was selected to demonstrate the substantial radiation shield required to minimize the influence of radiation. Sensor type C, as well as sensor type D, were chosen to illustrate the impact of diameter on performance, highlighting a minor performance loss under radiation. This setup aims to confirm that small differences observed in the test room can also be detected in field conditions.

The following sections provide detailed descriptions of the two measurement positions.

Measurement position 1

This position was situated in the middle of the bus. The sensors and their respective radiation shields are depicted in Fig. 5.8. Four different configurations of sensors and radiation shields were tested: a standard room temperature sensor (type A) as currently used at RTA for comparison purposes, a room temperature sensor with an aluminum foil-coated cylinder as a radiation shield (type B), and two new sensors with aluminum foil-coated cylinders of different diameters (type C and D). The radiation shield of type C has an inner diameter of 35 mm, and the radiation shield of type D has an inner diameter of 42.5 mm, with both having a wall thickness of 1.5 mm. The radiation shield of type B has an inner diameter of 50 mm with the same wall thickness of 1.5 mm as the others.
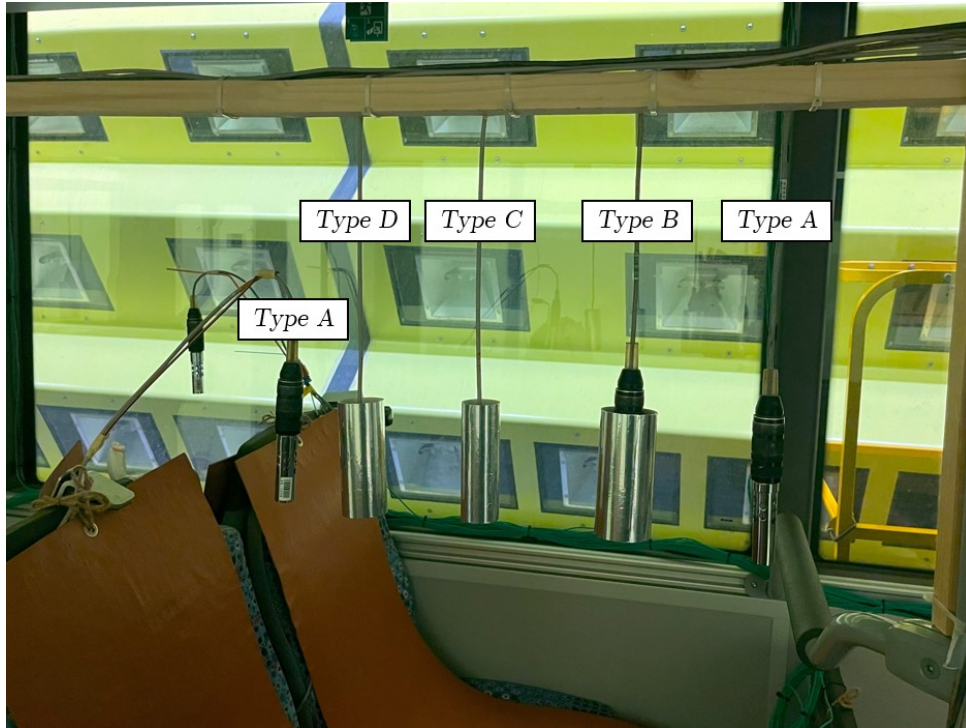
Figure 5.8.: Measurement position 1. Photo taken in the Small Wind Tunnel (SWT).

Additionally, a standard room temperature sensor (type A) was positioned near the measurement position to represent the measurement position used by RTA customers. Given that two type A sensors were deployed at the outermost positions, it was hypothesized that the sensors placed between them would exhibit the average temperature of the outer sensors, assuming they would be type A sensors as well. An important aspect of this setup was the presence of a heating mat below the sensors, simulating the sensible heat of passengers.

Measurement position 2

Measurement position 2 comprised the same sensor types with identical radiation shields as those used in measurement position 1 (see Fig. 5.9).
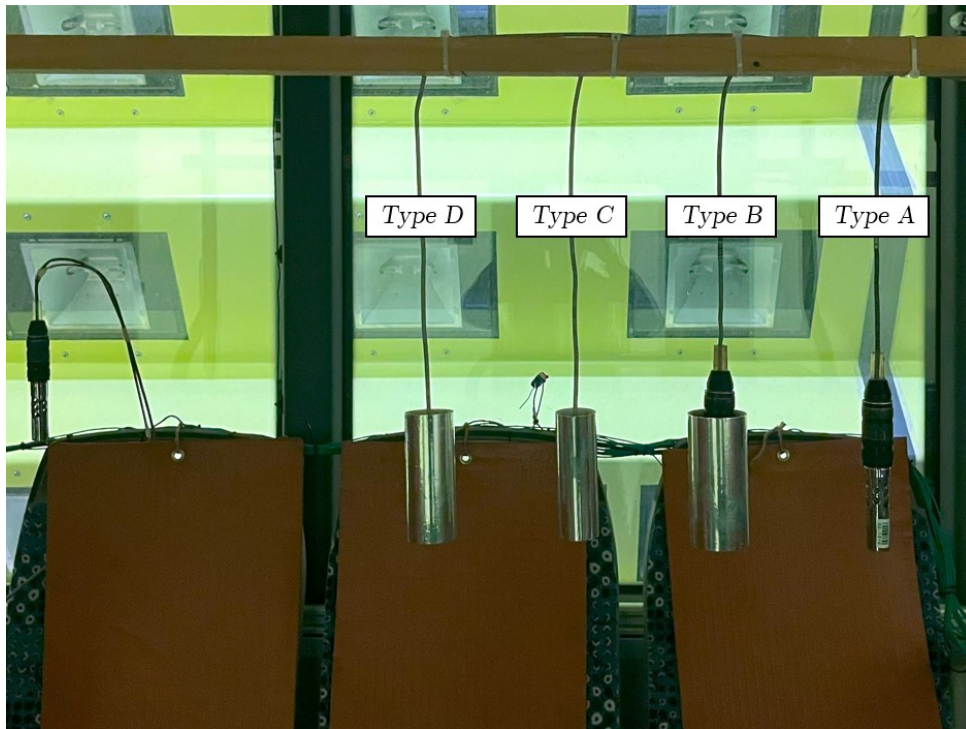
Figure 5.9.: Measurement position 2. Photo taken in the Small Wind Tunnel (SWT).

Heating mats were also placed below the sensors, influencing the measurements. Both measurement positions had a nearly unobstructed view to the solar simulation.

5.1.5. Validation setup in a rail vehicle

In this vehicle, the final version of the various tested design iterations was evaluated against the currently used type A sensors. The objective was not only to reaffirm the correlation between the test room and wind tunnel results but also to acquire insights into the sensor's performance under field conditions, such as its response time to temperature changes.

Fig. 5.10 shows the four different measurement positions in the rail vehicle. Measurement position 1 and 2 have identical setups for a comparative analysis. Measurement position 3 is situated near the wall and is not exposed to direct radiation, whereas measurement position 4 is on the opposite side of the aisle near the window and therefore also less exposed to radiation.

Figure 5.10.: Measurement positions in the rail vehicle. Measurement position 1 and 2 are identical. Measurement position 3 is not exposed to direct radiation. Measurement position 4 is on the shaded side of the vehicle. Photo taken in the Large Wind Tunnel (LWT).

In the vehicle the sensors from Tbl. 5.2 have been used.

Abbreviation	Sensor number	Radiation shield	Position	Comment
AT01	00-1010	Standard	1	/
AT02	LT15 (new built)	Newly developed	2	/
AT03	00-0236	Standard	1	/
AT04	LT16 (new built)	Newly developed	2	/
AT05	00-0094	Standard	1	Customer sensor
AT06	LT14 (new built)	Newly developed	2	/
AT07	00-0095	Standard	1	Customer sensor
AT08	LT08 (new built)	Newly developed	2	/

Table 5.2.: Sensors used in the validation setup in a long distance transportation railway vehicle.

In contrast to the validation performed in the bus, this setup compared the currently used sensor type A with the newly developed sensor type E featuring advanced radiation protection. Heating mats were placed beneath all sensors, with the type A sensors positioned closer to them, potentially experiencing greater influence. To investigate this effect, as described later in Sec. 5.2.5, the positions of the sensors of type A and E at measurement position 2 were swapped close to the end of the measurement campaign to exclude the possibility of higher temperature values closer to the heat mats.

5.2. Experimental results

All sensors used in the experiments were calibrated on the date of use. The newly constructed sensors underwent calibration in a climate chamber using an aluminum block, which is also employed for the annual verification of the temperature sensors at RTA. The calibration in the climate chamber was carried out at a reference temperatures of $20\,^\circ\text{C}$ and $40\,^\circ\text{C}$.

5.2.1. Radiation field of a single solar lamp in the test room

To assess how the radiation from a single lamp in the test room is distributed, a cardboard with an uniform surface and emissivity coefficient was placed in front of the lamp. The thermal imaging camera, as shown in Fig. 5.11 (left), displays the temperature distribution. The highest temperature, and thus the highest radiation intensity, is observed in the center. This demonstrates the necessity of conducting various tests with different sensor arrangements to eliminate the possibility of unequal radiation exposure among sensors. Fig. 5.11 (right) shows the same sensors used in the validation setup in a bus at measurement position 1. Due to the varying emissivity coefficients of the different surfaces, a direct comparison between them is not appropriate. However, some observations can be made: the currently used room temperature sensor appears relatively hot. The plastic and rubberized surface on the top of the plug and the knurled surfaces of the plug exhibit the highest temperatures. At sensor type B, only the rubberized surface on the top of the plug is directly radiated, while the knurled surface is not exposed to radiation and is therefore much cooler.
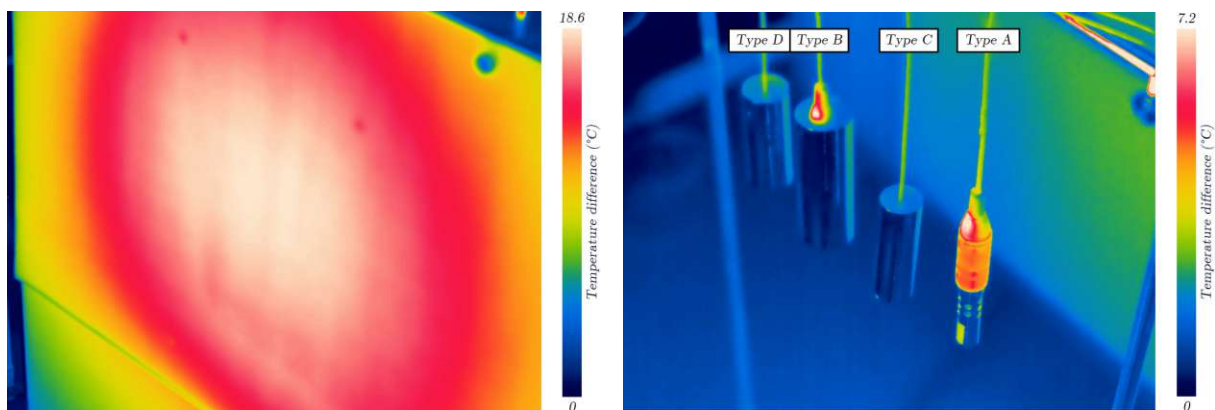
Figure 5.11.: Two images captured by a thermal imaging camera (FLIR T660) from the same perspective at $350\,\text{W/m}^2$. The scale indicates the temperature differences relative to the coldest surface. Note the differing scales. Left: Cardboard in front of the sensors. Right: Comparison of different sensors with varying radiation shields.

5.2.2. Measured radiation intensities in the climatic wind tunnel

To obtain comparable results in the test room to those in the wind tunnel, radiation intensities were measured in different vehicle types during the author's presence at RTA. The radiation intensity was measured using a portable solar radiation sensor (05-0001). The sensor was held at an angle of 30° to ensure that the solar rays shone perpendicular to the sensor, thereby detecting the maximum radiation. As shown in Tbl. 5.3, the radiation intensities inside the vehicles vary significantly depending on the calibrated radiation intensity outside the vehicle and the vehicle type, due to the different types and sizes of windows used in different vehicles.

Vehicle	Radiation int. outside (calibrated) $[W/m^2]$	Radiation int. seat (near window) $[W/m^2]$	Radiation int. aisle (height $1.1\,\mathrm{m}$) $[W/m^2]$	Radiation int. aisle (height $1.7\,\mathrm{m}$) $[W/m^2]$
Bus	500	98 / 136[1]	/	/
Railway 1	700	80	10	/
Tram	700	280	100	60
Railway 2	1050	180	60	5

[1] The radiation intensity varied along the bus between measurement position 1 and 2.

Table 5.3.: Measured radiation intensities in different vehicle types. Due to confidential information the exact vehicles can not be mentioned here.

The radiation intensity outside was measured between the solar radiation panel and the vehicle at two positions. The radiation intensity at the seat near the window was measured at the nearest position where a room temperature sensor was placed, which is critical for investigating the influence of radiation on temperature measurement. The radiation intensity in the aisle was measured at two heights in the center of the aisle and is essential for the relative humidity measurement, as described in Ch. 6. The specific height of importance depends on the vehicle type. Regional transportation vehicles measure the relative humidity at $1.1\,\mathrm{m}$ and long-distance transportation vehicles at $1.7\,\mathrm{m}$.

As indicated in Tbl. 5.3 the radiation intensity within the bus showed variation along the wind tunnel. Specifically, at the rear of the bus (measurement position 2), the radiation intensity was notably lower compared to the middle area (measurement position 1). This variation is likely caused by the deactivated lamps behind the bus, resulting in a reduction of diffuse radiation in that area.

It should be noted that these measurements were obtained over an extended period during the author's time at RTA and were not available right from the start.

5.2.3. General test room results

Fig. 5.12 and Fig. 5.13 present a selection of tested sensor and radiation shield configurations relevant for comparison with the simulation results and validation experiments performed in the wind tunnel. Measurements taken during the iterative development process are not presented, due to minor setup changes made during the course of the several months of measurements and the non-uniform radiation field of the lamp. Additionally, seasonal variations influenced the test environment: during winter, the heat from the lamp was absorbed by the concrete walls of the test room, whereas in summer, the air conditioning was required to cool the room. Therefore it is further not possible to directly compare test room measurements of the bus and rail vehicle tests, as they were made in winter and summer, respectively. Consequently, the wind tunnel validation results are presented and analyzed separately.

Each measurement lasted in total 70 minutes, with the solar simulation active for the first 60 minutes. To determine a representative temperature value for each sensor, the final 15 minutes of data, with the solar simulation active, were averaged.

Test room results of the bus arrangement

All measurements were performed twice under identical external conditions but with two different sensor arrangements. The results from both measurements were averaged to minimize the effects of variations in the non-uniform radiation field.

Fig. 5.12 presents the results of a measurement. To evaluate the performance of the different sensors, their temperature differences relative to the shaded reference sensor are compared.
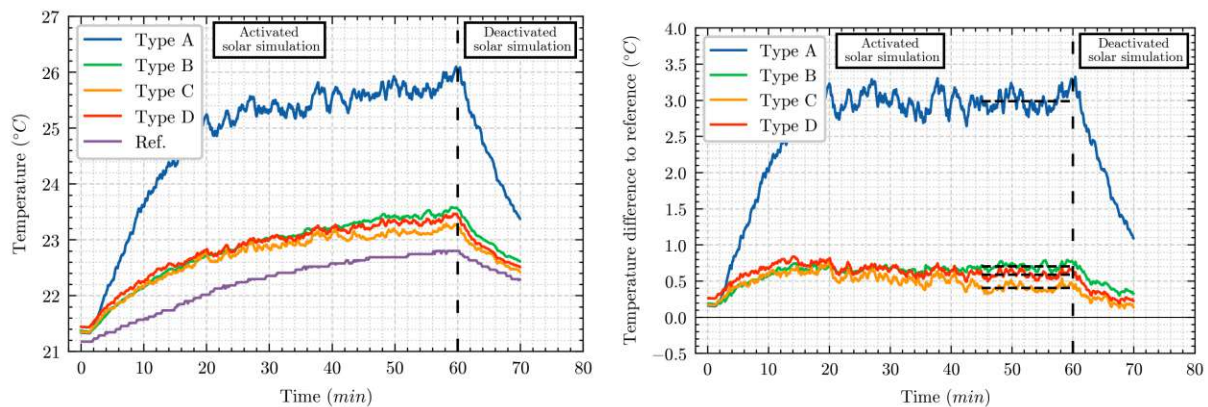
Figure 5.12.: Reference measurement for the bus at $350 \, \text{W/m}^2$ and with activated ventilation. Left: Absolute values. Right: Differences to reference sensor.

The figure on the left illustrates a steady increase in room temperature. The temperature differences relative to the shaded reference sensor stabilizes toward the end of the segment with an activated solar simulation. Once the solar simulation is deactivated (right of the

dashed line), these differences begin to decrease. Sensor type A shows a significantly larger deviation compared to the other sensor types, while the differences between types B, C, and D are minimal.

Tbl. 5.4 summarizes the results from the test room for the sensor types relevant to the subsequent bus analysis. The table presents the temperature differences relative to the shaded reference sensor.

Measurement	Radiation int. at sensors [W/m^2]	A [$°C$]	B [$°C$]	C [$°C$]	D [$°C$]
No ventilation	350	5.84	0.92	0.72	0.47
No ventilation	110	3.06	0.86	0.39	0.21
Ventilation	350	2.88	0.58	0.38	0.32
Ventilation	110	1.27	0.62	0.38	0.34

Table 5.4.: Comparison of the differences to the shaded reference sensor under various test conditions. When multiple measurements were taken with varying sensor arrangement, the results are averaged.

Sensor type A consistently exhibits significantly higher temperatures compared to all other sensor types under each measurement condition. While sensor types B, C, and D show smaller differences, type D demonstrates the least deviation from the reference sensor, indicating the best overall performance. Despite type B being shielded by a large-diameter tube, type D shows nearly half the temperature difference compared to the reference sensor. The difference between types C and D is relatively small, with deviations of $0.06\,°C$ and $0.04\,°C$ under conditions with active ventilation. In cases without ventilation, the differences are larger; however, the most relevant cases involve active ventilation, as ventilation is always active at customer measurements in the wind tunnel.

Test room results of the rail vehicle arrangement

Since only two sensor types were tested in the rail vehicle, no changes in sensor arrangement were required. Fig. 5.13 shows the measurements carried out in the test room.
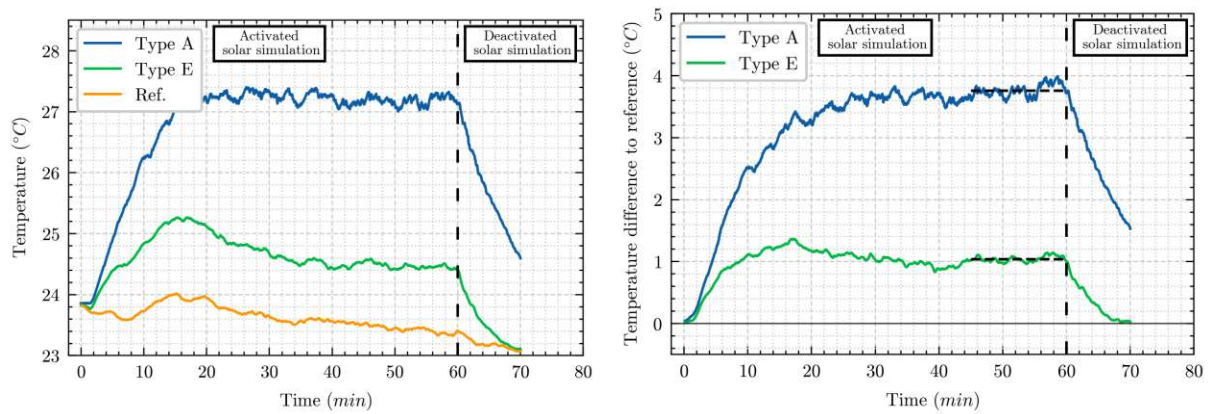
Figure 5.13.: Reference measurement for the rail vehicle at $350\,\mathrm{W/m^2}$ and with activated ventilation. Left: Absolute values. Right: Differences to reference sensor.

As shown in the left diagram, the activated air conditioning in the test room caused a reduction in the reference temperature during the measurement. At the end of the period with active solar simulation, the temperature differences to the shaded sensor, as can be seen in the right diagram, were $3.76\,°\mathrm{C}$ for type A and $1.04\,°\mathrm{C}$ for type E, indicating that type E is significant better. The larger difference observed for type A compared to the bus test can be attributed to the influence of the air conditioning. As previously mentioned, the test room measurements for the bus cannot be directly compared to those due to different conditions. Additional other not shown measurements performed with the air conditioning active also exhibited greater differences to the reference sensor compared to measurements taken in winter.

5.2.4. Validation results from the bus and comparison with the test room

As previously mentioned, the optimal configurations of the sensor and radiation shield available at that time were evaluated in a bus within the climatic wind tunnel. There were no dedicated tests to determine the performance of the sensors, therefore it was necessary to interpret the data at the test conditions from the RTA customer. The objective of the customer tests was to evaluate the heating and cooling performance of the vehicle under varying conditions, including an activated solar simulation panel. The tests also included door opening cycles with different air curtain settings at the doors. Given the limited time of an activated solar simulation panel at the tests, the radiation calibration at the beginning of the tests, performed with the bus in a standby mode, was also recorded. The conditions during this measurement were analogous to those in the test room with deactivated ventilation.

To quantify the performance of the different types, specific characteristic segments of the overall measurement were selected. These segments will be detailed below for measurement position 1, highlighting the differences compared to the used standard room temperature sensors (type A). Figures for measurement position 2, which showed similar results, along with figures showing the temperatures of all sensors, can be found in the appendix.

All measurements were performed at a sampling rate of one measurement per minute.

Segment 1: No ventilation

Fig. 5.14 illustrates the temperature deviations of the sensor types B, C and D from the average readings of sensors AT01 and AT05_Ext (type A). Prior to segment 1, temperature differences of approximately 0.4 °C were observed at types B, C and D. These discrepancies may be attributed to variations in the temperatures of the surrounding areas (the bus was moved inside the climatic wind tunnel about an hour before), leading to radiation from different temperatures, with the types B, C and D less influenced due to their low emissivity foil. In segment 1, different radiation intensities for the vehicle were calibrated. During this period, all sensors exhibited significantly lower temperatures compared to the standard room temperature sensors (type A), with type D, followed by type C, demonstrating the best performance. The greatest deviation occurred at the end of segment 1, at the highest measured radiation intensity. After the radiation was turned off, it took approximately 60 minutes for the temperature differences to return to the levels observed at the beginning. Fluctuations within this period were caused by the opening and closing of the bus doors. It is crucial to note that during this measurement period, the bus's ventilation and air conditioning systems were deactivated.
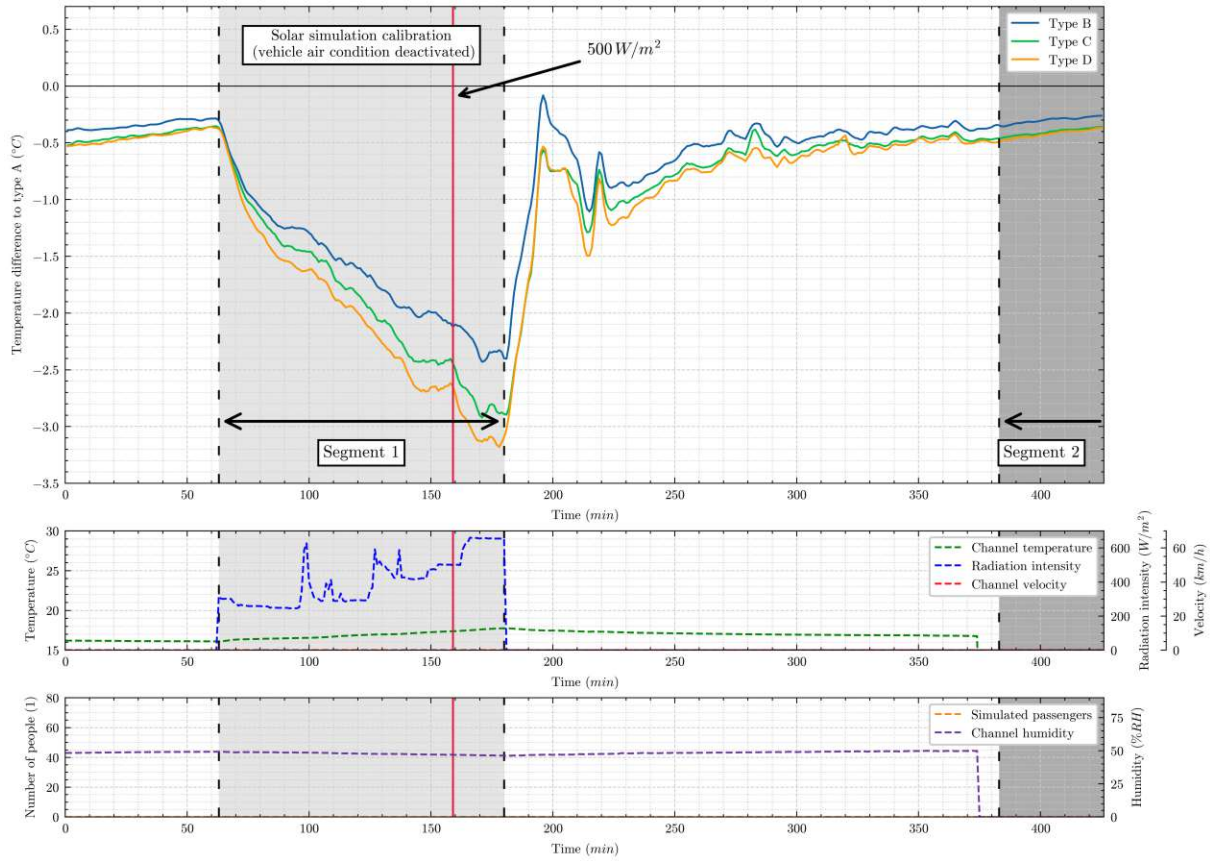
Figure 5.14.: Temperature differences relative to the sensor type A when the bus ventilation was deactivated.

A comparison between measurement position 1 and measurement position 2 (Fig. 5.15) reveals that the magnitudes recorded at measurement position 2 are consistently lower than those at measurement position 1. This discrepancy is attributed to the reduced radiation intensity encountered by the sensors at measurement position 2, as detailed in Sec. 5.2.2. This trend persists across all measurement segments. At both measurement positions, sensor type D demonstrated the best performance, followed by type C. Notably, although the sensor itself of type B is identical to type A, the application of a cylindrical radiation shield significantly enhances the performance.
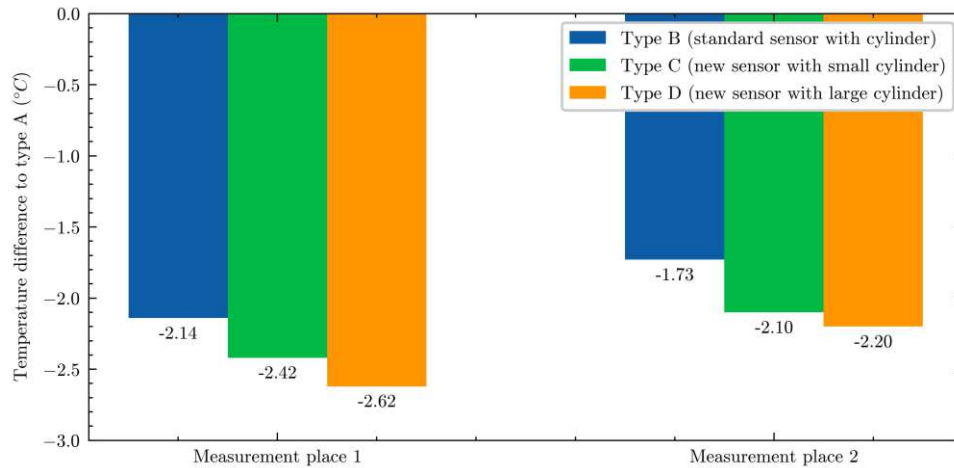
Figure 5.15.: Temperature differences relative to the sensor type A at the time indicated in Fig. 5.14, at a radiation intensity of $500\,\mathrm{W/m^2}$.

Segment 2: Thermal equilibrium

Segment 2 in Fig. 5.16 demonstrates that the temperature differences nearly vanish after an extended period. After this duration without somebody in the entire climatic wind tunnel for more than 30 hours, the wind tunnel and all equipment inside reached a uniform temperature, thereby eliminating heat exchange through radiation. As a result, the small surface emissivity of the aluminum foil becomes inconsequential. The remaining difference at the end of segment 2, the highest with $-0.06\,^\circ\mathrm{C}$, lies within the measurement uncertainty (Fig. 5.17).

It is important to note that since the climatic wind tunnel was deactivated, the measurement system stopped to record the environmental conditions within the tunnel, resulting in the nonexistence of data during this period.
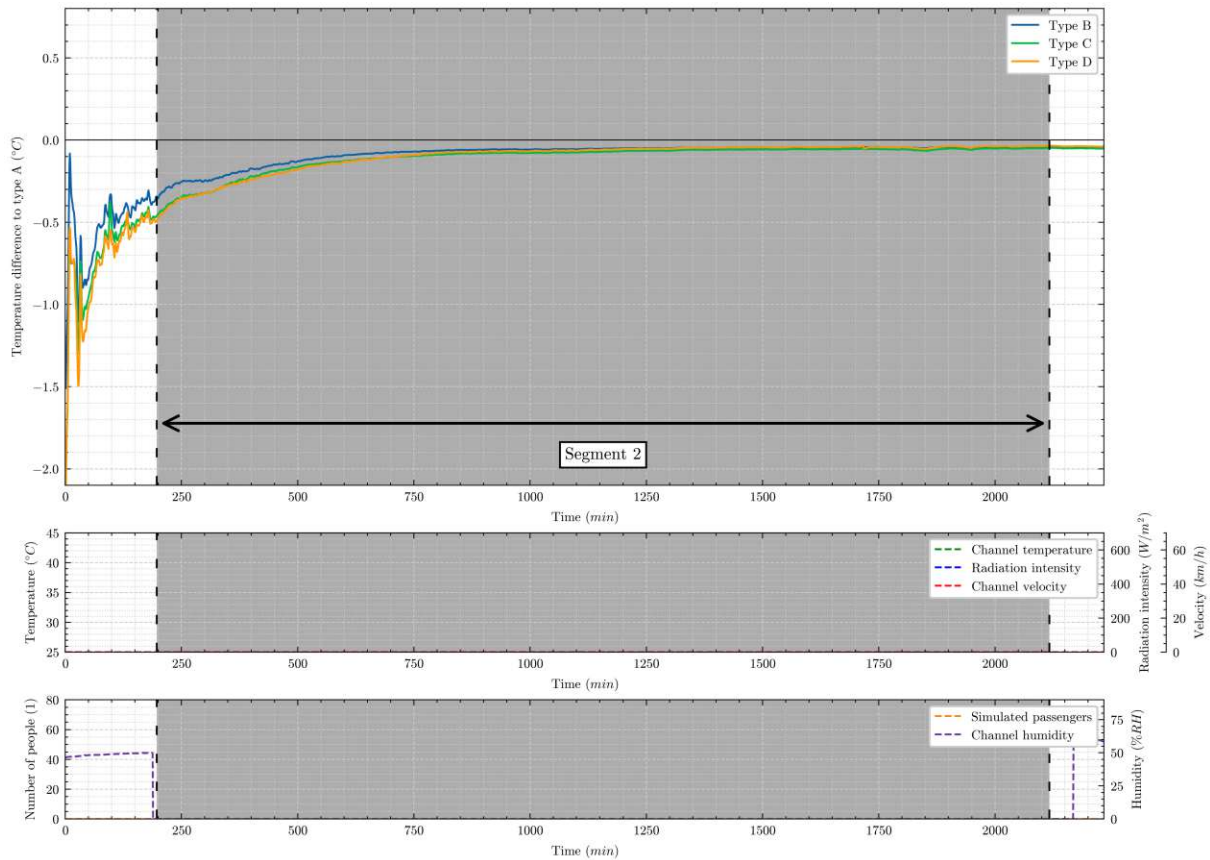
Figure 5.16.: Temperature differences relative to the sensor type A over an extended undisturbed period.
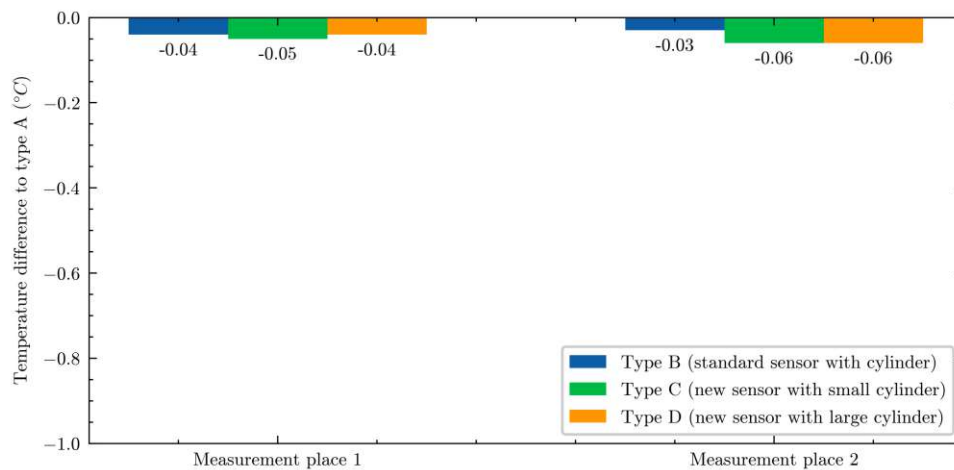
Figure 5.17.: Temperature differences relative to the sensor type A at the end of segment 2, indicating that at stationary conditions the temperature differences get negligible.

Segments 3 and 4: Door opening cycles

As the tests were carried out simultaneously with the RTA customer's evaluations, only limited segments were available for comparison, but in general, all sensors at one measurement position should exhibit the same temperatures, irrespective of the vehicle's state. Measurement position 2, as depicted in the appendix in Fig. A.3, also displays some upward fluctuations. These fluctuations result from a single door at the rear being opened with deactivated air curtains. Measurement position 1 remained unaffected due to its greater distance from this door.

During segments 3 and 4 in Fig. 5.18, the same environmental conditions were present, except from the door opening cycle and the radiation intensity which decreased from $500 \, \text{W/m}^2$ in segment 3 to $470 \, \text{W/m}^2$ in segment 4. The wavy nature of the curves can be attributed to the varying response times of the sensors. As shown in the appendix at a diagram with the temperatures of all sensors (Fig. A.9), sensor type A exhibits the slowest response time among all sensors, which contributes to the observed wave pattern in the differences. Type B exhibits the smallest wave magnitude and reacts more like type A due to its comparably high heat capacity. Conversely, type C and type D, having the least heat capacity, react faster, resulting in a more pronounced wave pattern.

Between segments 3 and 4, the ambient temperature in the wind tunnel changed significantly, and the vehicle's state was altered to some atypical conditions. Therefore, this segment is not representative for analyzing the performance of the different types. It is also observable that the differences to the type A diminish to nearly zero once the radiation and passenger simulation are deactivated, as seen from minute 970 onward.
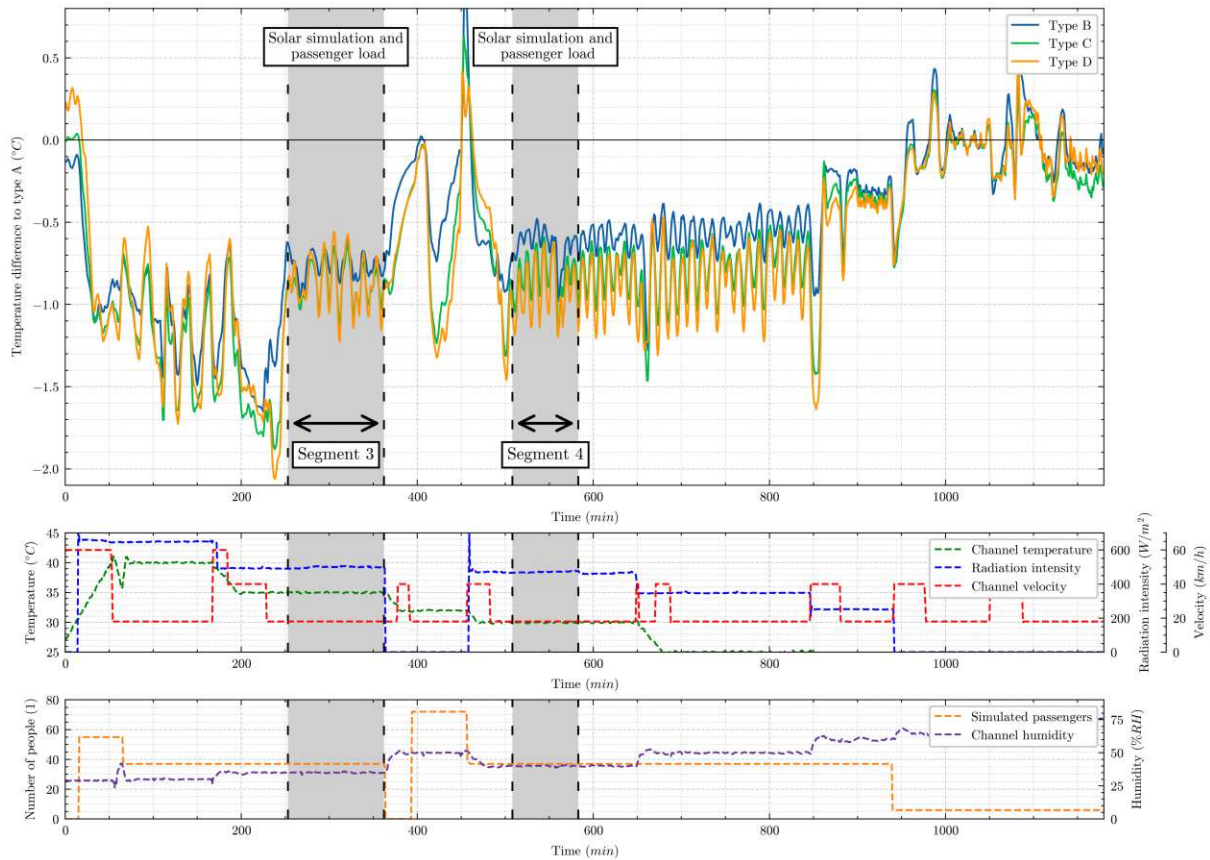
Figure 5.18.: Temperature differences relative to the sensor type A during a measurement involving solar radiation and various door opening cycles.
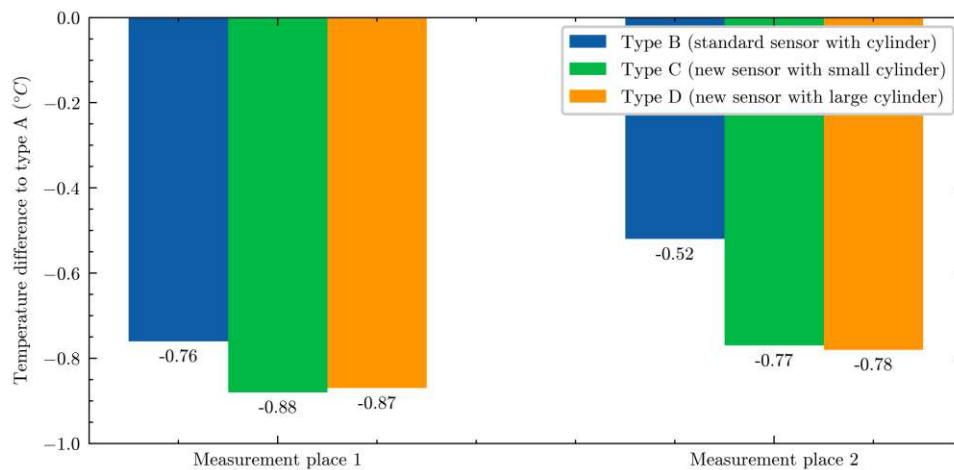
Figure 5.19.: Average temperature differences relative to the sensor type A in segment 3 at both measurement positions.
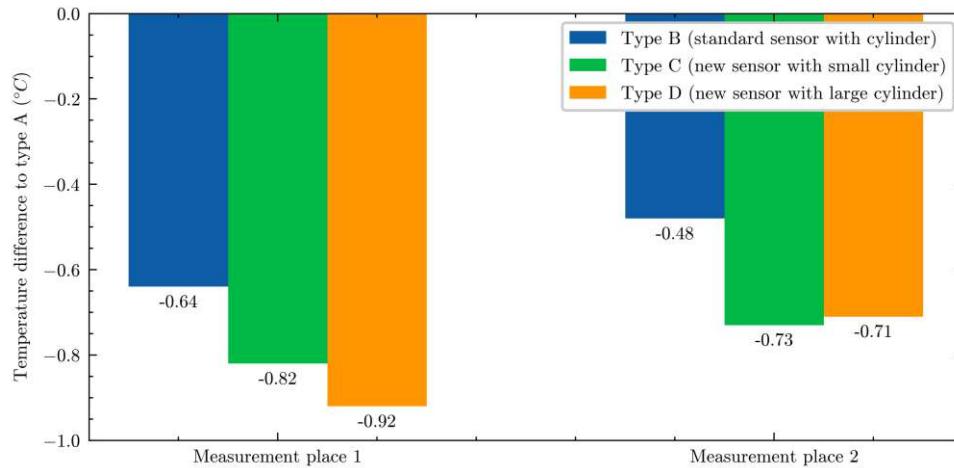
Figure 5.20.: Average temperature differences relative to the sensor type A in segment 4 at both measurement positions.

Fig. 5.19 illustrates that during segment 3, the performance of types C and D is comparable. Sensor type B consistently demonstrates lower performance compared to types C and D. When contrasted with segment 1, the observed temperature magnitudes are smaller, with a maximum difference of $-2.62\,°\mathrm{C}$ in segment 1 and a maximum difference of $-0.88\,°\mathrm{C}$ in segment 3. This reduction in magnitude can be attributed to the activation of the bus's air conditioning and ventilation systems during segment 3. A similar trend is observed in segment 4, as depicted in Fig. 5.20. When comparing the magnitudes between segment 3 and segment 4, a slight decrease is observed with the exception of type D at measurement position 1. This reduction is likely due to the slight decrease in the calibrated radiation intensity from $500\,\mathrm{W/m^2}$ in segment 3 to $470\,\mathrm{W/m^2}$ in segment 4, which results in a decrease in the radiation intensity inside the bus.

Summary and comparison with the test room

Tbl. 5.5 provides a summary of the results from the various segments defined earlier. Overall, measurement position 2 exhibits smaller deviations from the standard temperature sensor (type A), due to the lower radiation intensity at that position. Another significant observation is the difference between segment 1 and segments 3 and 4, with a discrepancy of approximately a factor of 3 between them. This variation highlights the substantial influence of the vehicle's air conditioning system on the measurements.

Measurement	Radiation int. at sensors [W/m^2]	Measurement pos. 1			Measurement pos. 2		
		B [$°C$]	C [$°C$]	D [$°C$]	B [$°C$]	C [$°C$]	D [$°C$]
Sec. 1: No ventilation	136 / 98	-2.14	-2.42	-2.62	-1.73	-2.10	-2.20
Sec. 2: Thermal equilibrium	0	-0.04	-0.05	-0.04	-0.03	-0.06	-0.06
Sec. 3: Door opening cycle	136 / 98	-0.76	-0.88	-0.87	-0.52	-0.77	-0.78
Sec. 4: Door opening cycle	$\approx$ 136 / 98[1]	-0.64	-0.82	-0.92	-0.48	-0.73	-0.71

[1] Radiation intensity at the sensors was slightly lower (see Sec. 5.2.2 for details)

Table 5.5.: Comparison of the differences to the type A at various measurements in the bus. Measurement position 2 experienced lower radiation, resulting in smaller temperature deviations.

Tbl. 5.6 presents a summary of the deviations from the type A sensor observed in the test room. Since it was only in the test room possible to position a temperature sensor in a shaded area, but still within the same thermal environment, the differences relative to this shaded sensor are also provided. This shaded sensor represents the benchmark for the maximum effectiveness that an ideal radiation shield can achieve.

The smallest deviations occurred at the measurement with active ventilation at a radiation intensity of $110 \, W/m^2$. This scenario most closely replicates the actual conditions within the climatic wind tunnel, as usually all vehicles tested in the wind tunnel operate with active ventilation. Additionally, both measurements performed without ventilation exhibit differences that are more than twice as large compared to those with ventilation.

Measurement	Radiation int. at sensors [W/m^2]	B [$°C$]	C [$°C$]	D [$°C$]	Shaded sensor [$°C$]
No ventilation	350	-4.92	-5.12	-5.37	-5.84
No ventilation	110	-2.20	-2.67	-2.85	-3.06
Ventilation	350	-2.30	-2.5	-2.56	-2.88
Ventilation	110	-0.65	-0.89	-0.93	-1.27

Table 5.6.: Comparison of the differences to the type A in the test room at different conditions. All values show the difference to the type A standard room temperature sensor.

A comparison between the wind tunnel results and those from the test room is possible. Segment 3 from the wind tunnel can be compared with the test room measurement performed with ventilation at $110 \, W/m^2$. Segment 4, however, is not suitable for comparison, as the actual radiation intensity at the sensors is slightly lower and not precisely known. Consequently, the comparison focuses on segment 3 and the test room results, as depicted in Fig. 5.21.

Overall, the measurements produce quite similar outcomes. Sensor type B consistently exhibits the smallest magnitude across all measurements, indicating that it has the least effective radiation shield compared to types C and D. For both types C and D, the test room results are comparable to those at measurement position 1, whereas the magnitudes at measurement position 2 are lower, despite the reduced radiation intensity in the test room. This suggests that the test room tends to overestimate the magnitudes slightly.
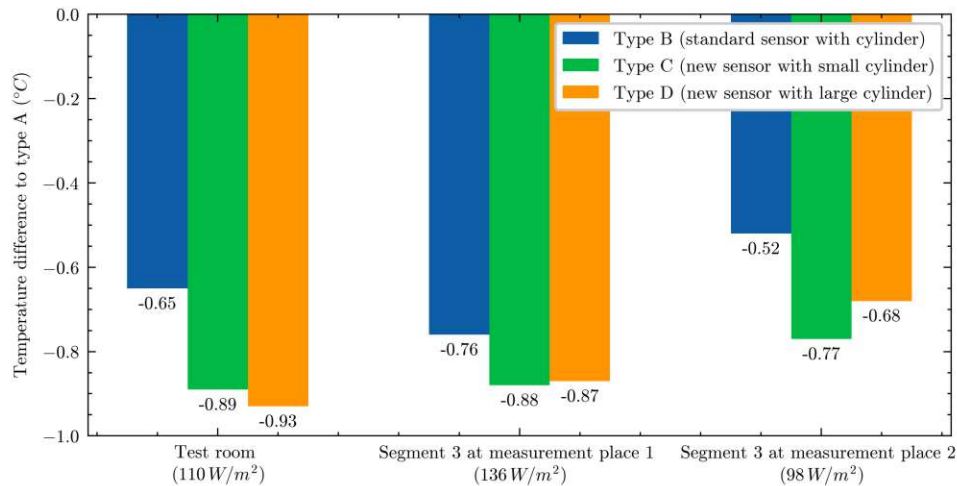
Figure 5.21.: Summary of the temperature differences at similar conditions (ventilated).

Segment 1 from the wind tunnel can be directly compared with the measurement without ventilation at $110\,\mathrm{W/m^2}$, as illustrated in Fig. 5.22. Sensor type B again demonstrates the smallest magnitude in comparison to types C and D. Both types C and D exhibit higher magnitudes in the test room relative to measurement position 1, further indicating that the test room conditions tend to overestimate the influence of the radiation shields slightly.
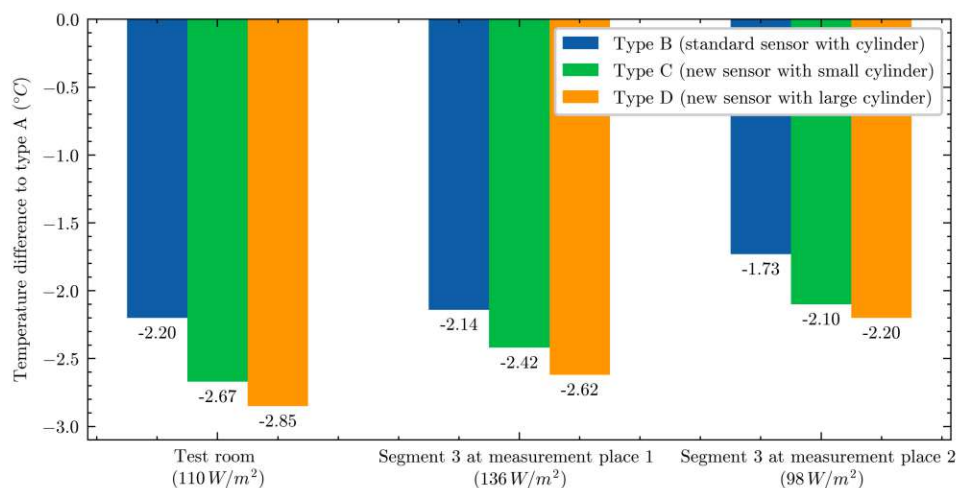

Figure 5.22.: Summary of the temperature differences at similar conditions (no ventilation).

5.2.5. Validation results from the rail vehicle and comparison with the test room

Based on the results obtained from the bus tests, the iterative process of developing a new radiation shield and testing it in the test room was restarted. A new radiation shield has been developed, offering several advantages over those previously tested in the bus. To validate the performance of this new type a vehicle that was undergoing testing at the time in the climatic wind tunnel was used. This vehicle was a long-distance railway vehicle exposed to radiation intensities up to $1050\,\text{W/m}^2$. The sampling rate at these measurements was twelve measurements per minute. To assess the performance of the newly developed sensor type, various segments were selected for analysis. The differences between the currently used type A at RTA and the newly developed type E are presented below. Additional diagrams, including temperature data from all sensors, are provided in the appendix. The analysis initially focuses on qualitative results, with quantitative results discussed in the summary.

Segment 1 - segment 6: Various conditions

Fig. 5.23 presents the data from various typical segments. Although both the passenger load and solar simulation were deactivated in segment 1, temperature differences were still observed. This phenomenon is likely attributable to the high channel temperature of approximately $40\,^\circ\text{C}$, which caused radiation from temperature differences to be emitted through the windows to the sensors. The lowest differences were recorded at measurement position 3, which was behind an insulated wall without any window and therefore not radiated, while the other measurement positions exhibited similar differences.

At the start of segment 2, the passenger load was activated, resulting in an increase in the magnitude of the differences by approximately $0.3\,^\circ\text{C}$ across all measurement positions. This suggests that the passenger simulation has a significant influence on temperature readings of different sensor types. It is also noteworthy that the wind speed in the chamber during segment 2 was significantly higher, at $120\,\text{km/h}$, compared to previous segments.

In segment 3, the solar simulation was activated with a radiation intensity of $750\,\text{W/m}^2$. This led to a significant increase in the magnitude of the differences at measurement positions 1 and 2, which were most exposed to radiation, while the magnitude of the difference at measurement position 3 remained nearly constant. The constant difference at measurement position 3, which is shaded by a wall, can likely be attributed to the passenger load and possibly to the closer position of type A to the heat mat. This is further supported by the results observed in segments 9 and 10.

Segment 4 highlights the differing response times of the sensors and is described in more detail in Fig. 5.24 below.

Segments 5 and 6 are analogous to segments 2 and 3. In segment 5, only the passenger load was activated, whereas in segment 6, the solar simulation panel was also active, though with a reduced radiation intensity of $650\,\text{W/m}^2$. As observed previously in segments 2 and 3, measurement position 3 exhibited similar magnitudes of difference in both

segments, reinforcing the hypothesis that these differences are primarily due to the heat mats and the closer proximity of type A to the heat mats. The magnitudes of the differences in segment 5 were higher compared to segment 2, likely because the vehicle was not fully heated up at the start of segment 2, as the temperature was increased only during the last 4.5 hours prior to the start of segment 1. By the time segment 5 began, the vehicle had more time to reach thermal equilibrium, leading to higher wall temperatures inside the rail vehicle, which in turn contributed to the increased magnitudes of differences compared to segment 2.

Figure 5.23.: Temperature differences relative to the sensor type A at various measurement positions during a typical test campaign.

Segment 4 in Fig. 5.24 illustrates the response times of sensor types A and E at measurement positions 1 and 2. It is evident that type E exhibits faster response times with more pronounced peaks and troughs, while type A demonstrates a more damped response. This difference can be attributed to the thermal inertia inherent to each sensor type.

Sensor type A incorporates a heavy Tuchel plug and a brass radiation shield, both of which contribute significantly to its thermal inertia. In contrast, the newly developed type E utilizes a lightweight Renk plug and a small plastic radiation shield, resulting in a substantially lower heat capacity and, consequently, reduced thermal inertia. Measurement positions 3 and 4 exhibit similar trends, as shown in the appendix in Fig. A.12.
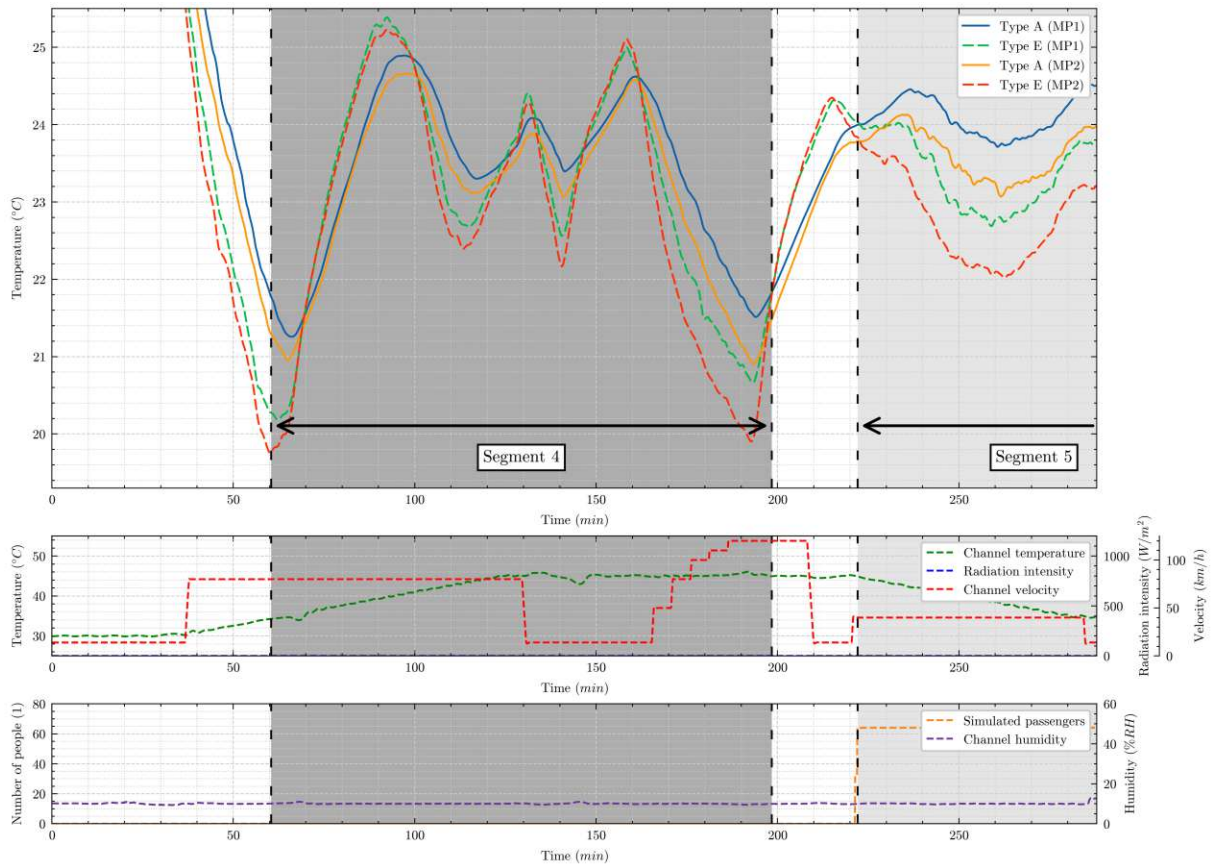
Figure 5.24.: Temperatures at measurement positions 1 and 2 during a test with changing conditions. Sensors of type E measure more extreme highs and lows, whereas sensors of type A are more damped.

Segment 7: Switched off climatic wind tunnel

Fig. 5.25 illustrates the decline in temperature differences in segment 7 when both the wind tunnel and the vehicle were deactivated, without persons present inside the vehicle. The residual differences, which are less than $0.1\,°C$, can be attributed to measurement uncertainties.
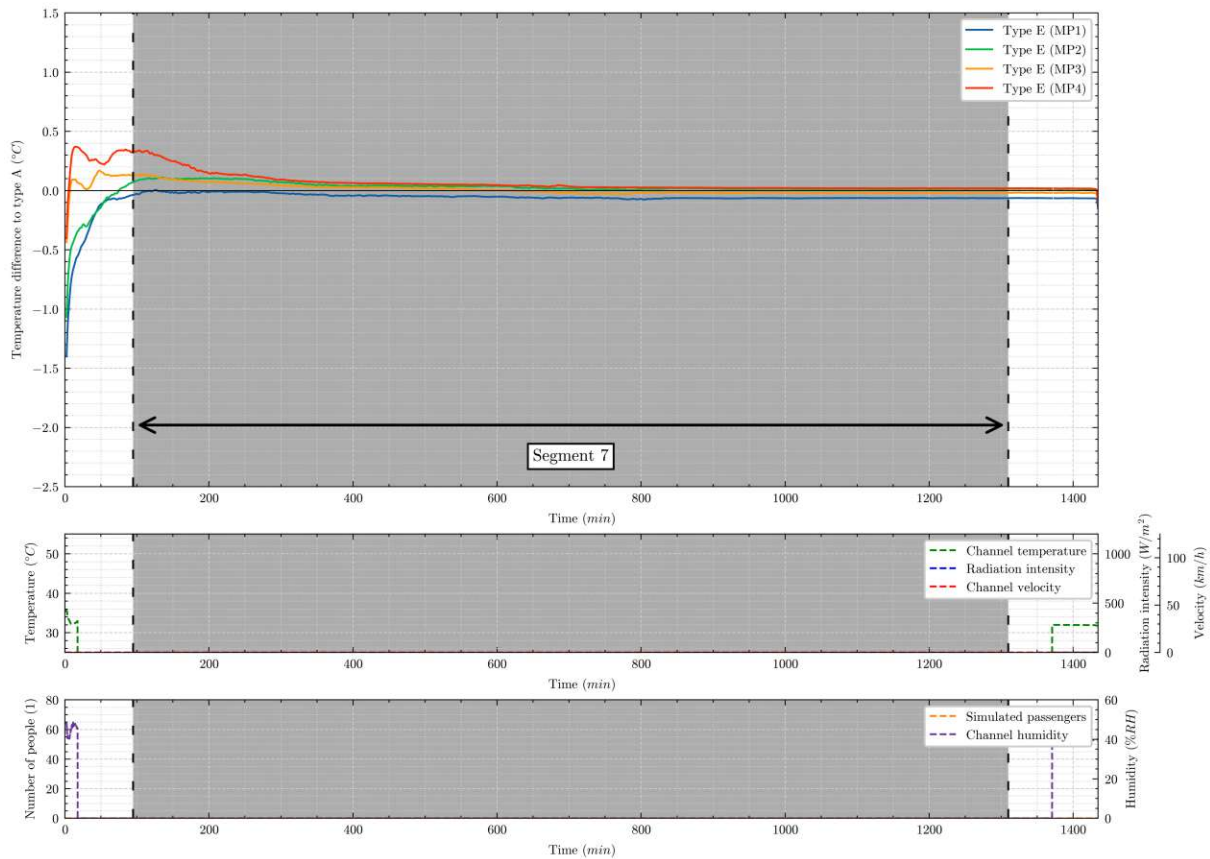
Figure 5.25.: Temperature differences relative to the sensor type A at various measurement positions over an extended undisturbed period.

Segment 8: Radiation intensity of 1050 W/m²

This segment presents the differences observed under the highest radiation intensity achievable with the installed lamps of the solar simulation panel. Notably, measurement positions 1 and 2 exhibit significant differences, compared to the other measurement positions. In general measurement position 4 displays greater magnitudes of difference compared to measurement position 3, suggesting a higher level of radiation at that position.
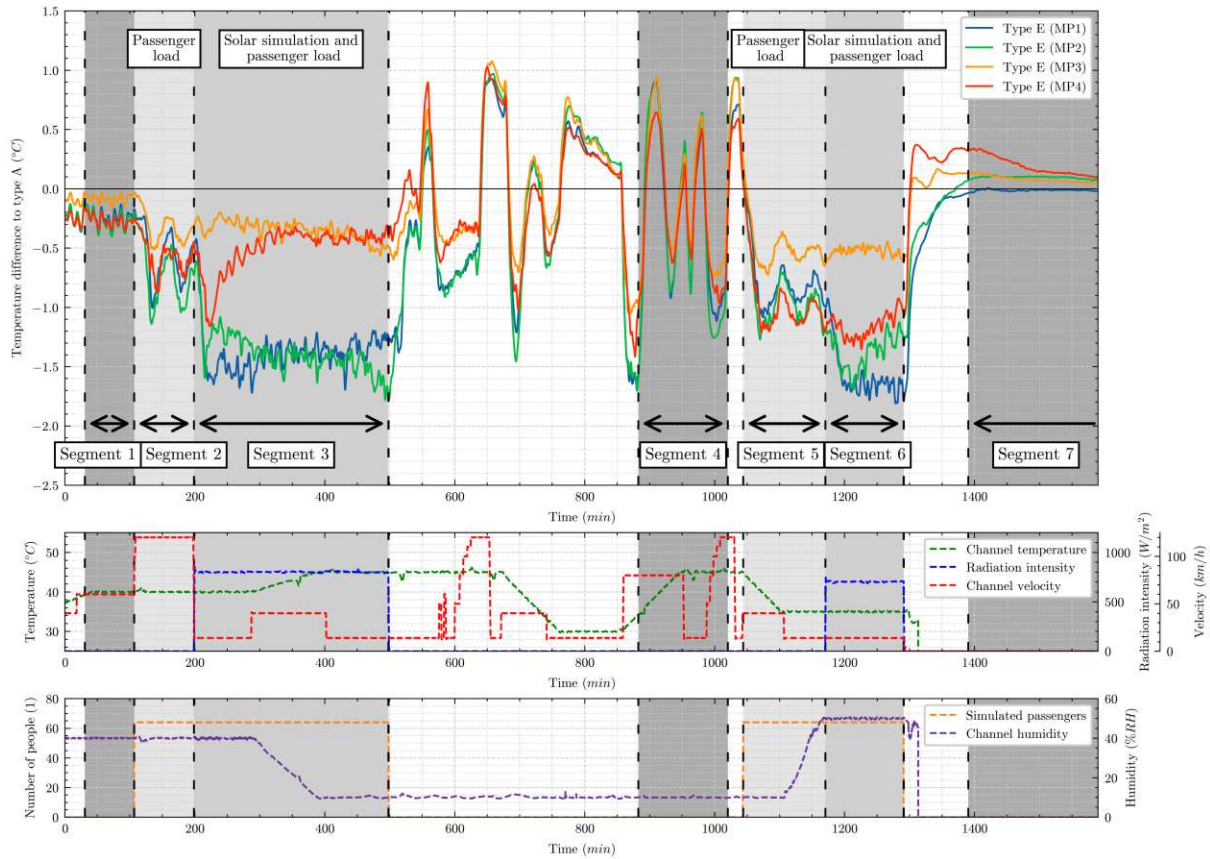
Figure 5.26.: Temperature differences relative to the sensor type A at various measurement positions during a typical test campaign.

Segment 9 - 11: Position change of type A and E

Fig. 5.27 presents the measurements before and after the respective positions of type A and E were swapped at measurement position 2. The purpose of this position change was to investigate the influence of the heat mat. Prior to the swap, all sensors of type A were positioned 10 cm away from the seat, and consequently from the heat mat, while all sensors of type E were positioned 25 cm away from the heat mat. To evaluate the effect of this swap, two segments with similar conditions were defined. Unfortunately, minor conversion work carried out by the customer between the tests prevents a direct comparison of these segments, as indicated by the data from measurement position 1. Despite nearly identical external conditions of segments 9 and 11, measurement position 1 shows a higher difference in magnitude, suggesting that the changes introduced had an impact on the observed differences.

Fig. 5.27 also depicts a brief period during which the passenger simulation was deactivated while the solar simulation remained active (Segment 10), just before the position swap — the only such occurrence during the entire measurement campaign. During this period, the magnitudes of the differences changed notably at measurement positions 3 and 4, whereas measurement positions 1 and 2 exhibited differences within the same range as those observed before and after this period. This observation suggests that the heat mats also have a measurable influence on the results.
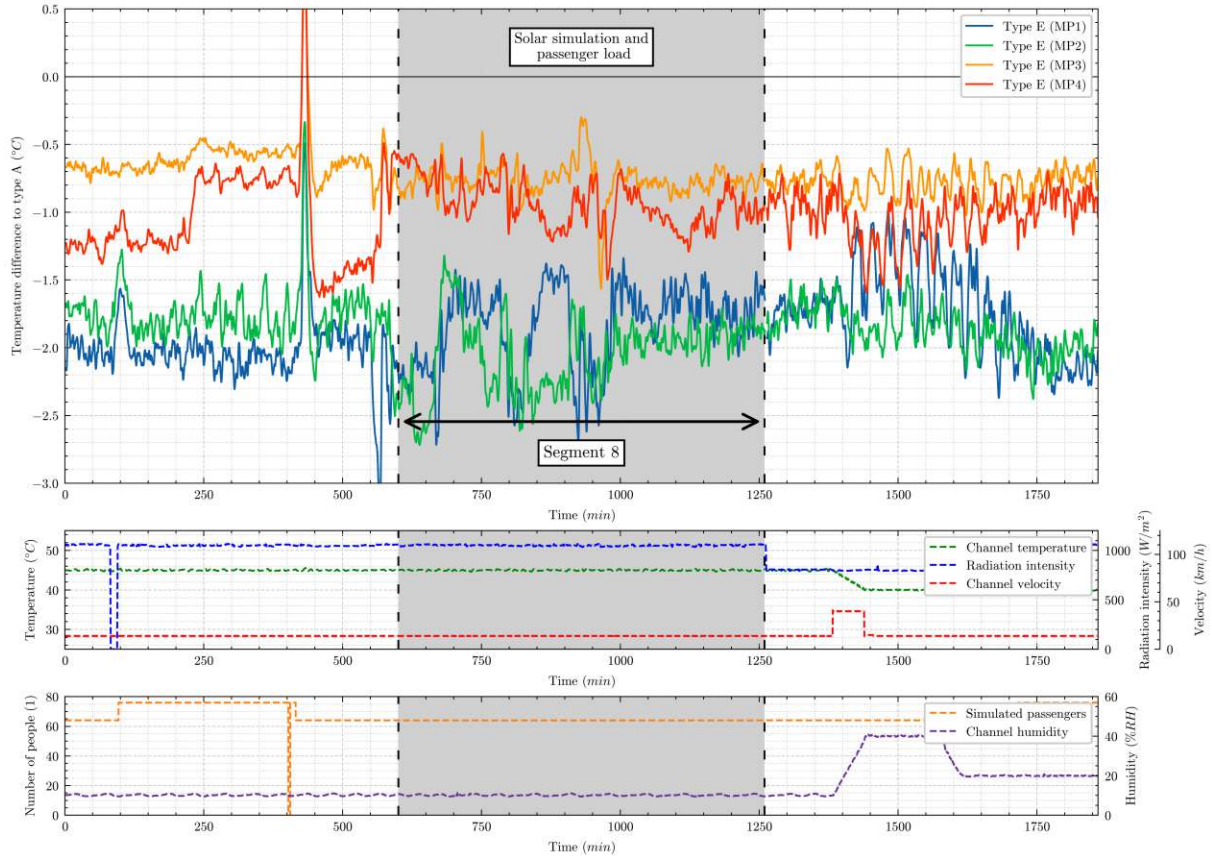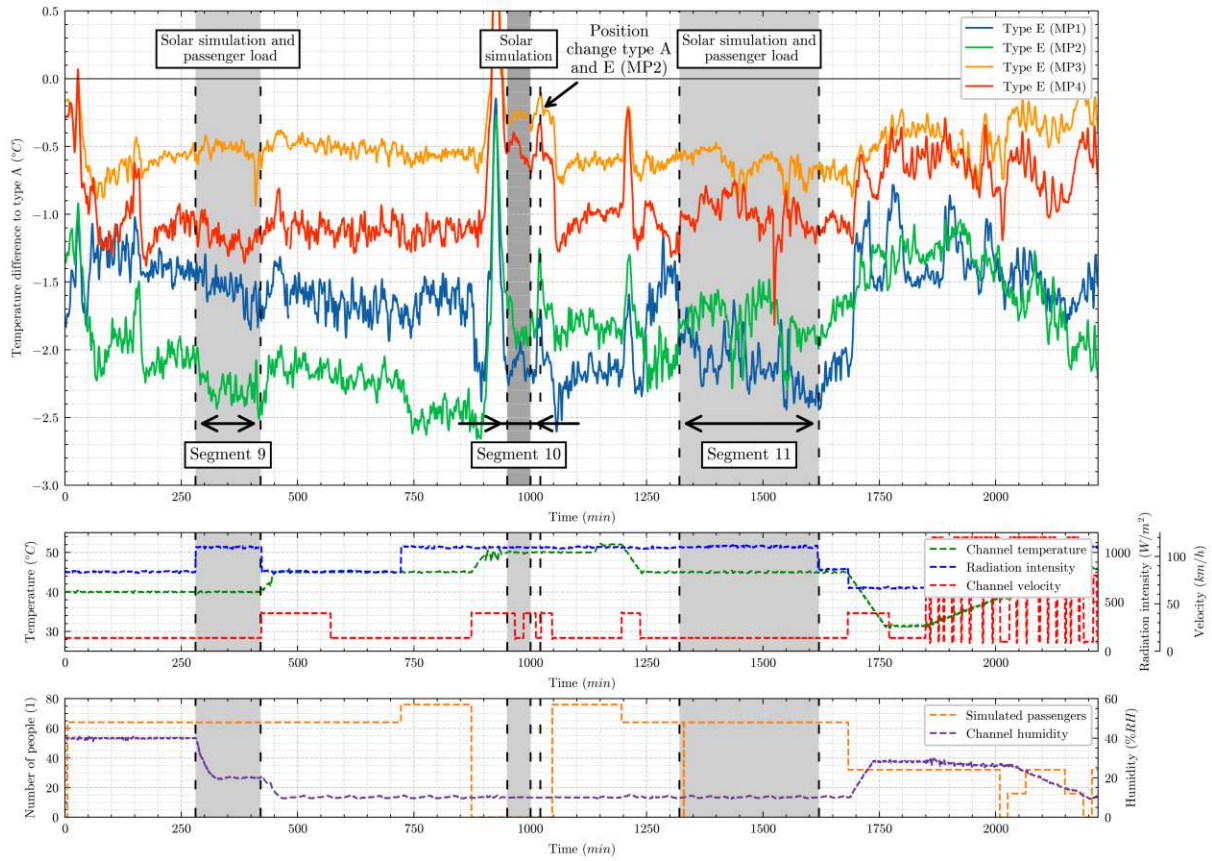
Figure 5.27.: Temperature differences relative to the sensor type A at various measurement positions during a typical test campaign.

Summary and comparison with the test room

Tbl. 5.7 presents the quantitative results for each segment and measurement position. The values represent the average value for each segment, with the exception of segment 7, where the results from the end of the segment are reported. The radiation intensity at measurement positions 1 and 2 depends on the calibrated radiation intensity, which for a calibrated value of $1050\,\mathrm{W/m^2}$ corresponds to $180\,\mathrm{W/m^2}$, as indicated in Tbl. 5.3. At lower calibrated radiation intensities, one can assume that the radiation intensity observed at the sensors decreases proportionally.

Measurement	Passenger load[1]	Calibrated radiation int.	MP1	MP2	MP3	MP4
	[1]	$[W/m^2]$	$[°C]$	$[°C]$	$[°C]$	$[°C]$
Segment 1	0	0	-0.24	-0.27	-0.09	-0.27
Segment 2	64	0	-0.55	-0.72	-0.32	-0.56
Segment 3	64	800	-1.38	-1.38	-0.35	-0.50
Segment 4	0	0	/	/	/	/
Segment 5	64	0	-0.79	-0.92	-0.50	-0.96
Segment 6	64	700	-1.57	-1.37	-0.52	-1.15
Segment 7	0	0	-0.06	0.02	-0.02	0.02
Segment 8	64	1050	-1.84	-2.05	-0.77	-0.94
Segment 9	64	1050	-1.56	-2.28	-0.54	-1.17
Segment 10	0	1050	-2.12	-1.84	-0.28	-0.53
Segment 11	64	1050	-2.11	-1.79	-0.64	-1.00

[1] Number of passengers simulated with heat mats and humidifiers.

Table 5.7.: Comparison of the differences to the type A at various measurements in the railway vehicle. Measurement positions 1 and 2 were next to the window in the same way. Measurement position 3 was on the same side of the aisle but behind a wall and measurement position 4 was on the other side of the aisle. Due to different vehicle states in each segment these measurements have uncertainties.

In general, measurement position 3, located behind the wall, consistently shows the smallest differences across all segments, even when there is only a temperature gradient between the compartment and the wind tunnel without solar radiation. When radiation is present, measurement position 4, situated further from the solar simulation panel, exhibits significantly lower differences in magnitude compared to measurement positions 1 and 2. Without radiation, the differences between these positions are quite similar. Despite the identical setup of measurement positions 1 and 2, discrepancies are observed in the results. From segment 1 to segment 8, the differences recorded by both measurement positions did not exceed $0.21\,°C$. However, in segments 9, 10 and 11, the differences between measurement positions 1 and 2 were notably larger. As previously mentioned in Sec. 5.2.5, minor conversion work was carried out, which likely influences the comparability between those segments.

5.3. Simulation setups

To investigate the qualitative processes occurring when the sensors are exposed to solar radiation, a CFD model was developed using ANSYS Fluent 2024 R1. The model was initially developed with sensor type D and subsequently applied to sensor types A and E.

5.3.1. Simulation objective

The objective was to simulate the impact of solar radiation on the sensors and to analyze the heat transfer from the sensor components to the surrounding air. The exposure to radiation increases the air temperature around the sensors, leading to natural convection. In steady-state conditions, a balance must be achieved between the energy absorbed from solar radiation and the energy carried outside of the simulation domain by natural convection. The effects of forced convection, as it would occur in reality, were not considered in this model due to a lack of information regarding it. The key performance metric in this analysis is the temperature difference between the sensor tip and the inlet air temperature.

5.3.2. Models involved

The following models were employed in the simulation:
- **Energy:** The energy equation was solved to analyze the heat transfer within the domain. All three modes of heat transfer, conduction, convection, and radiation, are present in this model.
- **Viscous:** This flow is solely buoyancy driven and the corresponding Rayleigh number (Ra) is calculated as:

$$\text{Ra} = \frac{g\,\beta\,\Delta T\,L^3}{\nu\,a} = \frac{9.81\,\text{m/s}^2 \cdot 3.4 \times 10^{-3}\,1/\text{K} \cdot 10\,\text{K} \cdot (0.15\,\text{m})^3}{1.49 \times 10^{-5}\,\text{m}^2/\text{s} \cdot 2.1 \times 10^{-5}\,\text{m}^2/\text{s}} \approx 3.6 \times 10^6 \ll 10^8$$

(5.1)

with $L = 0.15\,\text{m}$ as a typical length scale and a typical temperature difference of $10\,°\text{C}$. For all other quantities a temperature of $20\,°\text{C}$ and atmospheric pressure is assumed. As the Rayleigh number is significantly below 10^8, the flow is laminar, and no turbulence model is necessary [16].
- **Radiation:** The Discrete Ordinates (DO) model is used for radiation modeling. This model supports the use of semi-transparent walls and can be applied with non-gray radiation models, though this was not utilized in the present work. Opaque surfaces were characterized by their emissivity and a diffuse fraction parameter, which determines the proportion of reflected radiation that is diffuse. The remaining portion is reflected specularly. The angular discretization was set to six divisions for both theta and phi angles in each spatial octant, with two pixels for the theta and phi angle [16]. To speed up the simulation the DO model is solved every 7th iteration.

5.3.3. Simulation domain

The simulation domain consists of the respective temperature sensor and its radiation shield, along with the surrounding air. The sensor hangs within the domain by its cable, as it does in reality. All single components were assumed to be homogeneous and isotropic. Fig. 5.28 illustrates the simulation domains for all investigated sensor types.
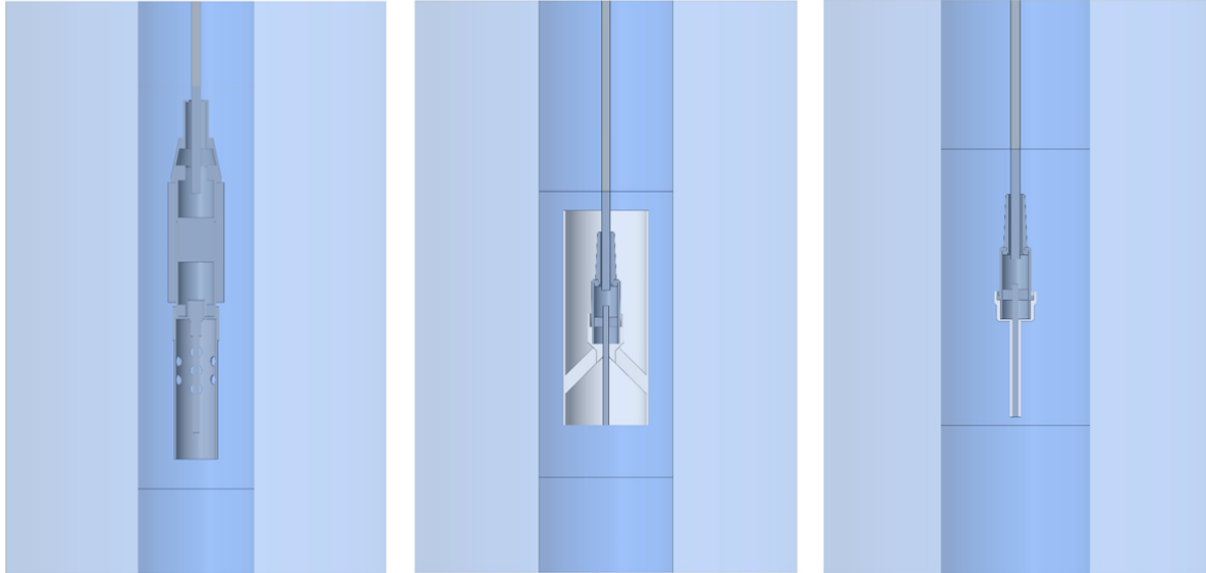
Figure 5.28.: Cross sections through the simulated domain of all sensor types. Left: Type A. Middle: Type D. Right: Type E.

All sensor types are composed of various components, each made from different materials with distinct thermal properties, summarized in Tbl 5.8 for sensor type A, and in Tbl. 5.9 for types D and E. Types D and E have the same sensor, differing only in their radiation shields manufactured from identical materials. Since radiative heat transfer between sensor components and the surrounding air is critical to the thermal performance, material properties such as the emissivity coefficient are of particular importance in the analysis.

Part	Material	Density ρ $[kg\,m^{-3}]$	Specific heat c_p $[J\,kg^{-1}K^{-1}]$	Thermal conductivity k $[W\,m^{-1}K^{-1}]$	Emissivity coefficient ϵ [1]	Diffuse fraction [1]
Cable	PVC	1380	900	0.16	0.90	0.9
Sensing element	1.4571	8000	500	10.00	0.50	0.4
Silicon tube	PLA	1140	1250	0.30	0.95	0.8
Plug insert	PVC	1400	1000	0.16	0.95	0.9
Plug housing	Steel	7850	470	47.70	0.90	0.9
Plug rubber	PVC-P	1380	850	0.16	0.95	0.9
Radiation shield[1]	Brass	8440	376	120.00	0.03	0.2

Note: Data for density, specific heat and thermal conductivity from [35], emissivity coefficients from [9, 36, 37]

[1] The radiation shield is chromium plated at all surfaces.

Table 5.8.: Material properties of different parts for the sensor type A.

Part	Material	Density ρ $[kg\,m^{-3}]$	Specific heat c_p $[J\,kg^{-1}K^{-1}]$	Thermal conductivity k $[W\,m^{-1}K^{-1}]$	Emissivity coefficient ϵ [1]	Diffuse fraction [1]
Cable	PVC	1380	900	0.16	0.90	0.9
Sensing element	1.4571	8000	500	10.00	0.50	0.4
Plug insert	PVC	1400	1000	0.16	0.95	0.9
Plug housing	1.0330	7850	112	30.00	0.20	0.4
Plug rubber	PVC-P	1380	850	0.16	0.95	0.9
Radiation shield[1]	PLA	1240	1600	0.13	0.80	0.5
Radiation shield[2]	PLA	1240	1600	0.13	0.03	0.2

Note: Data for density, specific heat and thermal conductivity from [35], emissivity coefficients from [9, 36, 37]

[1] For surfaces without aluminium foil.

[2] For surfaces with aluminium foil.

Table 5.9.: Material properties of different parts for the sensor types D and E.

5.3.4. Mesh

Due to the low flow velocities, the use of a turbulence model was not required, and consequently, no boundary layer refinement was applied. However, in areas where higher gradients were expected, a finer mesh was employed. The conformal mesh is composed of hexahedral and tetrahedral elements, with a particularly refined mesh in the region surrounding the sensor. Fig. 5.29 illustrates the grid of all sensor types.
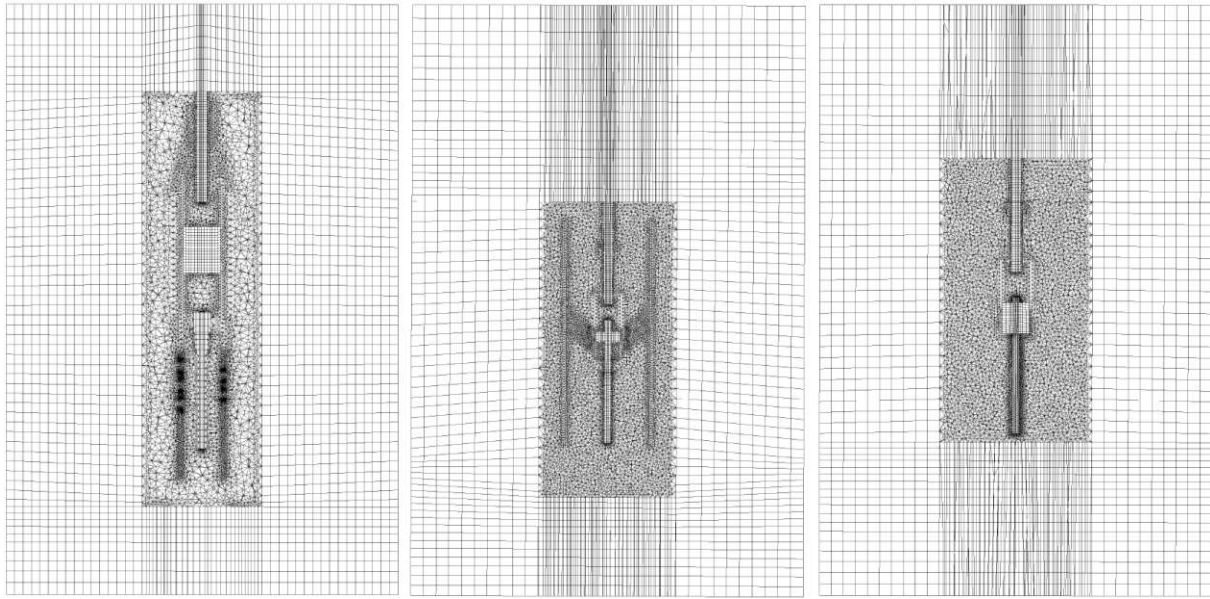
Figure 5.29.: Cross section through the cylindrical domain of the mesh. Left: Type A. Middle: Type D. Right: Type E.

5.3.5. Air properties

For the modeling of natural convection, the air density must vary with temperature. In this thesis, the approach of specifying the air density as an incompressible ideal gas was employed together with specifying the gravitational acceleration on Earth. Furthermore, operating conditions were defined, which are summarized in Tbl. 5.10 along with other relevant air properties.

Property	Value
Specified operating density	$1.204\,151\,29\,\text{kg m}^{-3}$
Operating temperature	$293.15\,\text{K}$
Operating pressure	$101\,325\,\text{Pa}$
Specific heat capacity	$1006.43\,\text{J kg}^{-1}\text{K}^{-1}$
Thermal conductivity	$0.0242\,\text{W m}^{-1}\text{K}^{-1}$
Viscosity	$1.7894 \times 10^{-5}\,\text{kg m}^{-1}\text{s}^{-1}$
Molecular weight	$28.966\,\text{kg kmol}^{-1}$
Absorption coefficient	$0\,\text{m}^{-1}$
Scattering coefficient	$0\,\text{m}^{-1}$
Refractive index	1

Table 5.10.: Air properties and operating conditions set in ANSYS Fluent.

5.3.6. Boundary conditions

The following boundary conditions were applied:

- **Wall:** A no-slip boundary condition is applied to all walls inside the domain. The thermal properties of each wall are coupled with the adjacent cell zones. The radiant surface properties are implemented as outlined in Tbl. 5.8 and 5.9, respectively.

- **Wall (cable top surface):** This is the only solid surface connected to the domain boundary. It is assumed that no heat is transferred out of the domain, thus the heat flux density is specified as $0\,\mathrm{W/m^2}$.

- **Pressure inlet:** This condition is applied to the bottom and side surfaces of the cylindrical domain. The gauge total pressure and the supersonic/initial gauge pressure are set to $0\,\mathrm{Pa}$, as recommended by the Fluent User Guide [38]. The inlet temperature is $293.15\,\mathrm{K}$. To account for solar radiation, the surface is set to transparent, allowing radiation to pass through. The direct radiation, applied parallel to a beam direction of 30° to the horizontal direction, and the diffuse radiation depend on the simulation setup, as specified in Tbl. 5.11. A beam width of 10^{-6} degree is chosen for both theta and phi angles.

- **Pressure outlet:** This boundary condition is applied to the top surface of the domain, excluding the cable surface. Natural convection drives the fluid to exit through the top, any backflow that occurs will adopt the inlet properties. The radiation settings at the pressure outlet are identical to those applied at the pressure inlets.

Depending on the simulation case, both direct and diffuse radiation were specified. The diffuse radiation was experimentally determined in the test chamber by positioning the portable pyranometer globe in the opposite direction to the radiation source. The following radiation values were measured:

Overall radiation int. $[W/m^2]$	Direct radiation int. $[W/m^2]$	Diffuse radiation int. $[W/m^2]$
110	105	5
350	339	11

Table 5.11.: Share of direct and diffuse radiation of the overall radiation.

5.3.7. Solver settings

For pressure-velocity coupling, the Coupled scheme was selected. Gradients were computed using the least-squares cell-based method, while pressure was discretized with a second-order scheme. The momentum, energy, and discrete ordinates equations were solved using a second-order upwind method.

5.3.8. Grid independence study

A grid independence study was performed for all sensor types under solar radiation of $350\,\mathrm{W/m^2}$, as illustrated in Fig. 5.30. The meshes for each type were based on the same

element length, yielding different total cell counts. For sensor type D, the mesh was refined to over 5 million cells, whereas the base meshes for types A and E did not exceed 1 million cells. In the end, the base meshes were used for the analysis.
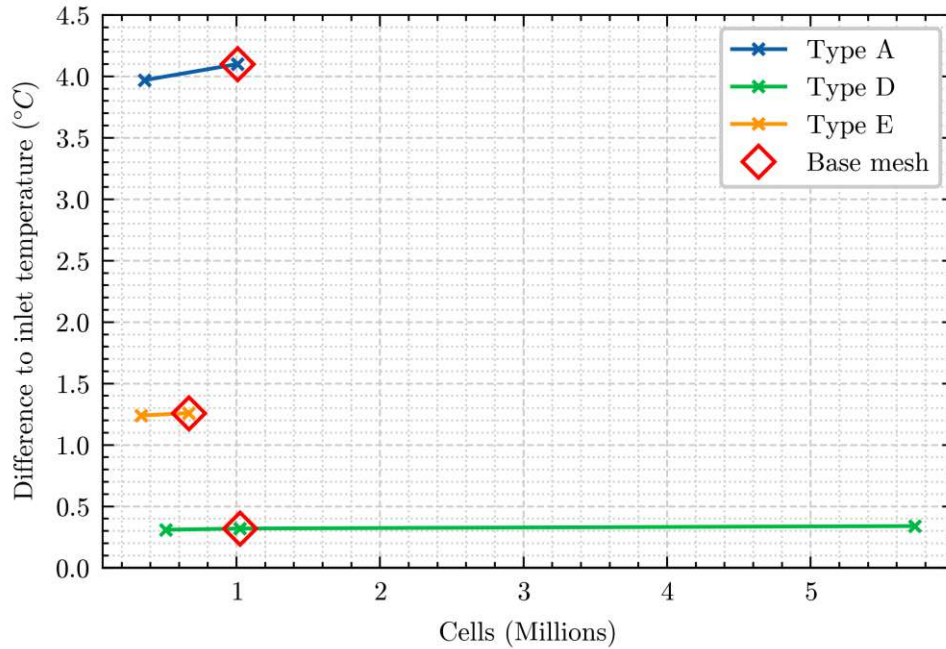

Figure 5.30.: Grid independence study carried out at $350 \, \text{W/m}^2$ for all sensor types.

5.4. Simulation results

Approximately 800 iterations were required for all residuals to fall below the defined threshold of 10^{-5}. Additionally, the surface-averaged temperature at the sensor tip reached convergence, showing no further variation. A subsequent transition to a transient simulation indicated that the root mean square values of both the velocity and temperature fields were lower than 10^{-3}, indicating a converged solution. The resulting plots for mean velocity magnitude, temperature distribution, and relative pressure are presented in the following sections.

5.4.1. Temperature

The stationary temperature field is illustrated in the following figures. It is obvious that regions far away from the sensor maintain the inlet temperature. Areas near the sensors heat up and conduct heat to areas in direct vicinity (Fig. 5.31 and Fig. 5.32). The elevated temperatures near the cables are attributed to the warmer convective upward flow.

The hottest regions for both sensor types A and E are the plug rubbers, which have a high emissivity constant and low thermal conductivity (Fig. 5.33 and Fig. 5.34). Conversely, sensor type D shows lower temperatures at the rubber due to its radiation shield. The radiation shield on type A is rather warm despite having the same emissivity constant as on the other types, caused primarily by the high thermal conductivity of its brass material, combined with poor airflow through the shield, which traps heat. The small ventilation holes in the shield are insufficient for generating an adequate cooling airflow.

For sensor type D, the top of the radiation shield experiences higher temperatures due to the high emissivity of its inner surface, while its outer surface, having a low emissivity constant, exhibits significantly lower temperatures.

The critical region for evaluating the performance is the sensor tip. The effectiveness of each sensor type is assessed by comparing the temperature at the sensor tip to the inlet air temperature. Therefore, one can see in Fig. 5.31 and Fig. 5.32 that sensor type A exhibits the poorest performance, followed by type E. Sensor type D demonstrates the best performance due to its large radiation shield from a low heat conducting material and the low emissivity on the shield's outer surface.
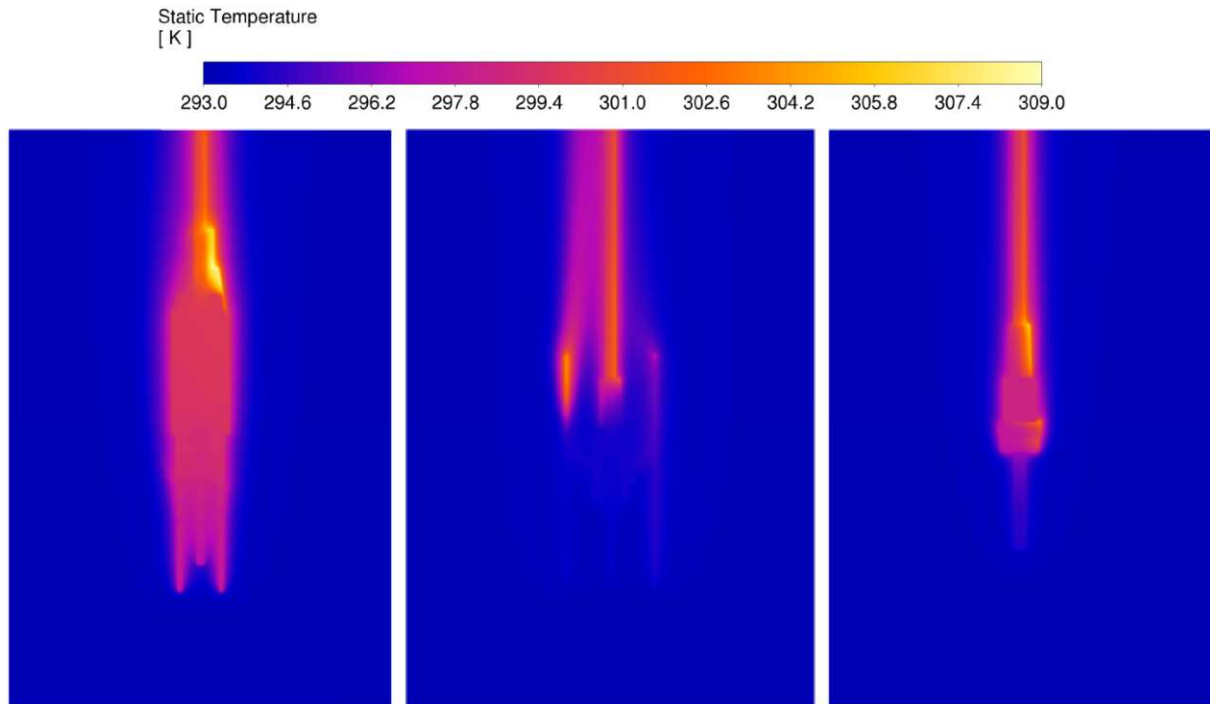
Figure 5.31.: Comparison of cross section temperatures at $350\,\mathrm{W/m^2}$. Solar radiation emitted from the top right corner at a 30° angle relative to the vertical. Left: Type A. Middle: Type D. Right: Type E.
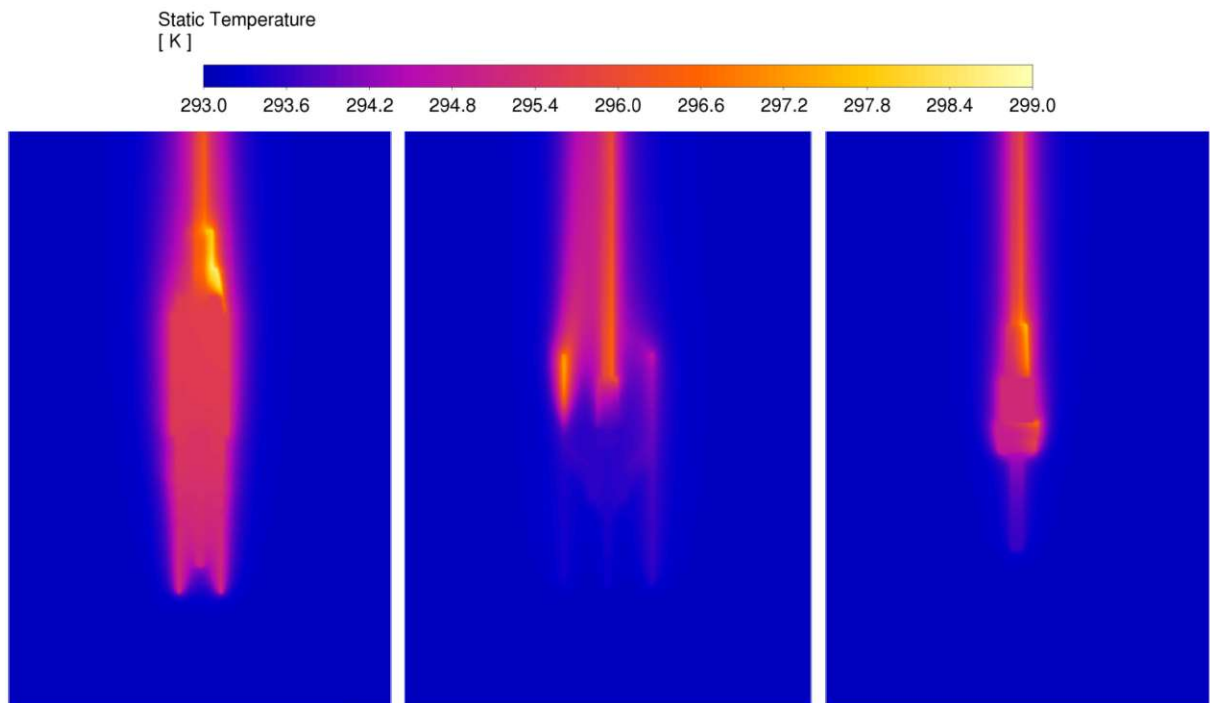
Figure 5.32.: Comparison of cross section temperatures at $110\,\mathrm{W/m^2}$. Solar radiation emitted from the top right corner at a 30° angle relative to the vertical. Left: Type A. Middle: Type D. Right: Type E.

Figure 5.33.: Comparison of the sensors surface temperatures at $350\,\mathrm{W/m^2}$. Solar radiation emitted from the top right corner at a 30° angle relative to the vertical. Left: Type A. Middle: Type D. Right: Type E.

Figure 5.34.: Comparison of the sensors surface temperatures at $110\,\mathrm{W/m^2}$. Solar radiation emitted from the top right corner at a 30° angle relative to the vertical. Left: Type A. Middle: Type D. Right: Type E.

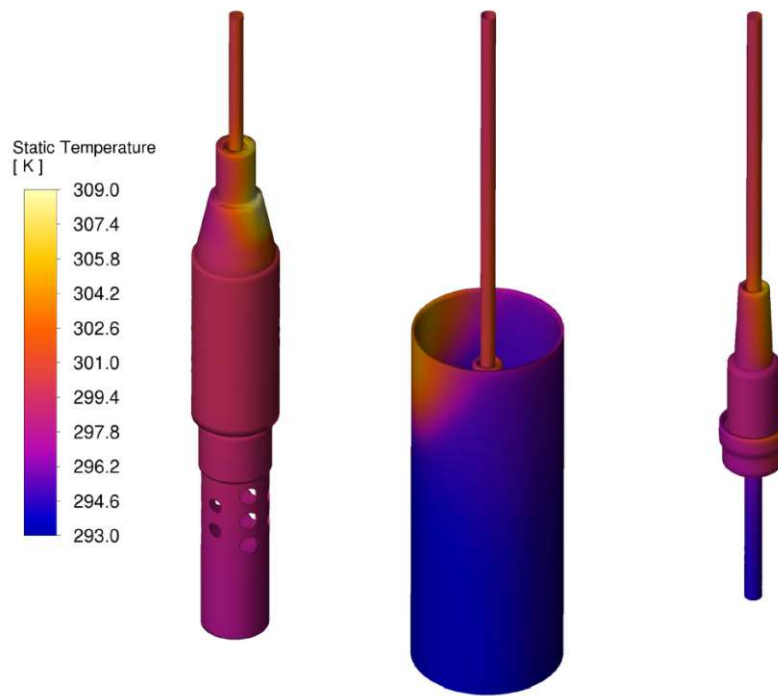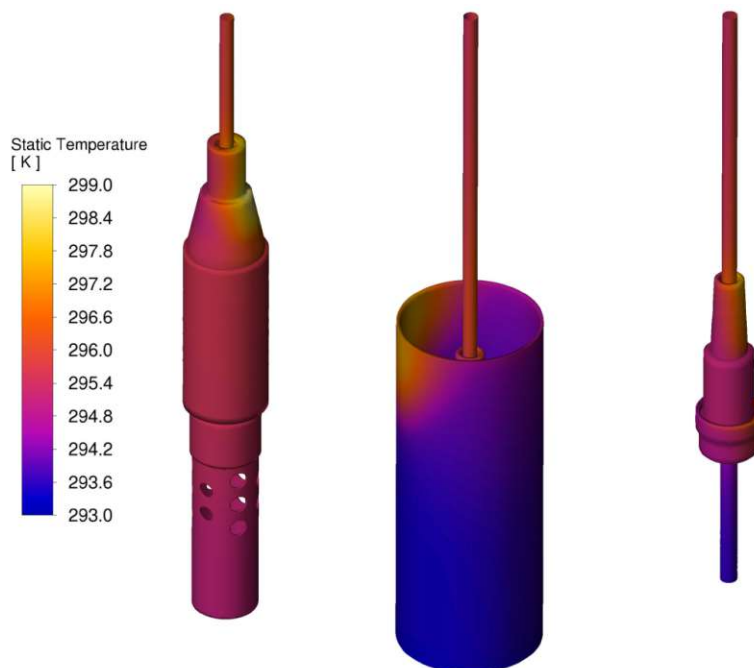Tbl. 5.12 quantifies the performance of each sensor type at both radiation intensities, by comparing the difference of the temperature at the sensor tip with the inlet temperature.

Radiation int. $[W/m^2]$	Type A $[°C]$	Type D $[°C]$	Type E $[°C]$
110	1.88	0.18	0.52
350	4.10	0.32	1.20

Table 5.12.: Summary of the temperature differences between the sensor tip and the inlet air.

The simulations carried out are based on certain assumptions, as outlined in Sec. 5.4.3. Consequently, discrepancies between the simulated sensor tip temperatures and the measured temperatures arise due to these modeling simplifications.

5.4.2. Mean velocity magnitude

Natural convection arises as a result of the elevated temperatures, generating an upward flow that transports thermal energy out of the domain, thus maintaining an energy balance with the incoming radiation (Fig. 5.35 and Fig. 5.36). Sensor type D exhibits the highest velocity magnitude, attributed to the significant temperature gradients within the radiation shield's interior, effectively ensuring a significantly lower temperature at the sensor tip. No qualitative differences are observed between the simulations carried out at $350\,\text{W/m}^2$ and $110\,\text{W/m}^2$. However, the velocity magnitudes are considerably higher in the case of $350\,\text{W/m}^2$.

Figure 5.35.: Comparison of the sensors mean velocity magnitudes at $350\,\text{W/m}^2$. Solar radiation emitted from the top right corner at a 30° angle relative to the vertical. Left: Type A. Middle: Type D. Right: Type E.
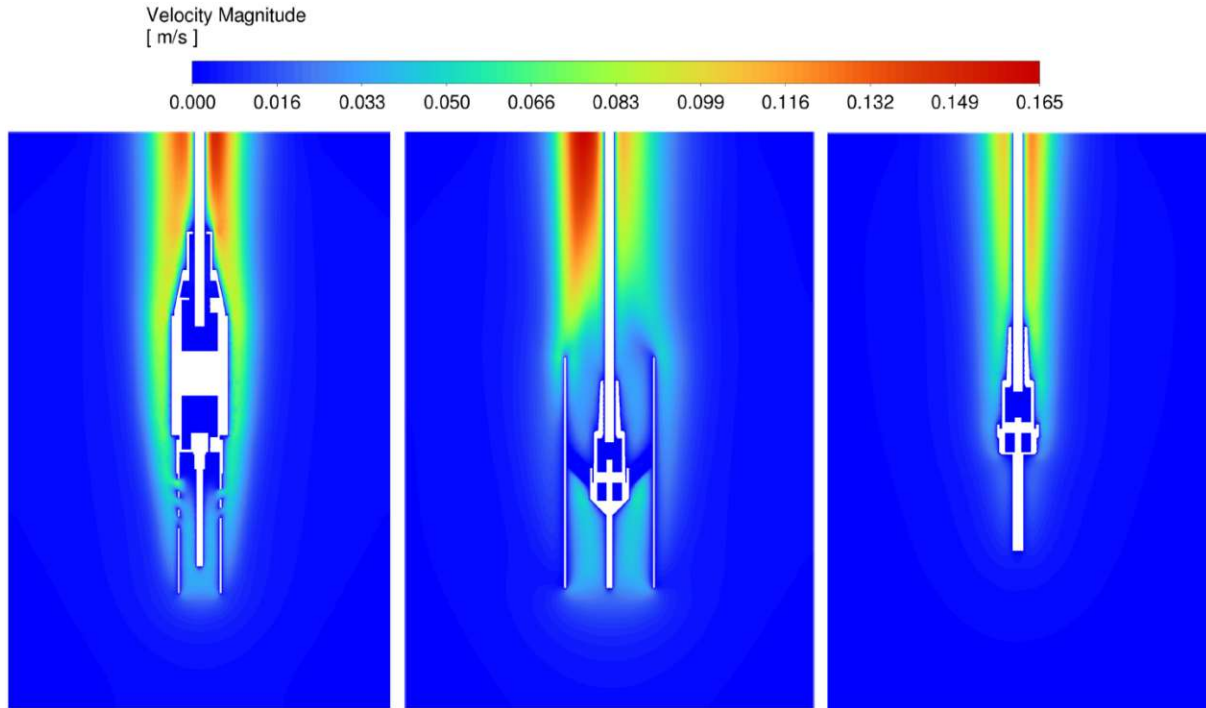

Figure 5.36.: Comparison of the sensors mean velocity magnitudes at $110\,\text{W/m}^2$. Solar radiation emitted from the top right corner at a 30° angle relative to the vertical. Left: Type A. Middle: Type D. Right: Type E.

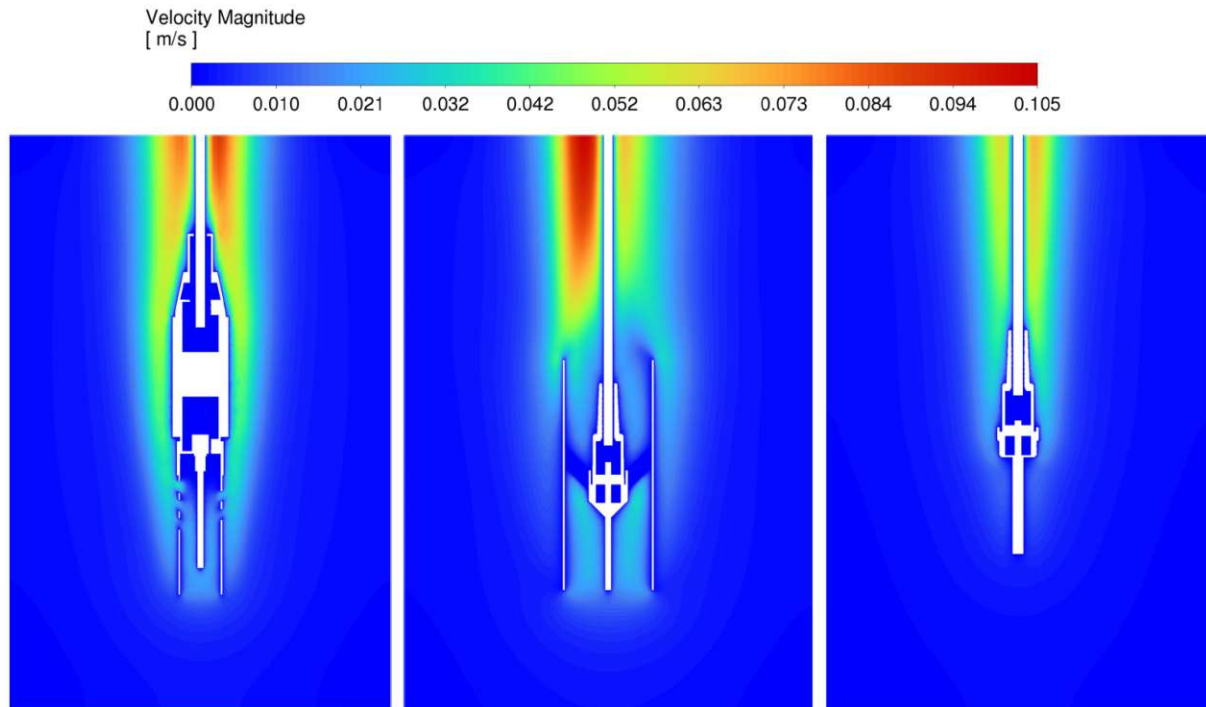### 5.4.3. Modelling errors

Overall, this CFD model provides a good understanding of the underlying physics and delivers qualitative insights. However, several modeling assumptions were made that do not fully capture the actual flow conditions in the test room and railway vehicle, limiting its comparability with them.

The sensor's structural representation lacks the detail of the real-world counterpart. In practice, there are small air gaps between various components that cannot be accurately modeled, having an influence on heat conduction. Additionally, the sensing element is simplified as a single part, whereas in reality, the actual Pt100 element is molded inside the sensing tube with a polymer.

In reality, the surrounding fluid flow is not laminar due to significant temperature gradients within the compartment, leading to natural convection. Moreover, forced convection is present as a result of different air inlets in the compartments.

Material properties were also subject to assumptions during the modeling process.

5.4.4. Comparison of the simulation results

As presented in Tbl. 5.12, sensor type D demonstrates the best performance among the simulated sensor types, followed by type E, with type A exhibiting the poorest performance. Qualitatively, the extensive knurled surface of type A contributes to significant heat conduction to the sensing element. Additionally, the design of the radiation shield traps warm air within, which leads to an undesired heating of the sensing element, despite shielding it from direct radiation. In contrast, type D benefits from its large tubular structure, allowing air to convect freely through the shield without entrapment, resulting in superior performance. Type E, on the other hand, features a radiation shield that is in direct contact with the sensing element with a good balance between performance and a compact design

The developed CFD model proved invaluable during the design phase of new sensor types, enabling virtual prototyping and pre-testing without the immediate need for physical manufacturing.

5.5. Summary and discussion

This chapter highlights the substantial impact of solar radiation on temperature measurements. Among all the sensors tested, type A exhibited the poorest overall performance. The CFD simulations provide a clear explanation: the knurled surfaces of the Tuchel plug, with their high emissivity, absorb a significant amount of radiative heat. Combined with the fully metallic housing and the radiation shield, the absorbed heat is transferred to the lower parts of the sensor configuration. Then the heat is trapped within the radiation shield, unable to escape efficiently due to the tiny holes in the radiation shield. Consequently, a complete redesign of the sensor became necessary, leading to the development

and successful testing of the new sensor with the new radiation shields. A comparison of these designs under various operating conditions and vehicles was performed, with a summary of selected measurement results presented in Tbl. 5.13.

Experiment location	Analysis segment	Radiation int. at sensor $[W/m^2]$	Reference	Temperature difference to type A $[°C]$
Test room	Ventilation	350	Type D	2.56
Test room	Ventilation	110	Type D	0.93
Bus: MP1	Segment 4	≈ 136	Type D	0.92
Test room	Ventilation	350	Type E	2.72
Railway vehicle: MP1	Segment 11	180	Type E	2.11

Table 5.13.: Summary of selected temperature differences relative to type A.

The largest difference, 2.72 °C, was recorded in the test room under radiation of 350 W/m², while the highest difference measured in a vehicle within the Climatic Wind Tunnel was 2.11 °C at 180 W/m², both in comparison to type E. The extended measurement uncertainty of 0.25 °C is significantly smaller [39]. It is noteworthy that inside a tram, radiation intensities of up to 280 W/m² were recorded, suggesting that even larger temperature differences could be expected in these environments.

It is evident that solar radiation has a considerably reduced effect on sensor types D and E. These sensors are more compact and feature reflective housings, in contrast to type A. Its radiation shield is both compact and lightweight. In contrast, type D presents challenges in defining the precise measurement location due to natural convection driven by the large radiation shield. Moreover, type E further minimizes the sensor's impact on the surrounding airflow, as demonstrated in Ch. 8, where the compact design of the temperature sensor significantly reduces its influence on the omnidirectional anemometers employed.

6. Influence of solar radiation on relative humidity sensors

This chapter describes the investigation of the influence of solar radiation on relative humidity measurement. Given the numerous potential setups for determining air humidity (e.g., dew point meters), relative humidity measurement devices are utilized at RTA. These sensors consist of a humidity sensor and a temperature sensor, which together facilitate the measurement of relative humidity. Neither sensor is explicitly shielded against radiation, except from the foam filter. Thus, investigating the impact of solar radiation on these sensors was expected to yield significant findings.

To simplify the analysis and accelerate the acquisition of results, a single sensor type (XD33A) was selected for the development of an effective radiation shield. The findings obtained with this sensor type were subsequently applied to the other two sensor types.

6.1. Experimental setup

The setup for this investigation was the same as for the investigation of the influence of radiation on temperature sensors in the test room. The reference sensor was also positioned in an area without direct radiation from the lamp. The exactly used sensors can be seen in Tbl. 6.1.

Abbreviation	Sensor number	Measurement quantity	Position	Comment
RH_Ref	04-0063	Relative humidity	Reference location	Not radiated
RH01	04-0061	Relative humidity	Position 1	/
RH02	04-0065	Relative humidity	Position 2	/
RH03	04-0055	Relative humidity	Position 3	/
RH04	04-0076	Relative humidity	Position 4	/

Table 6.1.: Sensors for the investigation of the influence of radiation on relative humidity measurement.

Each measurement lasted a total of 70 minutes: the first 60 minutes with the lamp activated, followed by a 10-minute cool-down period. Subsequently, the recording of the measurement was stopped, and a new setup was installed. Sufficient time was allowed between measurements for the sensors to reach equilibrium.

6.2. Different sensor and radiation shield configurations

As described in the following section, radiation has a major influence on the measurement. The previously mentioned bachelor thesis [5] primarily focused on the application of alternative filter caps. Due to the relatively small improvements achieved, it was concluded that further enhancement could only be realized through the development of a dedicated radiation shield. Consequently, various types of radiation shields were developed with varying degrees of success. Fig. 6.1 presents a selection of the tested radiation shields for the XD33A sensor type.

Figure 6.1.: Selection of tested radiation shield configurations for the XD33A sensor type.

6.3. Experimental results

This section initially describes measurements performed without any radiation shield at various radiation intensities for comparative purposes. Subsequently, the applied radiation shields and their performance for the XD33A sensor type are discussed. Finally, all sensors were tested using the optimal radiation shield identified during the investigation with the XD33A sensor.

6.3.1. Measurement without radiation protection

Initial measurements were performed to assess the influence of radiation on the sensors. Radiation intensities of $350\,\mathrm{W/m^2}$ and $110\,\mathrm{W/m^2}$ were selected for this purpose. Fig. 6.2 illustrates the measurements at $350\,\mathrm{W/m^2}$, while Fig. 6.3 depicts those at $110\,\mathrm{W/m^2}$. For comparative purposes, the average differences from the reference sensor over the last 15 minutes before the lamp was turned off were calculated. These differences are represented by the dashed black lines in the right plots of Fig. 6.2 and Fig. 6.3.
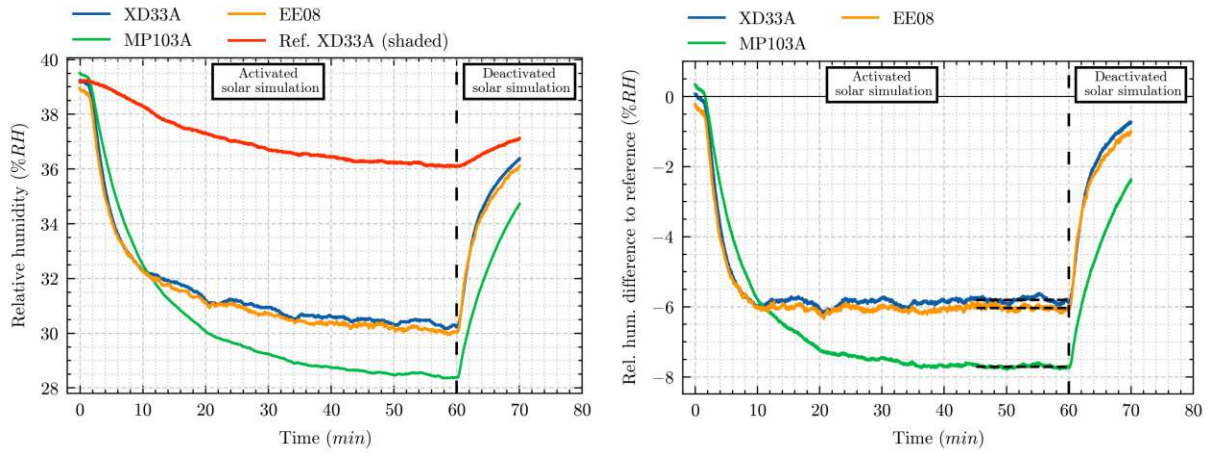
Figure 6.2.: Relative humidity measurement with all sensor types at $350\,\mathrm{W/m^2}$. Left: Absolute values. Right: Differences to reference sensor.
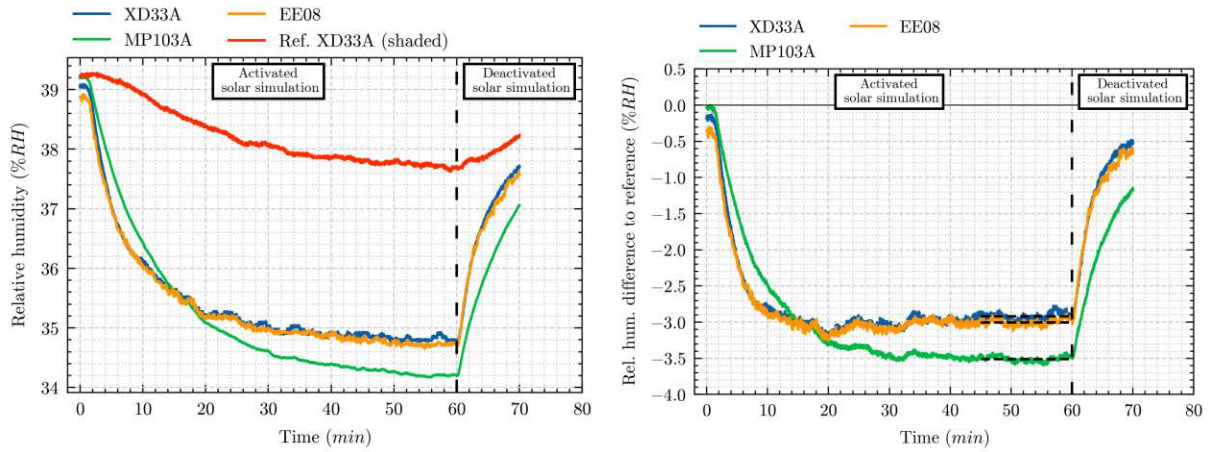

Figure 6.3.: Relative humidity measurement with all sensor types at $110\,\mathrm{W/m^2}$. Left: Absolute values. Right: Differences to reference sensor.

6.3.2. Different radiation protection shields

Various cylinders with aluminum foils and designs with chromium-painted slats, all with different diameters and lengths, were tested, as illustrated in Fig. 6.1. The investigation began with cylinders similar to those tested with the temperature sensors. This design exhibited a significant drawback: after applying the aluminum foil covered cylinder, a sudden decrease in relative humidity was observed, without even any solar radiation present. Although increasing the diameter reduced this decrease, it could not be entirely eliminated. For example, the second cylinder from the left in Fig. 6.1 exhibited a decrease of approximately $2\,\%\,\mathrm{RH}$ after applying it. Such a variation is unacceptable, leading to the development of the slat design. The decrease with the slat design was negligible, of $0.1\,\%\,\mathrm{RH}$. After several design iterations and measurements, the final design was established. Further increasing the number of slats to protect the entire sensor or implementing

a hybrid design consisting of a cylinder and slats near the sensors did not yield additional improvements. The measurements also indicated that the sprayed chromium coating on the 3D printed parts is crucial. An alternative coating with an even lower emissivity coefficient might further enhance the design.

6.3.3. Measurement with radiation protection

The final radiation protection design for the XD33A sensor was subsequently applied to the other sensor types. The inner diameter of the slats for the shields of the MP103A and EE08 sensors was selected to ensure that the distance from the sensor to the inner diameter of the slat is consistent across all sensor types. Fig. 6.4 presents the final results at a radiation intensity of $110\,\mathrm{W/m^2}$.
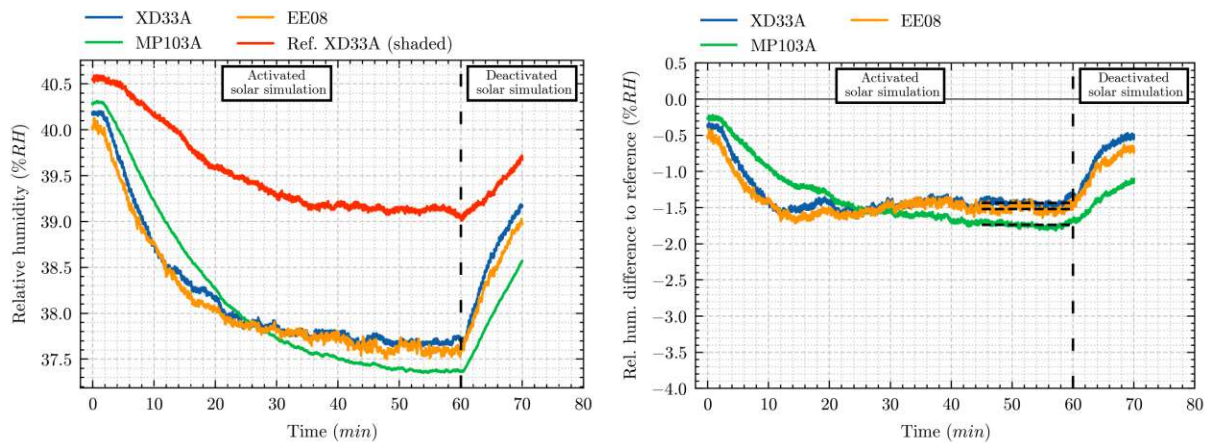

Figure 6.4.: Relative humidity measurement with all sensor types and radiation protection at $110\,\mathrm{W/m^2}$. Left: Absolute values. Right: Differences to reference sensor.

6.4. Summary and discussion

Tbl. 6.2 summarizes the results. It is evident that the differences of the sensors without a radiation shield to the reference sensor are significant. At $350\,\mathrm{W/m^2}$, the discrepancies are twice as large as those observed at $110\,\mathrm{W/m^2}$. The developed radiation protection shield significantly reduces these differences for all sensor types, demonstrating its effectiveness for the XD33A sensor as well as for the other two sensor types.

The extended measurement uncertainty, a key value for measurements, is $2\,\%\,\mathrm{RH}$ at a temperature of $40\,^{\circ}\mathrm{C}$ and a relative humidity of $80\,\%\,\mathrm{RH}$ and indicates the accuracy of the relative humidity measurement [39].

Sensor type	No radiation shield at 350 W/m² [% RH]	No radiation shield at 110 W/m² [% RH]	Radiation shield with slats at 110 W/m² [% RH]
XD33A	5.8	2.9	1.1
MP103A	7.7	3.5	1.2
EE08	6.0	3.0	1.1

Table 6.2.: Summary of the relative humidity differences of all sensor types with and without the developed radiation shields.

The residual difference between the sensors with radiation protection and the reference measurement is smaller than the extended measurement uncertainty but remains present. One possible explanation for this discrepancy is the incomplete uniform distribution of humidity within the test room, despite the ventilation being activated. Additionally, the irradiated area heats up, and the heated air may not have been sufficiently distributed within the test room to reach the reference sensor either. An indicator of this could be the persistent difference of about $1\,\%\,\mathrm{RH}$ of all sensor types compared to the reference sensor at the end of the measurement when the lamp has been turned off for ten minutes.

There is no doubt that radiation influences the measurement of relative humidity. However, no comparative validation measurements were performed in the wind tunnel due to a lack of the availability of a suitable vehicle at the right time. A key factor whether radiation plays a role or not is the positioning of the relative humidity sensors within the vehicles. As shown in Tbl. 5.3, the long-distance transportation vehicle tested had a radiation intensity of only $5\,\mathrm{W/m^2}$ at the location where the relative humidity measurement is performed (center of the aisle at a height of $1.7\,\mathrm{m}$ near the entrance). This minimal intensity has a negligible effect on the relative humidity measurement. In contrast, a local transportation vehicle exhibited a radiation intensity of $100\,\mathrm{W/m^2}$ in the center of the aisle at a height of $1.1\,\mathrm{m}$, where the relative humidity measurement is performed in this type of vehicle.

Considering these factors, it becomes apparent that depending on the vehicle type and window configuration, the use of the developed radiation shields will be necessary to mitigate the influence of radiation. Furthermore, in vehicles where feasible, positioning the relative humidity sensors in locations not directly exposed to radiation (e.g., in gangways) also appears to be a practical option.

7. Influence of solar radiation on CO$_2$ sensors

This chapter analyzes the effects of solar radiation on the Vaisala GMP252 CO$_2$ sensors utilized at RTA. Although these sensors are equipped with temperature compensation, the precise location of the temperature compensation sensor within the sensor and whether all components of the sensor experience uniform temperature conditions were not clearly understood. Consequently, it was deemed necessary to investigate this influence through an experimental analysis.

7.1. Experimental setup

The experimental setup was analogous to the previous investigation of the influence of solar radiation on temperature sensors in the test room. A reference sensor was positioned in a shaded area, while two additional sensors were placed within the radiation field. The specific sensors employed in the experiment are detailed in Tbl. 7.1.

Abbreviation	Sensor number	Measurement quantity	Position	Comment
CO2_Ref	17-0046	CO2 concentration	reference location	not radiated
CO2_01	17-0047	CO2 concentration	position 1	/
CO2_02	17-0045	CO2 concentration	position 2	/

Table 7.1.: Sensors for the investigation of the influence of radiation on CO$_2$ concentration.

7.2. Experimental results and discussion

Measurements were performed to assess the impact of radiation on this type of sensor. As shown in Fig. 7.1, the differences between the radiated sensors and the reference sensor are below 30 ppm throughout the measurement. This deviation is significantly smaller than the sensor's extended measurement accuracy, which is specified as ±126 ppm in the measurement range from 500 ppm to 2000 ppm [39]. Consequently, an influence of radiation is disproved and no further measurements were deemed necessary.
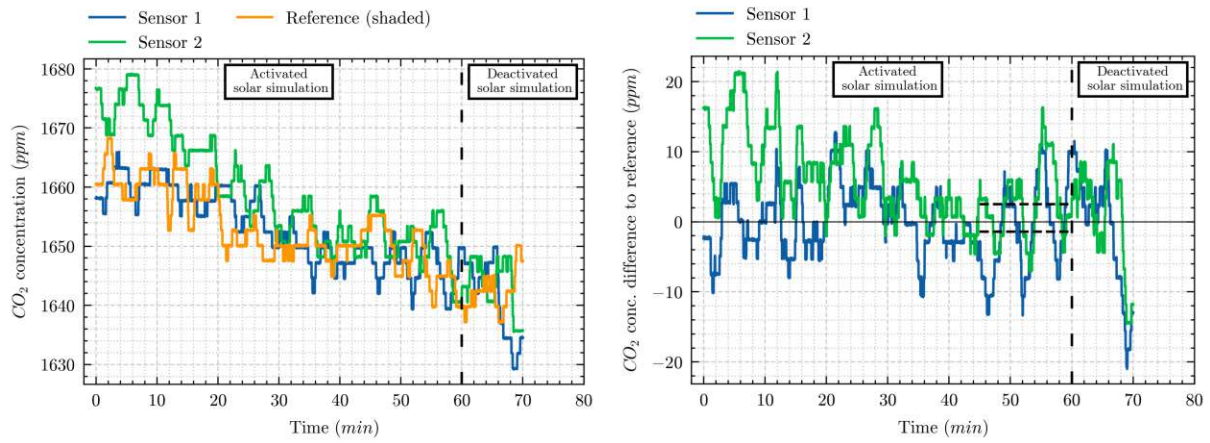
Figure 7.1.: CO_2 concentration measurement with two identical sensors and one shaded reference sensor at $350\,\mathrm{W/m^2}$. Left: Absolute values. Right: Differences to reference sensor.

8. Influence of objects near omnidirectional anemometers

During measurements in rail vehicles, numerous sensors are placed within the driver's cab and passenger compartments. Particularly at the driver's seat temperature sensors, relative humidity sensors, and CO_2 sensors are positioned in close proximity to anemometers. Inside rail vehicles typically no dominant airflow direction is present, consequently nearby sensors can affect the anemometer readings. This Chapter investigates the potential impact of such objects on anemometer measurements through a series of simple experiments.

8.1. Sensor positioning

The positioning of anemometers, like other sensor types, typically follows a standard, as EN 13129 [3] and EN 14813 [23]. However, these standards do not specify the physical dimensions of the sensors. Fig. 8.1 depicts an experimental setup in a long-distance passenger compartment and the driver's cab of a railway vehicle.

Figure 8.1.: Measurement setup in a long-distance railway vehicle. The anemometer probes are not fully extended to avoid potential damage. Left: Driver's cab. Right: Passenger compartment.

The proximity of various sensors to the anemometers could significantly influence the airflow measurements. These setups demonstrate the potential for interference and highlight the need for further investigation.

8.2. Theoretical considerations

As discussed in Sec. 2.3, the dimensionless Reynolds number (Re) is a key parameter for characterizing the flow conditions in this experimental setup. In railway vehicles, air velocities typically range from $0\,\mathrm{m/s}$ to $1\,\mathrm{m/s}$, leading with Eq. 2.6 to a range of Re numbers with several orders of magnitude, as outlined in Tbl. 8.1.

Parameter	Abbreviation	Value
Air speed range[1]	v	$0.05 - 1\,\mathrm{m/s}$
Characteristic length	L	$0.0275\,\mathrm{m}$
Temperature	T	$20 - 30\,^{\circ}\mathrm{C}$
Kinematic viscosity	ν	$1.516 \times 10^{-5} - 1.608 \times 10^{-5}\,\mathrm{m^2/s}$
Reynolds number	Re	$86 - 1814$

[1] The lower limit is the lower measuring range limit of the anemometer.

Table 8.1.: Parameters used to calculate the Reynolds number range.

The diameter of a standard Pt100 resistance thermometer is selected as the characteristic length scale. The distinct wake behaviors are illustrated in Fig. 2.2. The flow regimes

relevant to rail vehicles include a laminar vortex street, the transition to a turbulent wake, and a turbulent wake with a laminar boundary layer separation.

To sum up, the literature review indicates that a circular object generates a significant wake, which can impact air speed measurements. When the measurement is taken directly along the centerline downstream of the cylinder, the resulting airspeed will experience the greatest deviation. This scenario will, therefore, be further examined experimentally. The complexity of the interaction between natural and forced convection of the hot sphere anemometer, combined with the turbulence-induced wake of the cylinder, makes it impractical to model using CFD methods within a reasonable timeframe. As a result, no CFD model has been developed.

8.3. Experimental setup

A temperature sensor is positioned upstream of the hot sphere anemometer. This placement is standard practice, as temperature sensors are commonly located near anemometers, as can be seen in Fig. 8.1. To generate constant airflow, an axial fan with a diameter of 0.25 m is employed, and its speed is regulated using a direct current controller. To assess the influence of angular dependency, the fan can be rotated while ensuring its centerline remains aligned with the hot sphere anemometer. The entire setup is positioned near the floor to minimize natural convective flow. The experiments are carried out in a large, non-ventilated room without windows and with closed doors, measuring approximately 10 meters in length and 8 meters in width, to maintain stable environmental conditions throughout the experiments. Additional dimensions of the test setup are provided in Tbl. 8.2, and an illustration of the experimental setup is shown in Fig. 8.2.
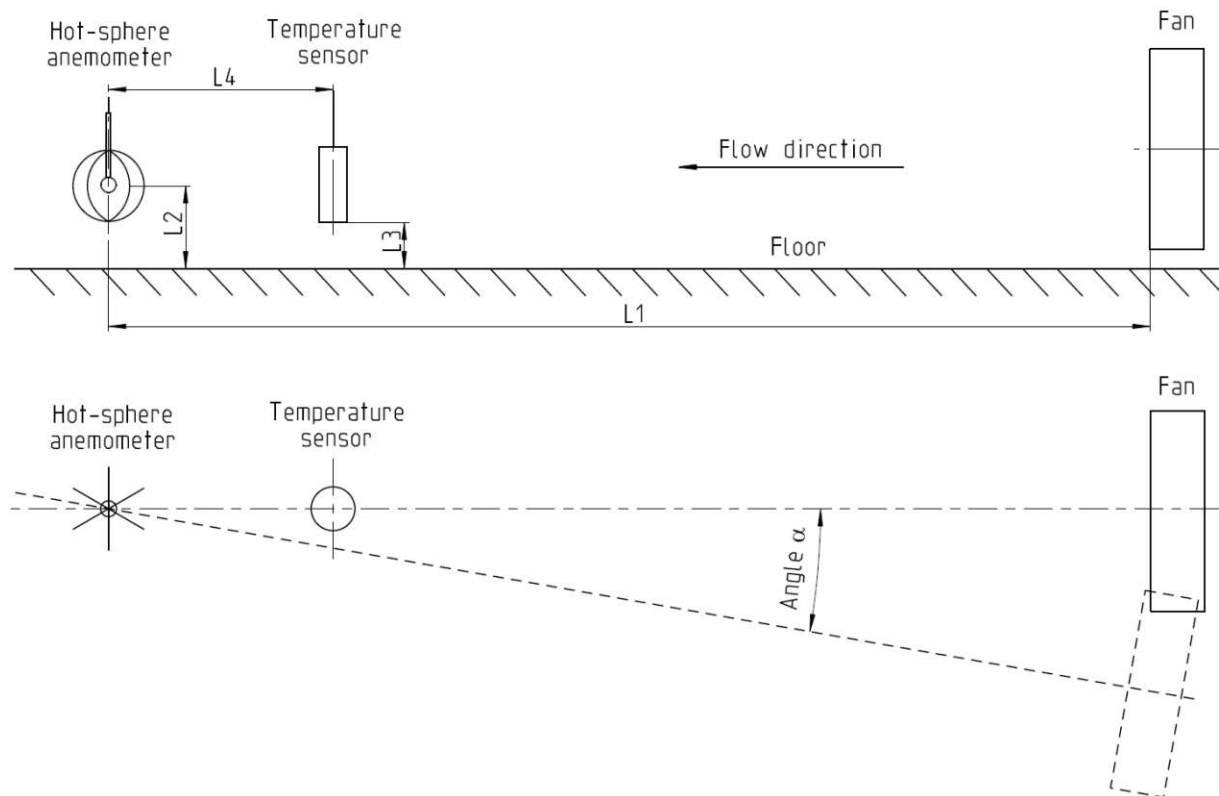
Figure 8.2.: Schematic of the experimental setup with the temperature sensor positioned upstream of the hot sphere anemometer.

Dimension	Value
L1	4 700 mm
L2	125 mm
L3	Old sensor: 75 mm New sensor: 85 mm
L4	Depending on measurement
α	Depending on measurement

Table 8.2.: Dimensions of the test setup.

The experimental procedure consists of an initial reference measurement at a predetermined flow velocity, performed without the temperature sensor, followed by a series of measurements where the temperature sensor's position relative to the anemometer is varied. Then a concluding reference measurement without a temperature sensor in front is performed. This methodology was necessary due to the impracticality of replicating two identical test setups and conducting simultaneous measurements. The flow behaviour is assumed to remain constant throughout the measurement series. To verify this assumption, the mean velocities of the initial and final reference measurements are permitted to deviate by a maximum of 0.02 m/s. Otherwise, the series is classified as invalid. The reference velocity for the measurement series is defined as the mean of these two values.

To mitigate minor disturbances, each measurement is performed for a duration of 10 minutes, with a minimum five minute stabilisation period after each parameter adjustment to ensure a steady state is achieved.

8.4. Experimental results and discussion

This section presents and discusses the experimental results obtained during the study. Relevant insights and trends observed during the experiments are highlighted, and potential sources of error are considered in the discussion.

8.4.1. Measured velocities without an activated fan

To confirm that the test room was suitable for the measurement series, an initial measurement was carried out without activating the fan. The results, shown in Fig. 8.3, indicate a mean airspeed of $0.058\,\mathrm{m/s}$, which is near the lower limit of the device's measurement range. Consequently, the subsequent measurements are not expected to be influenced by any other external factor.
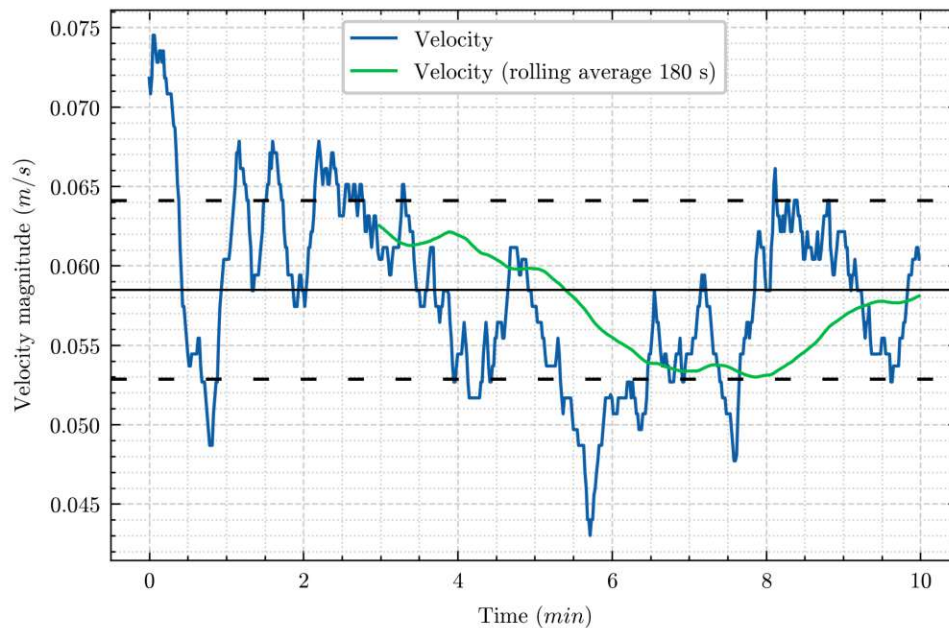
Figure 8.3.: Measurement of the flow velocity without fan. The mean velocity was $0.058\,\mathrm{m/s}$ and the standard deviation was $0.006\,\mathrm{m/s}$.

8.4.2. Influence of the distance between the temperature sensor and the anemometer

Measurements were performed at various flow velocities and at different distances between the temperature sensor and the anemometer. Fig. 8.4 illustrates the differences from the reference measurements.
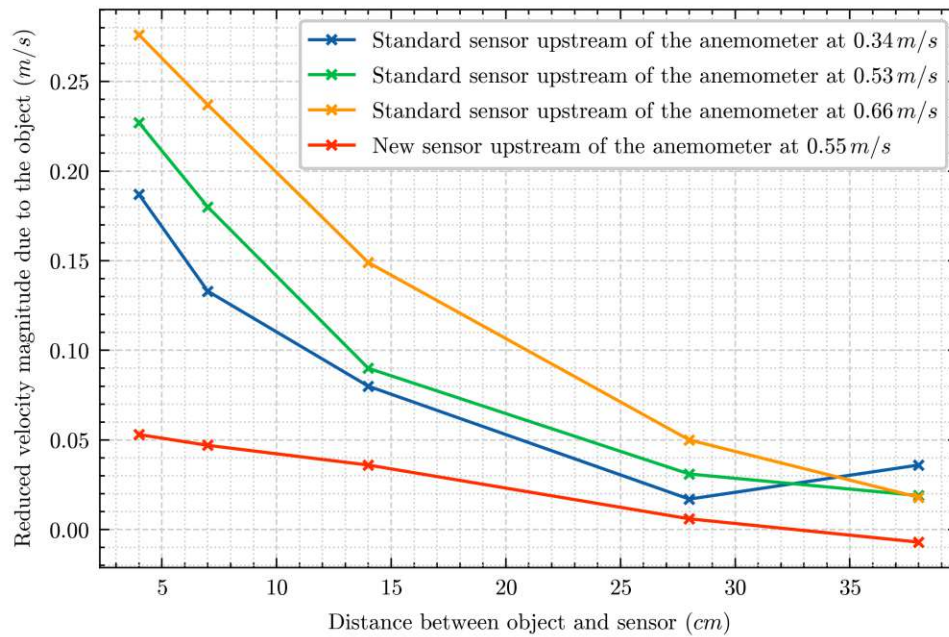
Figure 8.4.: Difference to reference measurements as a function of distance between the temperature sensor and the anemometer at different flow speeds. At smaller distances, the errors are significant but decrease as the distance between the objects increases.

The discrepancies from the reference measurements are more pronounced at shorter distances between the anemometer and the temperature sensor, decreasing to less than $0.05\,\text{m/s}$ at a distance of 38 cm. The error increases with higher flow velocities regardless of distance, with the exception of the velocity magnitude at 38 cm and $0.35\,\text{m/s}$. This anomaly is likely attributable to a small disturbance during this measurement period.

Notably, the newly developed sensor, as described detailed in Sec. 5.1.2, exhibits a significantly lower impact on the velocity measurement, despite being evaluated at a reference speed of $0.5\,\text{m/s}$. The data point for the new sensor at a 38 cm distance falls below zero, which is indicative for a minor random measurement error.

8.4.3. Influence of the angle between the temperature sensor and the anemometer

Measurements were carried out with varying angles between the incoming airflow and the imaginary line connecting the temperature sensor and the anemometer. To simplify the analysis, all measurements were performed with a fixed distance of 10 cm between the temperature sensor and the anemometer, and a flow velocity of about $0.55\,\text{m/s}$ in the absence of any object to ensure comparability with the previously mentioned measurements. The results are shown in Fig. 8.5.
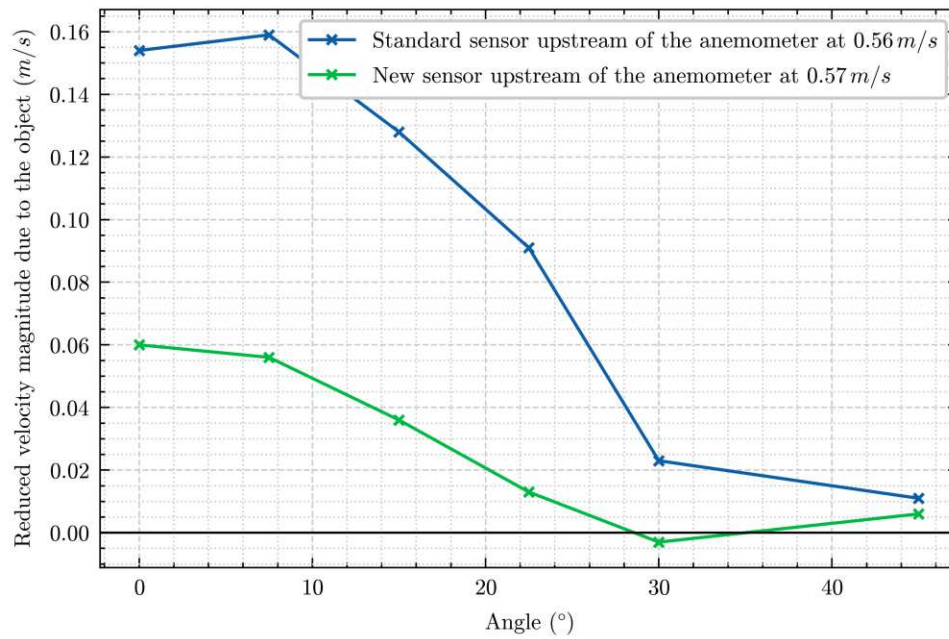
Figure 8.5.: Difference to reference measurements as a function of the angle between the flow direction and the line of the two objects at similar flow speeds and a constant distance of 10 cm between the temperature sensor and the anemometer.

The two measurement series exhibit similar trends, although with differing magnitudes. The larger, standard sensor causes a reduction in the measured flow velocity more than twice that of the new, smaller temperature sensor. At an angle of 22.5°, the new sensor causes a negligible reduction in flow velocity, approximately 0.01 m/s, whereas the standard sensor decreases the flow velocity by approximately 0.09 m/s. This confirms that smaller objects cause less disturbance to the flow. The slight negative value observed for the new sensor at 30° can be attributed to a minor measurement uncertainty.

9. Influence of different temperatures on omnidirectional anemometers

This chapter aims to analyze the influence of temperature on omnidirectional anemometers.

Both omnidirectional anemometers used at RTA, the reference anemometer SWEMA03 and the TSI anemometer, are equipped with internal temperature compensation. As a result, the measured values should theoretically remain unaffected by temperature variations. However, the accuracy of the temperature compensation is unknown and has never been analyzed.

9.1. Anemometer calibration process of RTA

At RTA, a small scale flow channel is utilized for the calibration of the omnidirectional anemometer. The calibration process follows a systematic approach: First, the flow channel itself is calibrated at various flow velocities using a highly accurate reference sensor (SWEMA03), which has been calibrated by an external laboratory. Next, the anemometer undergoing calibration is exposed to the same flow velocities as the reference sensor. A pulse-width modulation (PWM) signal is applied to the fan motor to ensure stable and repeatable flow velocities. Finally, the collected data is evaluated, and new calibration coefficients are computed.

To minimize errors arising from incorrect vertical positioning, as identified in the previous bachelor's thesis [5], a new laser alignment system has been implemented. The sensor's radial position is precisely determined by a 3D-printed attachment. The sensor's axial (vertical) position is ensured by the laser which projects a cross onto the sphere of the sensor and the rear wall of the channel. The shadow of the sphere indicates the current position. Fig. 9.1 illustrates the flow channel setup and the calibration process at RTA.
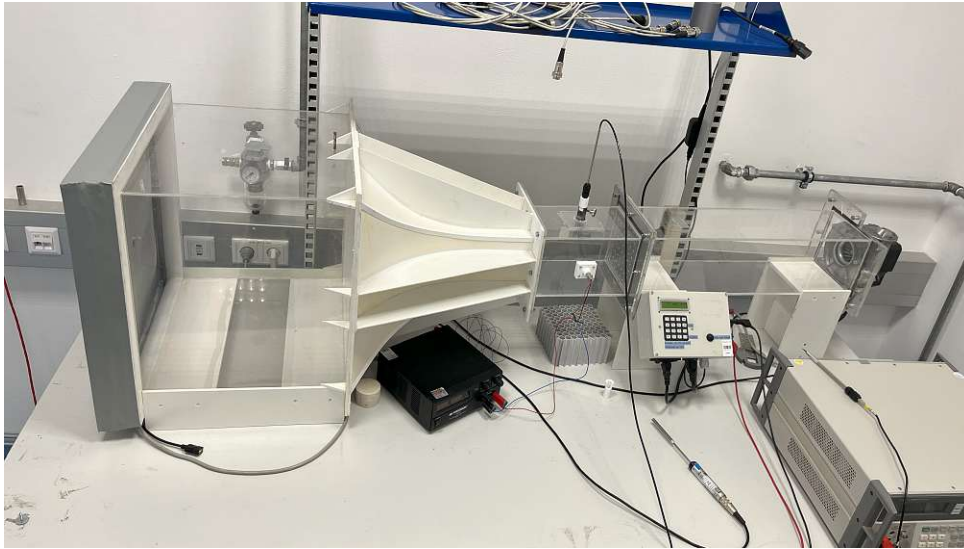
Figure 9.1.: Used flow channel for calibrating the anemometers. The radial fan at the outlet sucks the air from the left. At the inlet a perforated sheet metal and a insect mesh reduce large scale turbulence.

9.2. Experimental setup

The flow channel used for calibrating the anemometer was also employed for analyzing the temperature dependence of anemometers. The channel has two small holes on the top wall to insert temperature sensors. One sensor is located upstream, prior to the contraction of the channel, while the other is positioned downstream of the anemometer, after the perforated sheet metal. Additionally, a temperature sensor was placed 40 cm upstream of the flow channels inlet, and another one was positioned in the center of the room at a slightly higher height than the others. All temperature sensors used were newly designed sensors as detailed in Sec. 5.1.2.

The entire experimental setup was situated in a test room measuring approximately 5 meters in length and 3 meters in width, equipped with an air conditioning system. To elevate the room temperature, three 3 kW electric resistors were used. Due to the absence of an automated temperature control system during heating, temperature regulation was manually maintained by selectively connecting and disconnecting the resistors. To minimize the impact of radiation and ensure a more uniform temperature distribution throughout the room, the resistors were positioned behind a large climate cabinet on the opposite side of the room. Fig. 9.2 provides a schematic overview of the room setup.
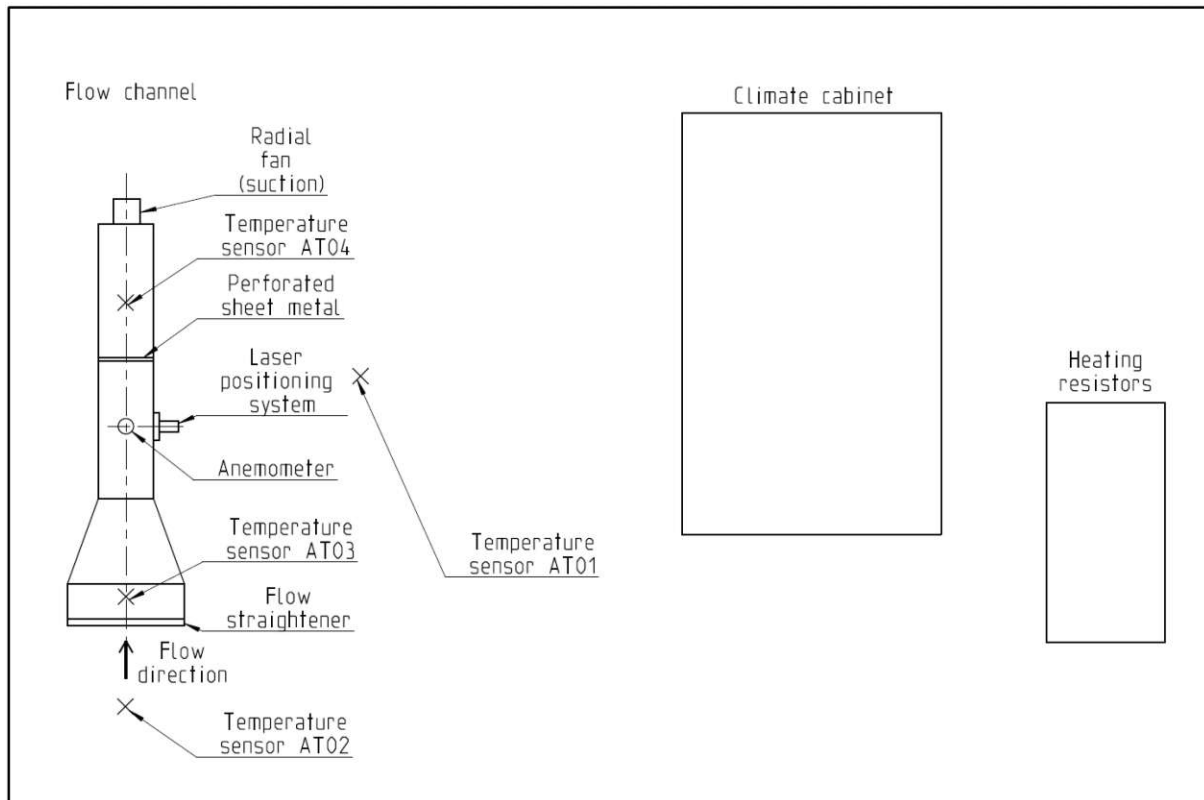
Figure 9.2.: Schematic overview of the test room setup for the investigation of the temperature influence on omnidirectional anemometer.

Tbl. 9.1 provides a summary of the sensors used in this experiment, including their respective positions and specifications.

Abbreviation	Sensor number	Measurement quantity	Position	Comment
AT01	LT08	Temperature	Middle of the room	New built
AT02	LT14	Temperature	Upstream anemometer, outside channel	New built
AT03	LT16	Temperature	Upstream anemometer, inside channel	New built
AT04	LT15	Temperature	Downstream anemometer, inside channel	New built
VEL01	03-0100	Velocity	Flow channel	SWEMA03
VEL02	/	Velocity	Flow channel	TSI new
VEL03	03-0091	Velocity	Flow channel	TSI old

Table 9.1.: Sensors for the investigation of the temperature influence on omnidirectional anemometers.

Sensor VEL02 has not yet been assigned an RTA sensor identification number, as it is a newly acquired one. Consequently, the most recent calibration of this sensor was carried out at the manufacturer's facility, which was still valid at the time the measurements were performed.

To investigate the behavior of the anemometers at different velocities, five distinct speeds were selected, ranging from approximately 0.1 m/s to approximately 0.8 m/s. Each velocity was maintained for a duration of four minutes. The initial minute at each velocity was allocated to achieve a steady state, while the remaining three minutes were utilized to get an average velocity. The sampling frequency was set to 1 Hz.

9.3. Experimental results and discussion

In general, all temperature sensors distributed throughout the room exhibited minimal deviations from one another. The sensor located at the center of the room (AT01) was the most influenced by the heat generated from the resistors and exhibited the shortest response time to changes in the number of active resistors. Temperature sensor AT03, positioned upstream the contraction and therefore at a slightly higher elevation, recorded marginally higher temperatures due to the vertical temperature gradient in the room. Consequently, the temperature sensor positioned downstream of the anemometer (AT04) proved to be the most suitable reference sensor, as it measured the temperature closest to the anemometer. Moreover, it showed the best correlation with the temperature sensor of the reference anemometer. Thus, sensor AT04 is designated as the reference temperature sensor throughout this chapter.

The following figure shows the reference measurement of the SWEMA03 sensor at about 21.7 °C.
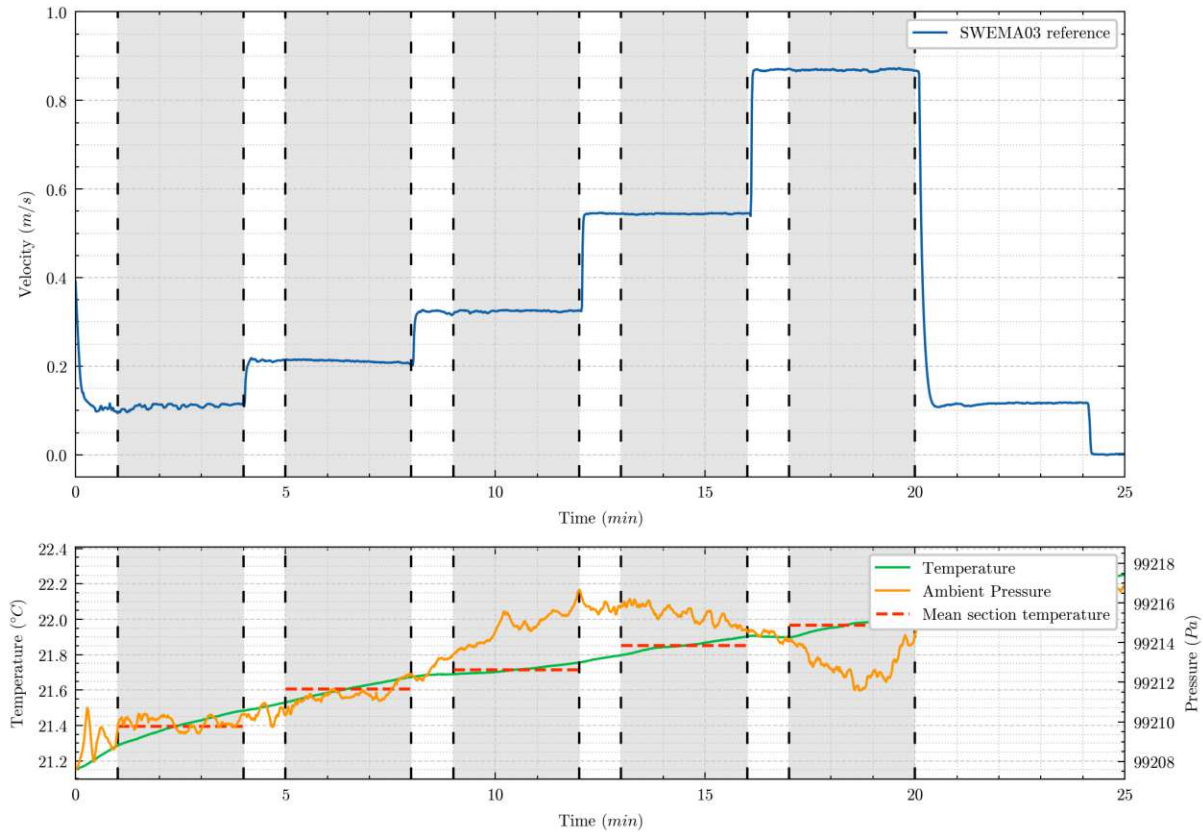
Figure 9.3.: Reference measurement of the SWEMA03 sensor at about 21.7 °C.

The plot clearly illustrates the different velocity steps and the corresponding time required to achieve a steady state. Each grey-shaded region represents a measurement interval for a specific data point (e.g., as shown in Fig. 9.4). Due to minor fluctuations in both temperature and velocity during the measurement, the mean values of temperature and velocity are calculated for each region. The ambient pressure is included for informational purposes. The not shaded region at the end is used for comparative analysis and is not further considered in the evaluation.

Additionally, this dataset serves as the reference measurement for all subsequent figures in this chapter. All computed differences are compared to this reference measurement.

9.3.1. Influence of temperature on the reference anemometer (SWEMA03)

Fig. 9.4 illustrates the measurement deviations observed at various flow velocities and temperatures.

87
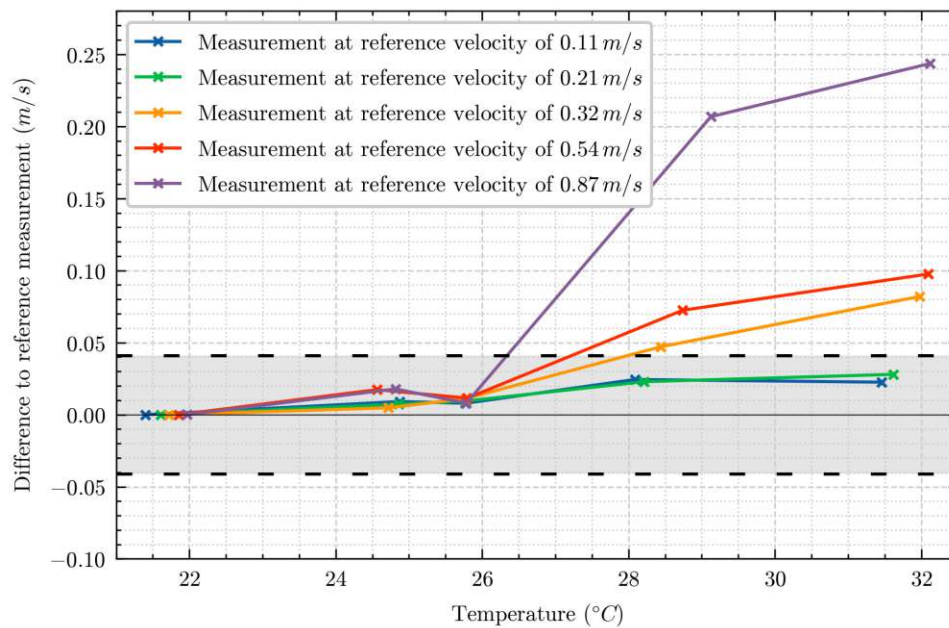
Figure 9.4.: Influence of temperature variations at specific flow velocities of the reference anemometer (SWEMA03) compared to the reference measurement (SWEMA03). The grey-shaded region indicates the range of the extended measurement uncertainty.

It is evident that the deviations remain negligible up to approximately $26\,°C$. However, at around $28.5\,°C$, the discrepancies increase, particularly at the highest flow velocity of $0.87\,\text{m/s}$. At about $32\,°C$, the deviations persist, reaching a maximum difference of $0.24\,\text{m/s}$ at a flow velocity of $0.87\,\text{m/s}$. The differences of the lower flow velocities of $0.11\,\text{m/s}$ and $0.21\,\text{m/s}$ stayed within the bounds of the extended measurement uncertainty for the whole investigated temperature range.

This demonstrates that calibration with this sensor should be performed at temperatures below $26\,°C$, as higher temperatures can result in significant errors when using this sensor as a reference for the calibration of other devices.

9.3.2. Influence of temperature on an old TSI anemometer

To investigate the effectiveness of the temperature compensation, an older TSI anemometer, in operation since 2012, was tested. This particular sensor has not undergone any refurbishment by the manufacturer, and as a result, the accuracy of its temperature compensation had not been previously assessed. The calibration coefficients used in this measurement were determined through the calibration procedure outlined in Sec. 9.1.
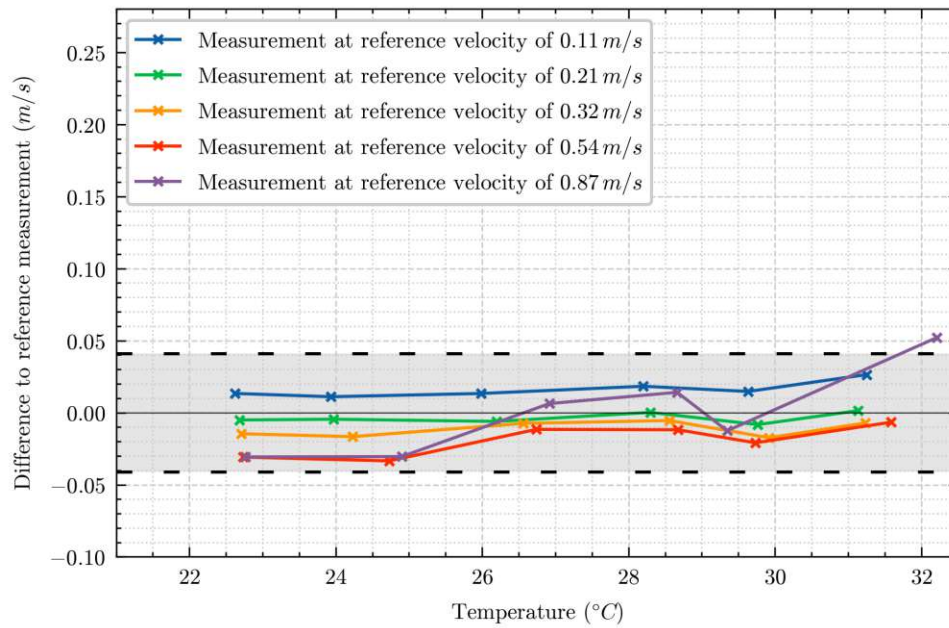
Figure 9.5.: Influence of different temperatures at certain flow velocities of an old TSI anemometer to the reference measurement (SWEMA03). The grey-shaded region indicates the area of the extended measurement uncertainty.

With the exception of a single measurement point, interpreted as an outlier, all differences relative to the reference measurement are within the extended measurement uncertainty. This result proves that the temperature compensation of the sensor remains effective.

9.3.3. Influence of temperature on a new TSI anemometer.

The following figure presents the results for a newly manufactured anemometer without the application of RTA's calibration coefficients.
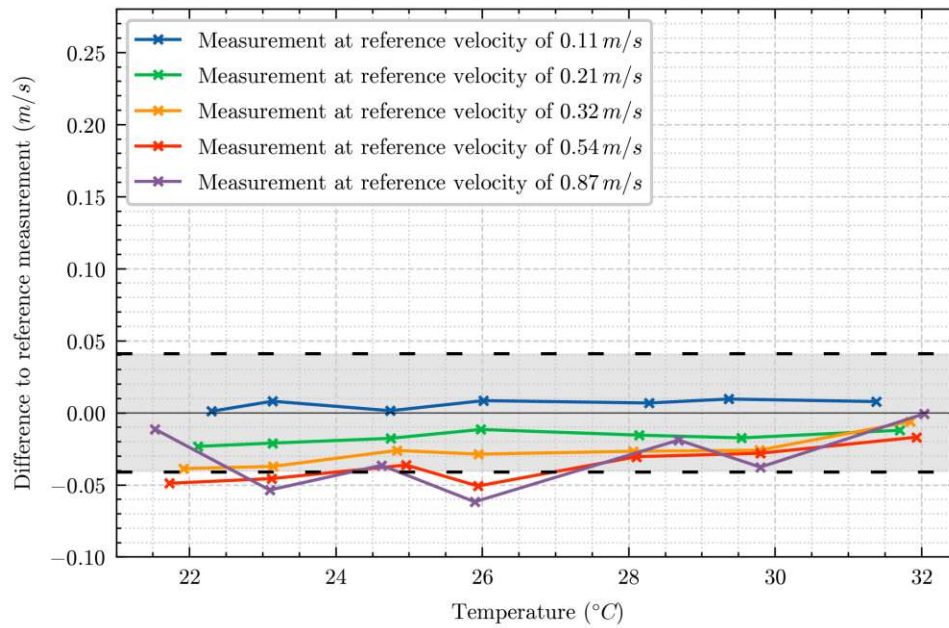
Figure 9.6.: Influence of temperature variations at specific flow velocities a new TSI anemometer compared to the reference measurement (SWEMA03). The grey-shaded region indicates the range of the extended measurement uncertainty.

At the lowest flow velocities, the differences remain relatively constant. However, for higher velocities, more pronounced negative deviations are observed, with the maximum difference reaching $-0.062\,\mathrm{m/s}$. These larger deviations, compared to previous measurements, may be attributed to variations in the calibration procedures and the equipment compared to the manufacturer.

10. Conclusions and future work

Several measurement effects were analyzed in this thesis, with particular emphasis on solar radiation and its impact. The primary focus was on the room temperature sensors and their optimization. Both the experimental work and the developed numerical CFD model demonstrated that solar radiation has a substantial influence on temperature measurement. However, this impact can be significantly reduced with the implementation of the newly developed sensor types.

Relative humidity measurements were also found to be affected by solar radiation. This impact can be minimized using the designed radiation shields and/or through strategic positioning of sensors in non-radiated areas within vehicles.

In contrast, the investigation of the influence of solar radiation on CO_2 sensors revealed no measurable impact, indicating the robustness of these sensors against radiative effects.

The extensive measurement equipment deployed in the limited installation place affects each other. The analysis of omnidirectional anemometers positioned near temperature sensors indicated a notable influence of nearby temperature sensors on anemometer readings. However, the newly developed temperature sensor demonstrated a substantially reduced impact on the anemometer data.

Additionally, the study on the effect of varying temperature levels on anemometer readings revealed that the TSI sensors employed in the Climatic Wind Tunnel are unaffected by temperature fluctuations. In contrast, the SWEMA03 anemometer, used for calibration, is temperature sensitive at temperatures above $26\,°\mathrm{C}$. Consequently, it is recommended that the calibration procedure is performed under consistent temperature conditions to ensure measurement accuracy.

Recommendations for future research:
The following topics may be the subject of future work:

- **Impact of solar radiation on omnidirectional anemometers:** Although these devices are temperature-compensated, the integrated temperature sensor is missing a radiation shield and therefore may overcompensate the measurement signal. A preliminary experiment applying a 3D-printed radiation shield yielded substantial differences even in the absence of radiation requiring a deeper analysis.

- **Effects of solar radiation on channel temperature sensors:** While these sensors are typically positioned within airflow ducts, partial exposure to direct radiation can occur. It is recommended to assess the extent to which this affects their accuracy and explore design improvements or shielding solutions.

- **Performance of surface temperature sensors under solar radiation:** These sensors are commonly applied to windows and walls exposed to solar radiation. An investigation should be performed to analyze the impact of the mounting tape and the properties of the underlying material on the sensor readings.

A. Appendix

A.1. Additional validation results from the bus

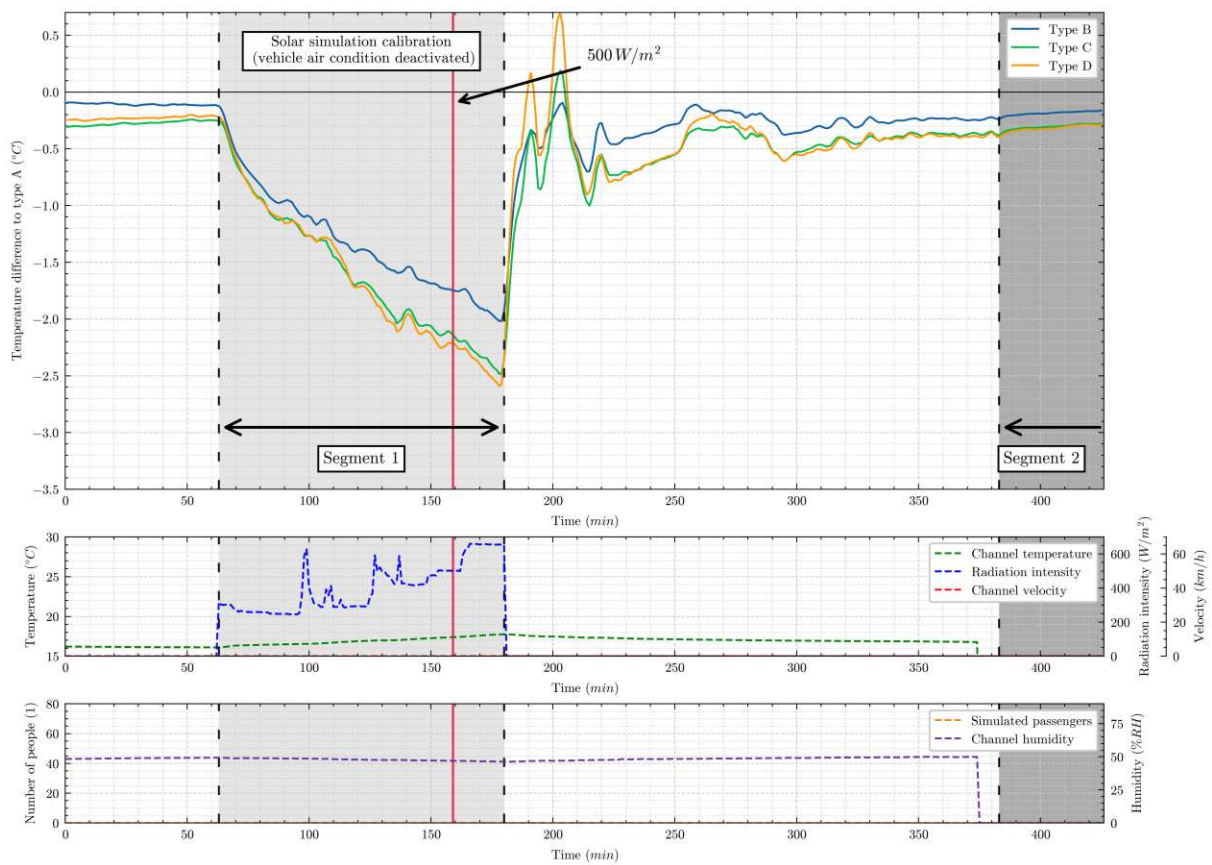### A.1.1. Temperature differences of measurement place 2

Figure A.1.: Temperature differences relative to the sensor type A when the bus ventilation was deactivated.
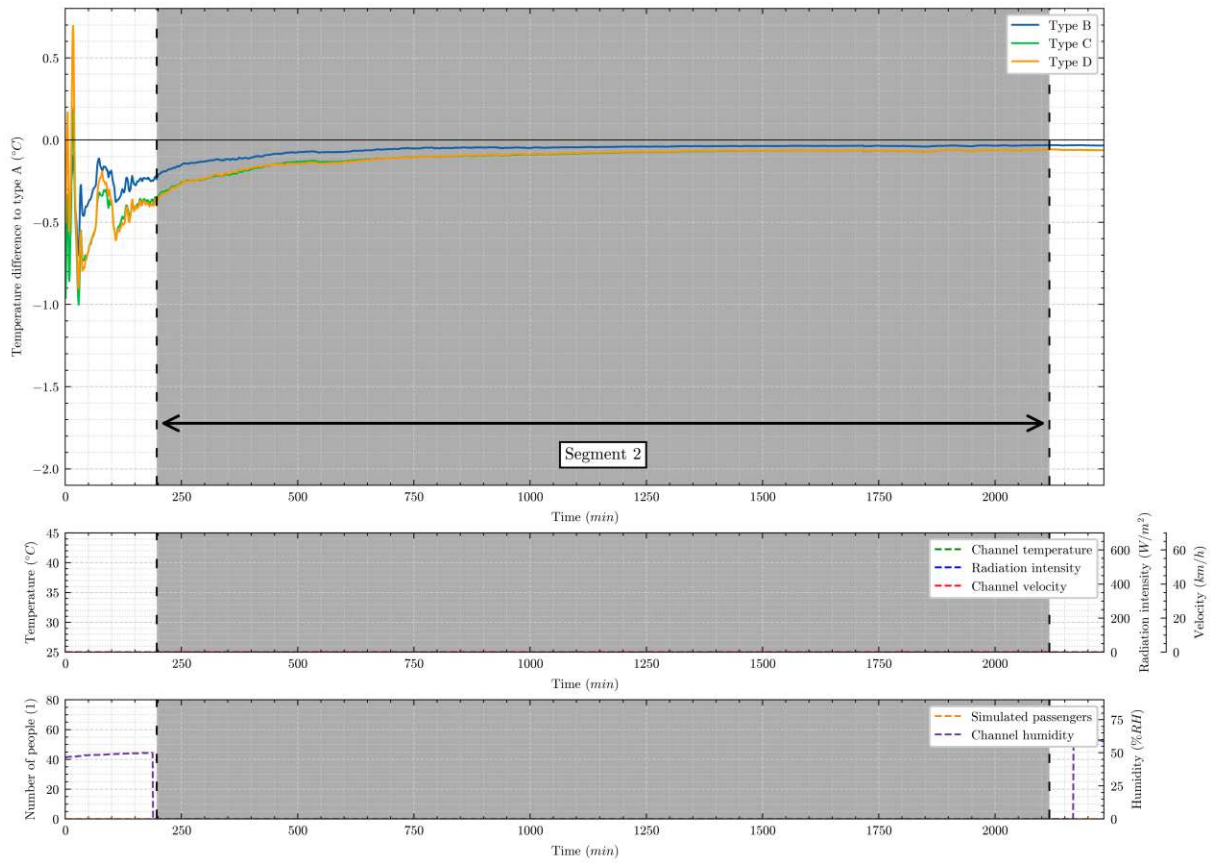
Figure A.2.: Temperature differences relative to the sensor type A over an extended undis-
turbed period.
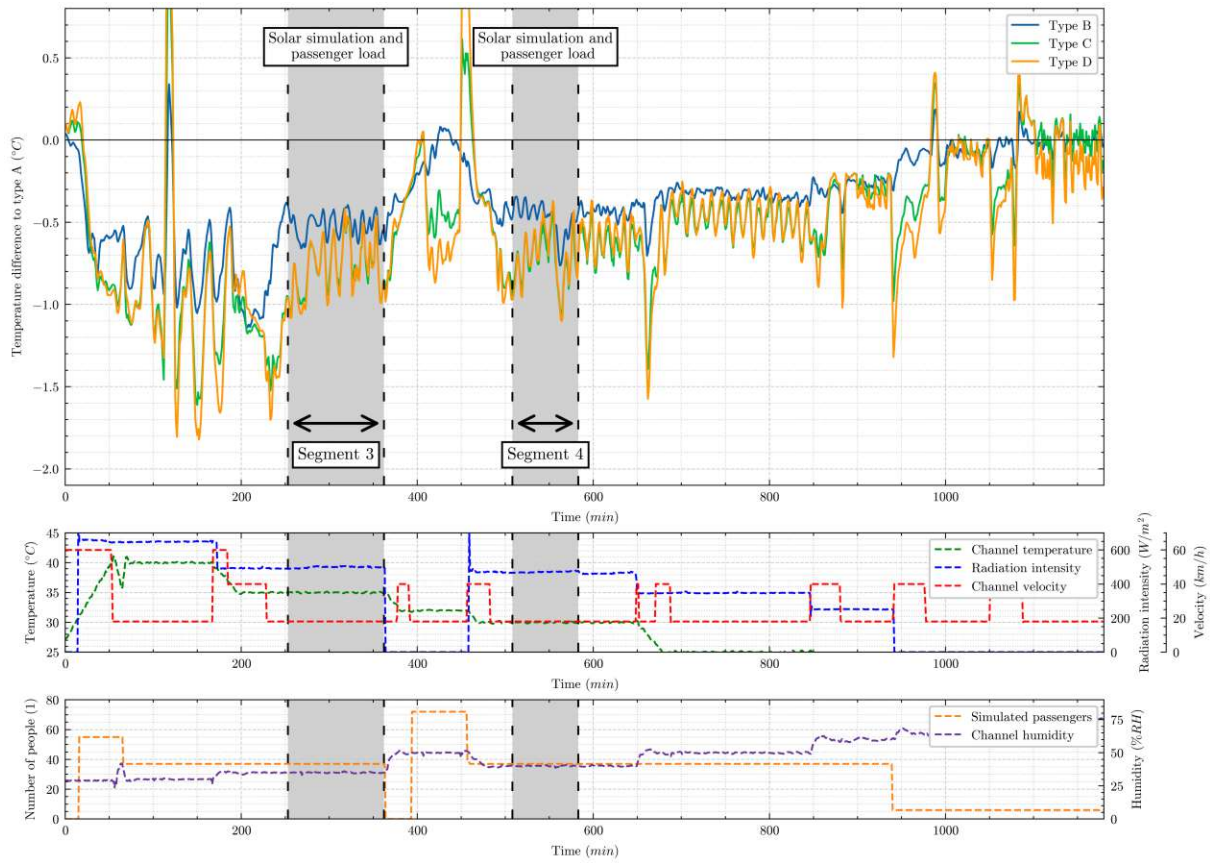
Figure A.3.: Temperature differences relative to the sensor type A during a measurement involving solar radiation and various door opening cycles.

A.1.2. Temperature curves of measurement place 1
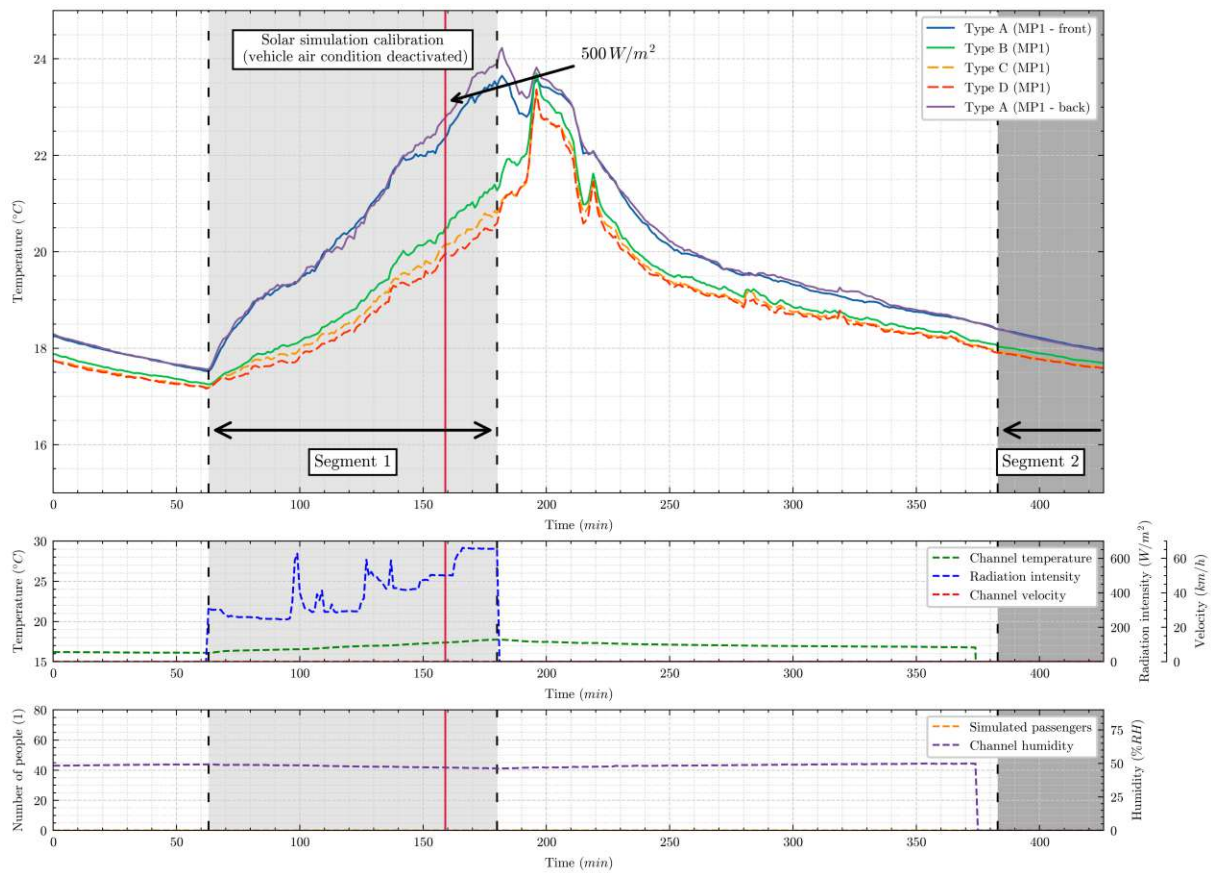
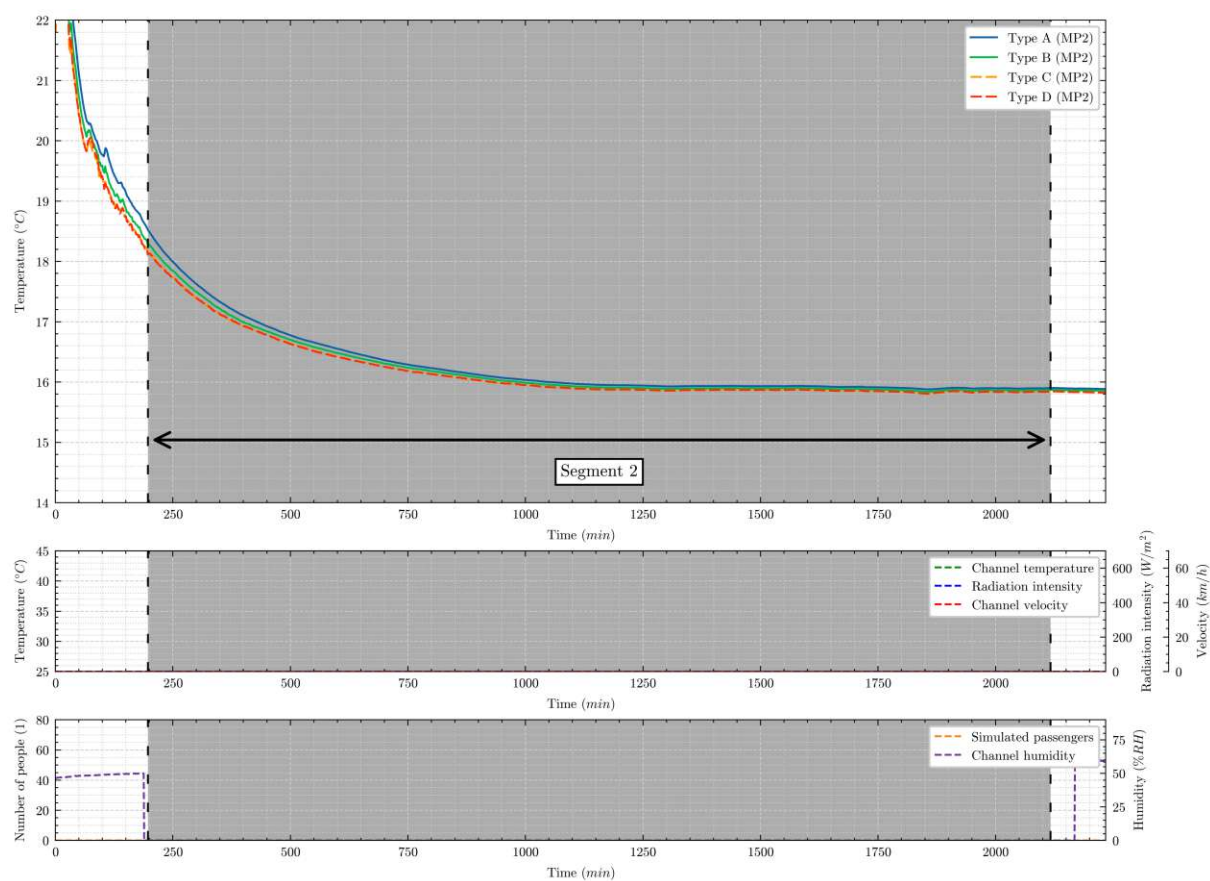Figure A.4.: Temperatures when the bus ventilation was deactivated.
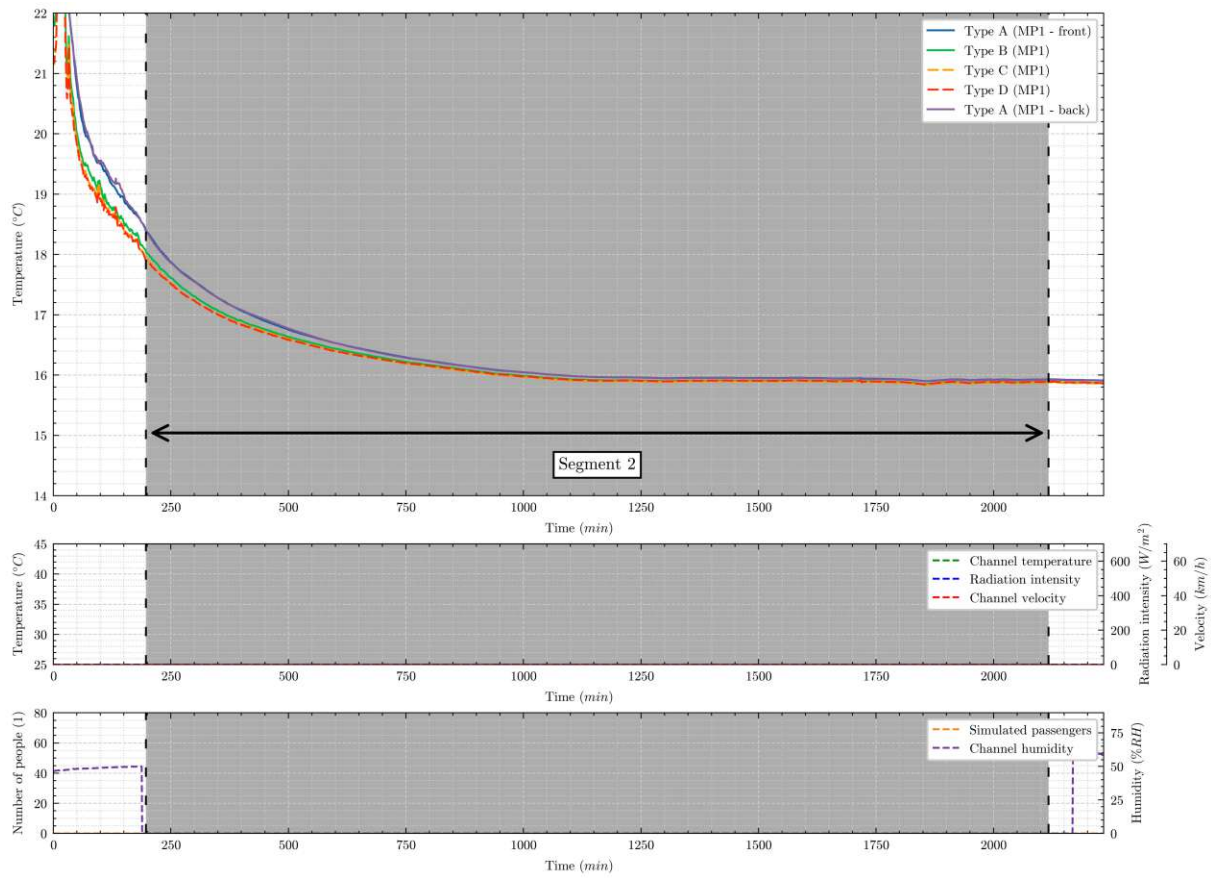
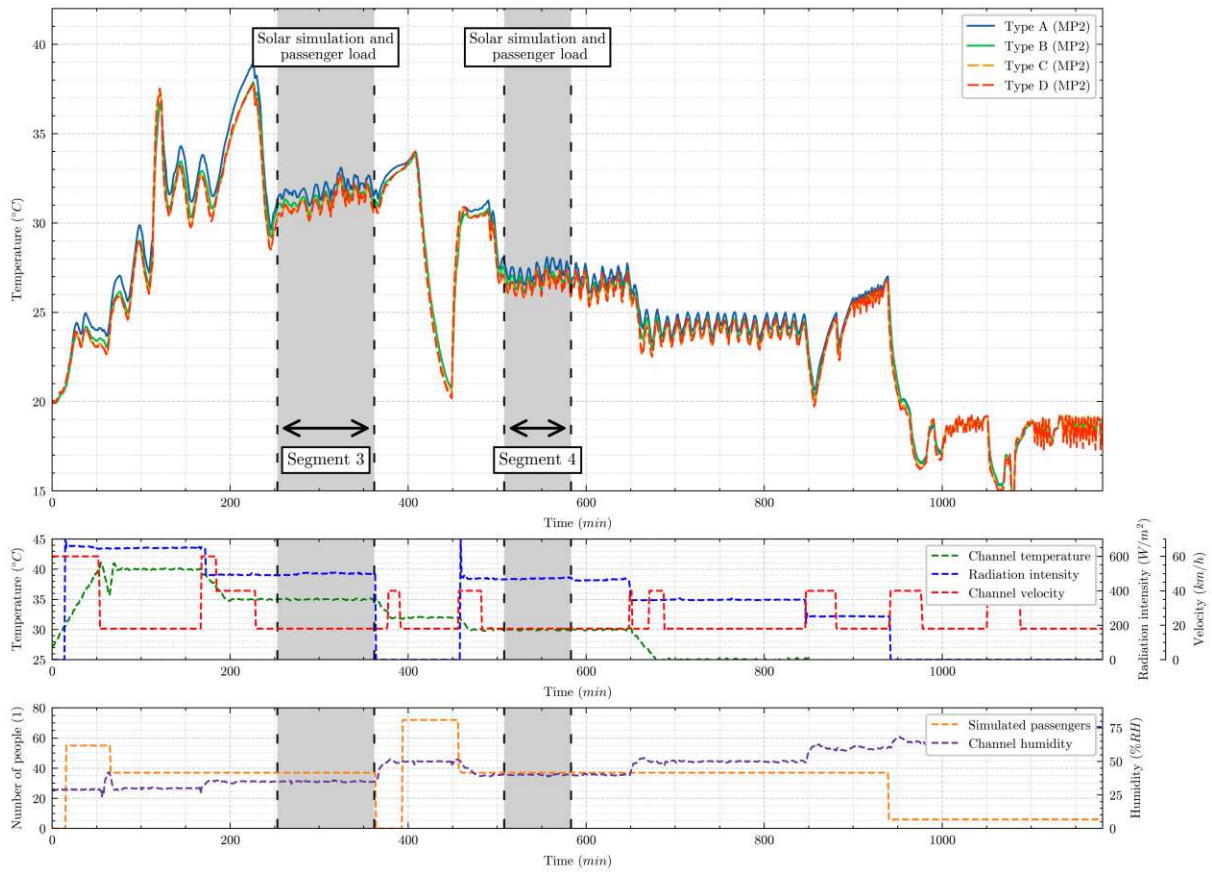Figure A.5.: Temperatures over an extended undisturbed period.
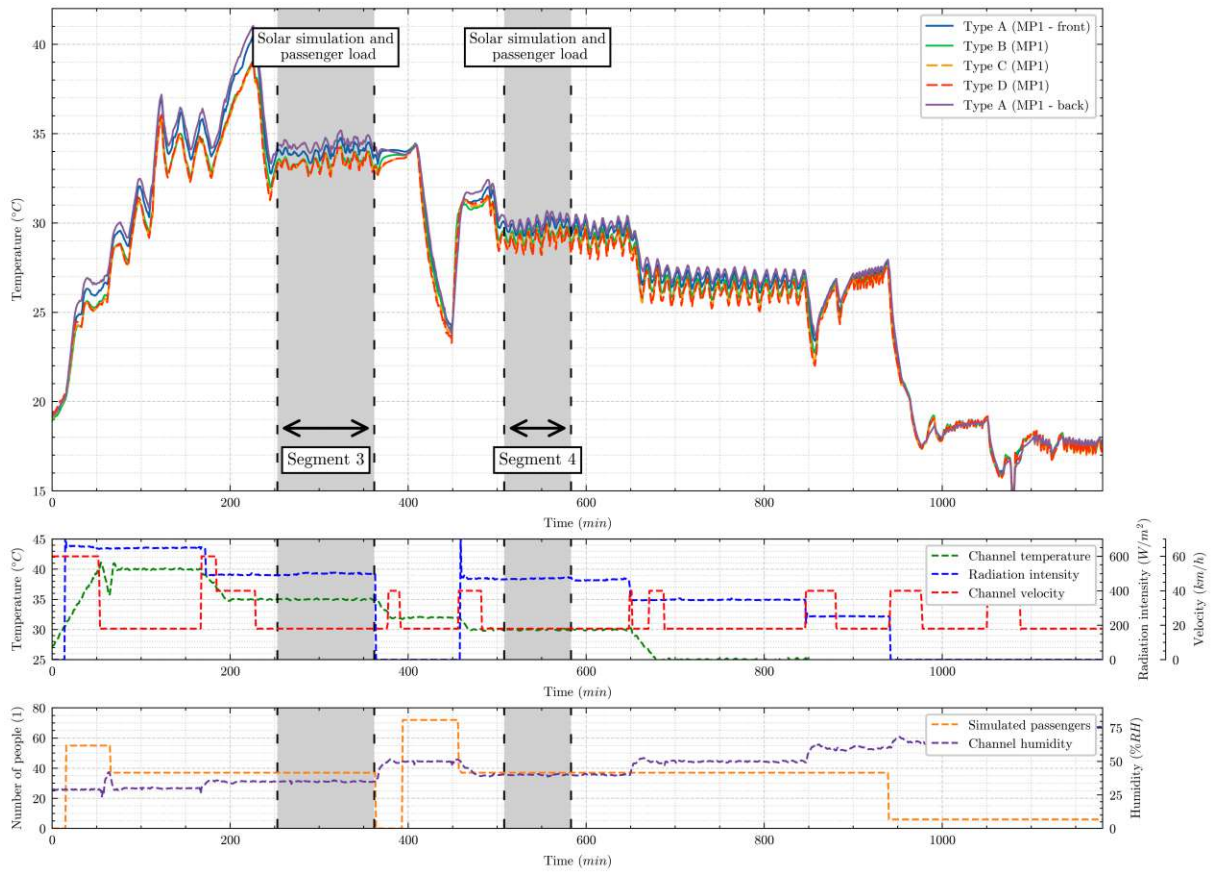
Figure A.6.: Temperatures during a measurement with various door opening cycles.

A.1.3. Temperature curves of measurement place 2
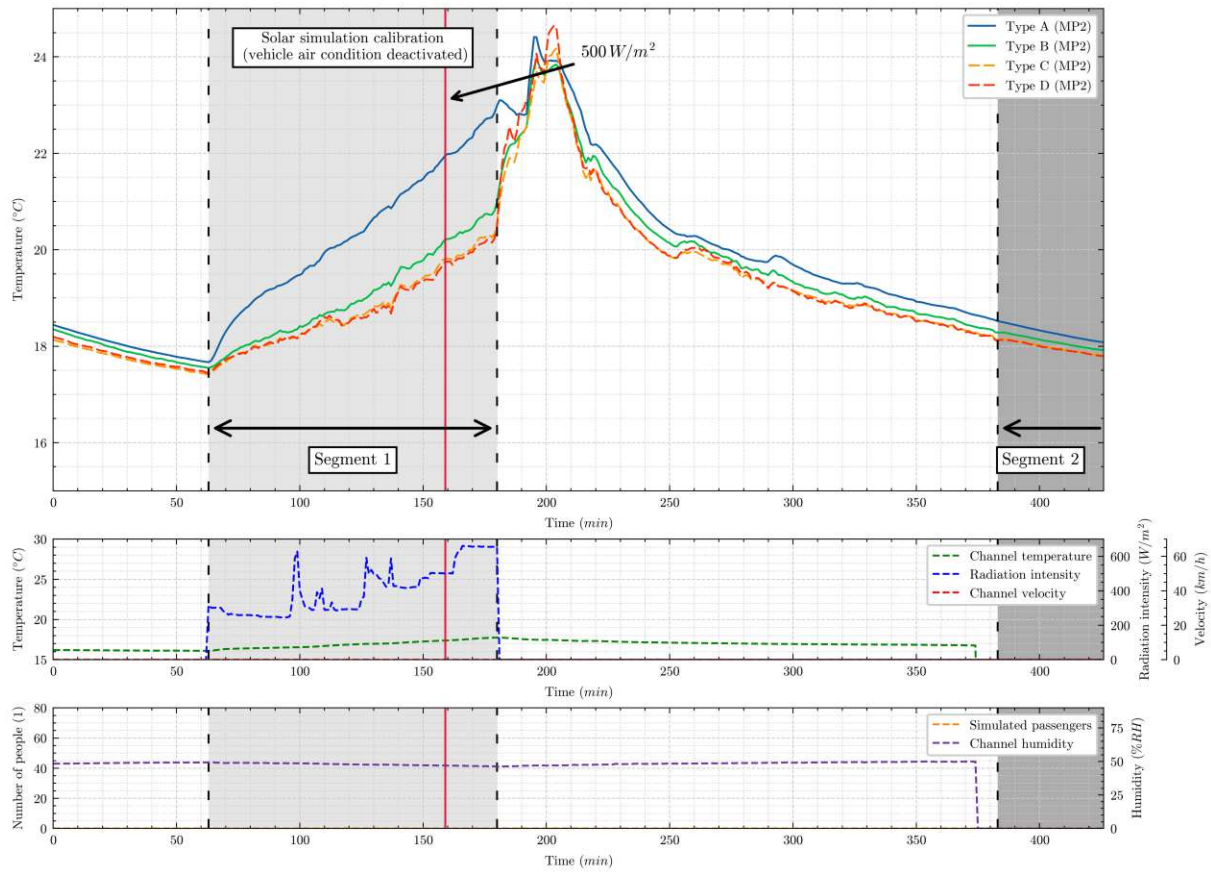
Figure A.7.: Temperatures when the bus ventilation was deactivated.

Figure A.8.: Temperatures over an extended undisturbed period.

Figure A.9.: Temperatures during a measurement with various door opening cycles.

A.2. Additional validation results from the rail vehicle

A.2.1. Segment 1 - segment 6: Various conditions
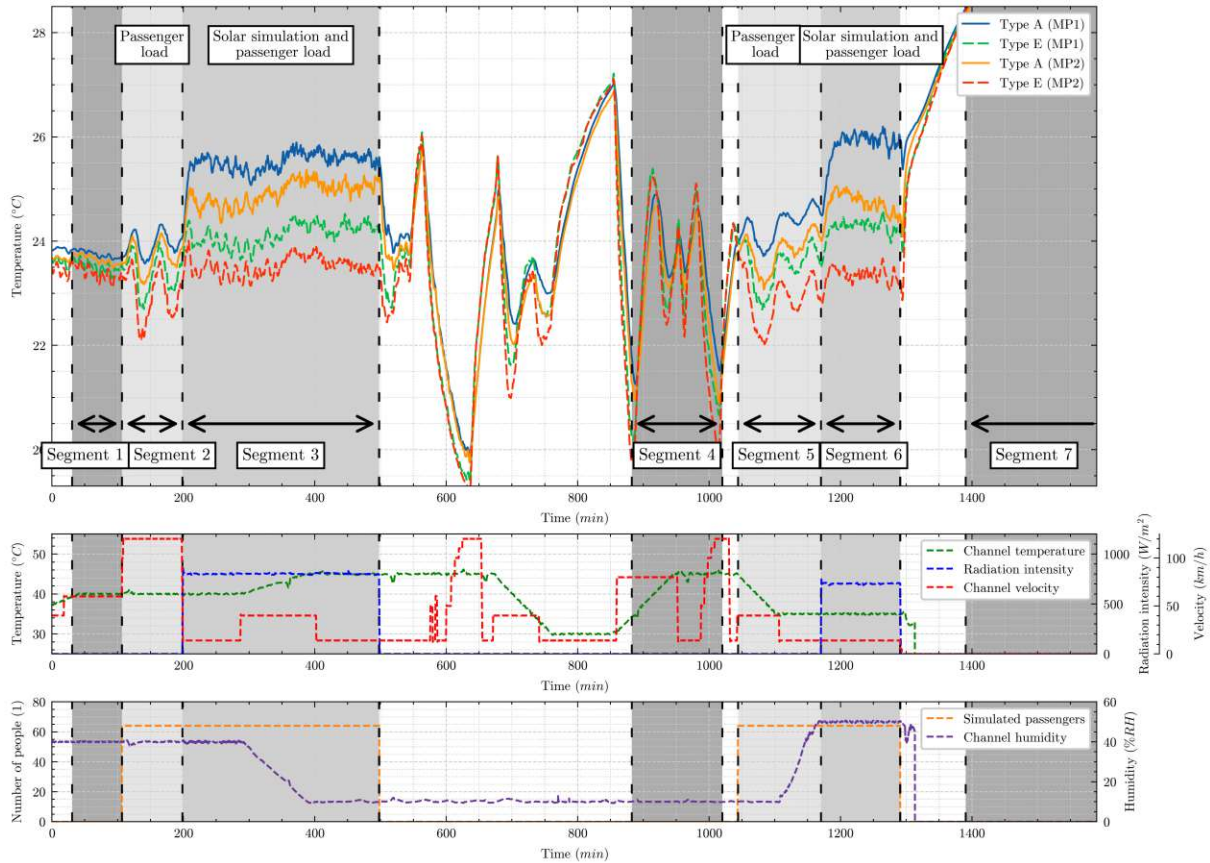
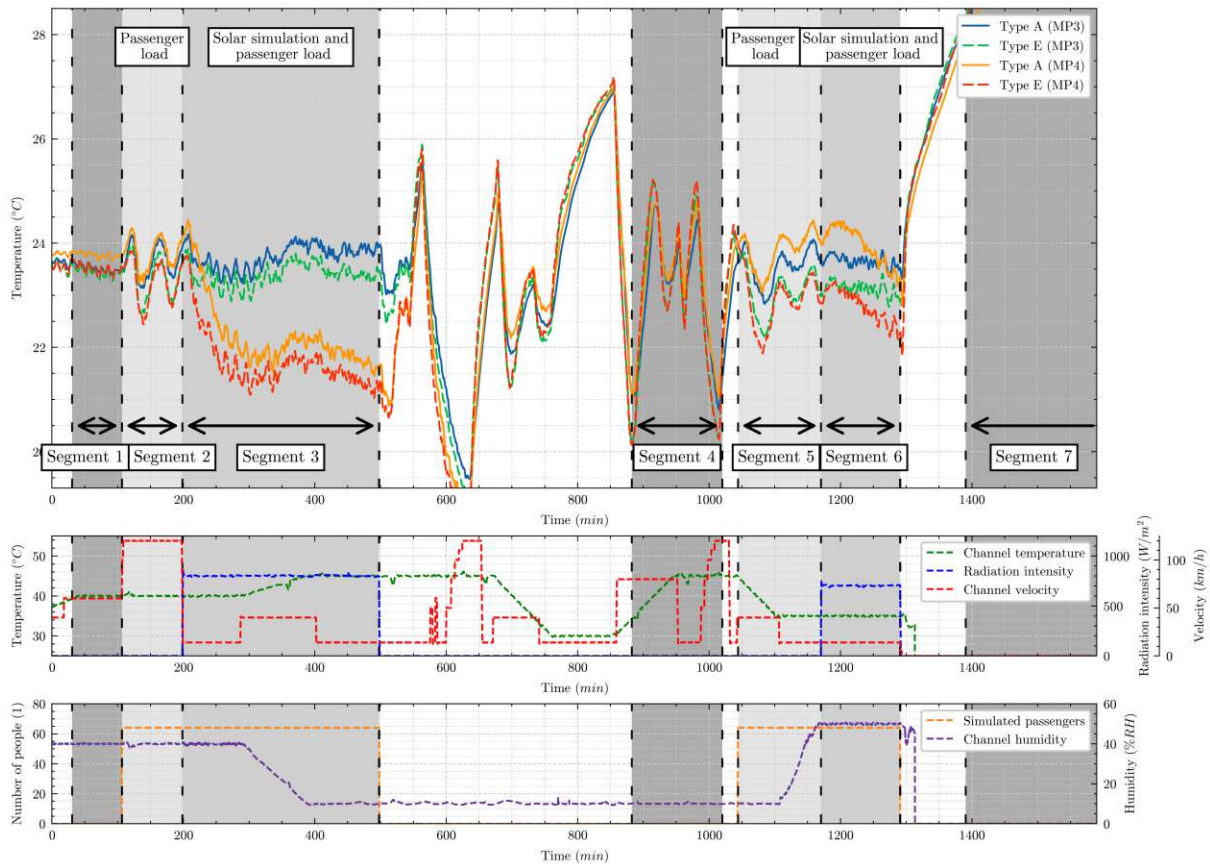Figure A.10.: Sensor temperatures at measurement places 1 and 2 during a typical test campaign.

Figure A.11.: Sensor temperatures at measurement places 3 and 4 during a typical test campaign.
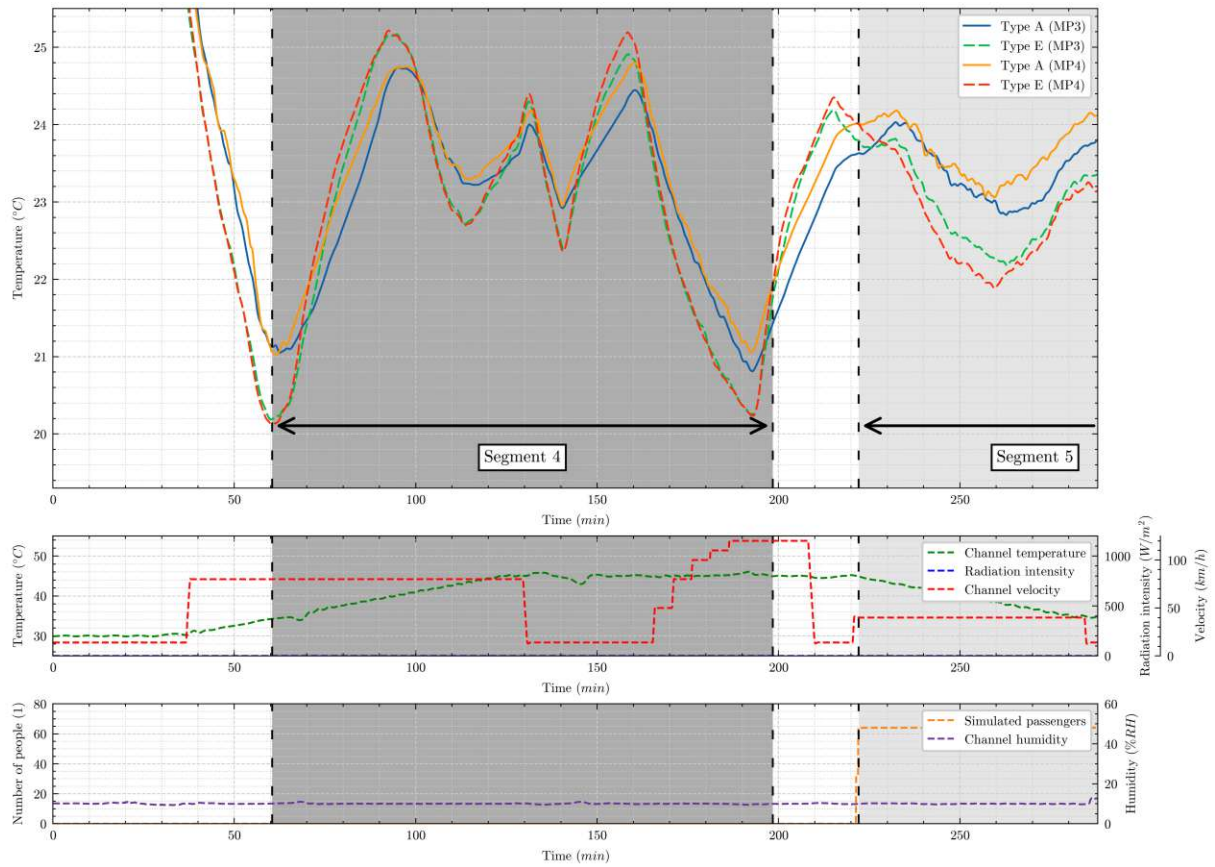
Figure A.12.: Sensor temperatures at measurement places 3 and 4 during a typical test campaign.

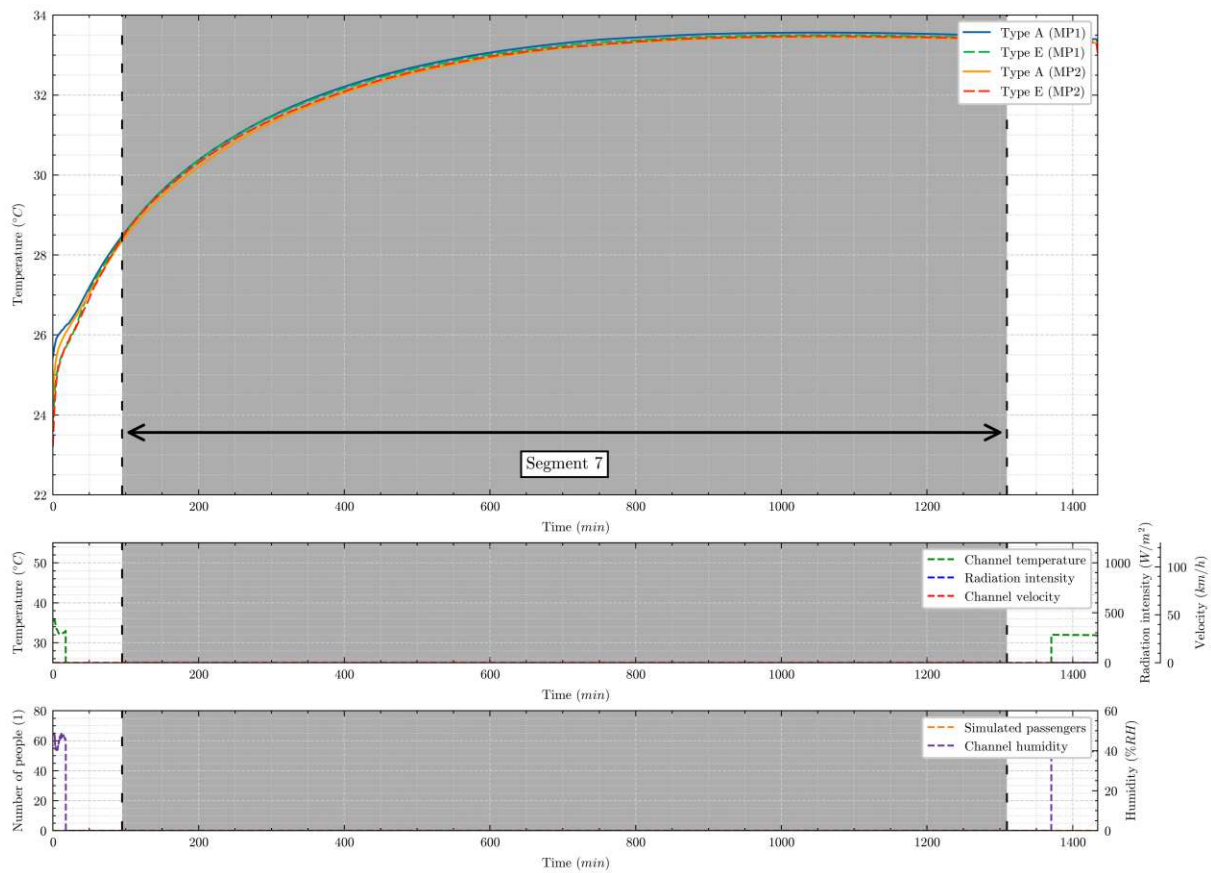## A.2.2. Segment 7: Switched off climatic wind tunnel

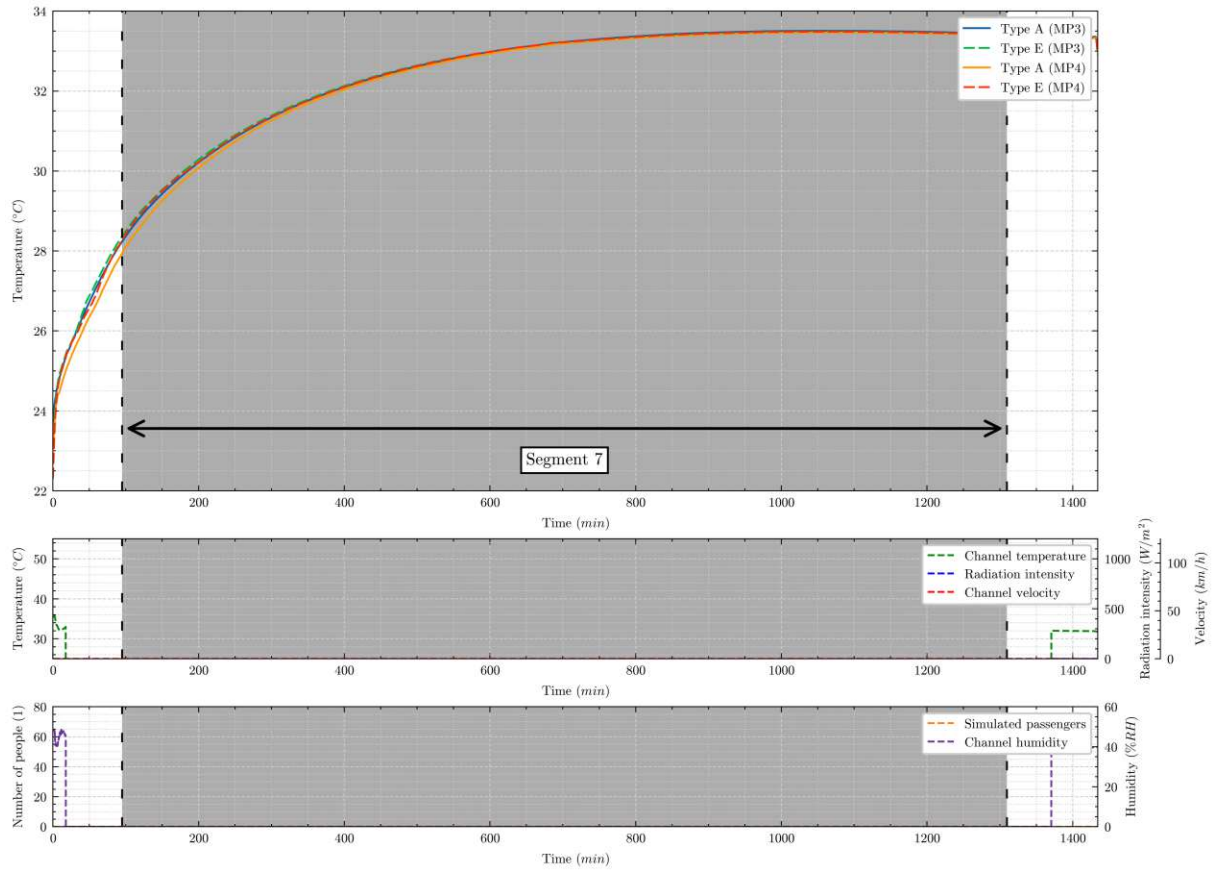Figure A.13.: Sensor temperatures at measurement places 1 and 2 during a typical test campaign.

Figure A.14.: Sensor temperatures at measurement places 3 and 4 during a typical test campaign.

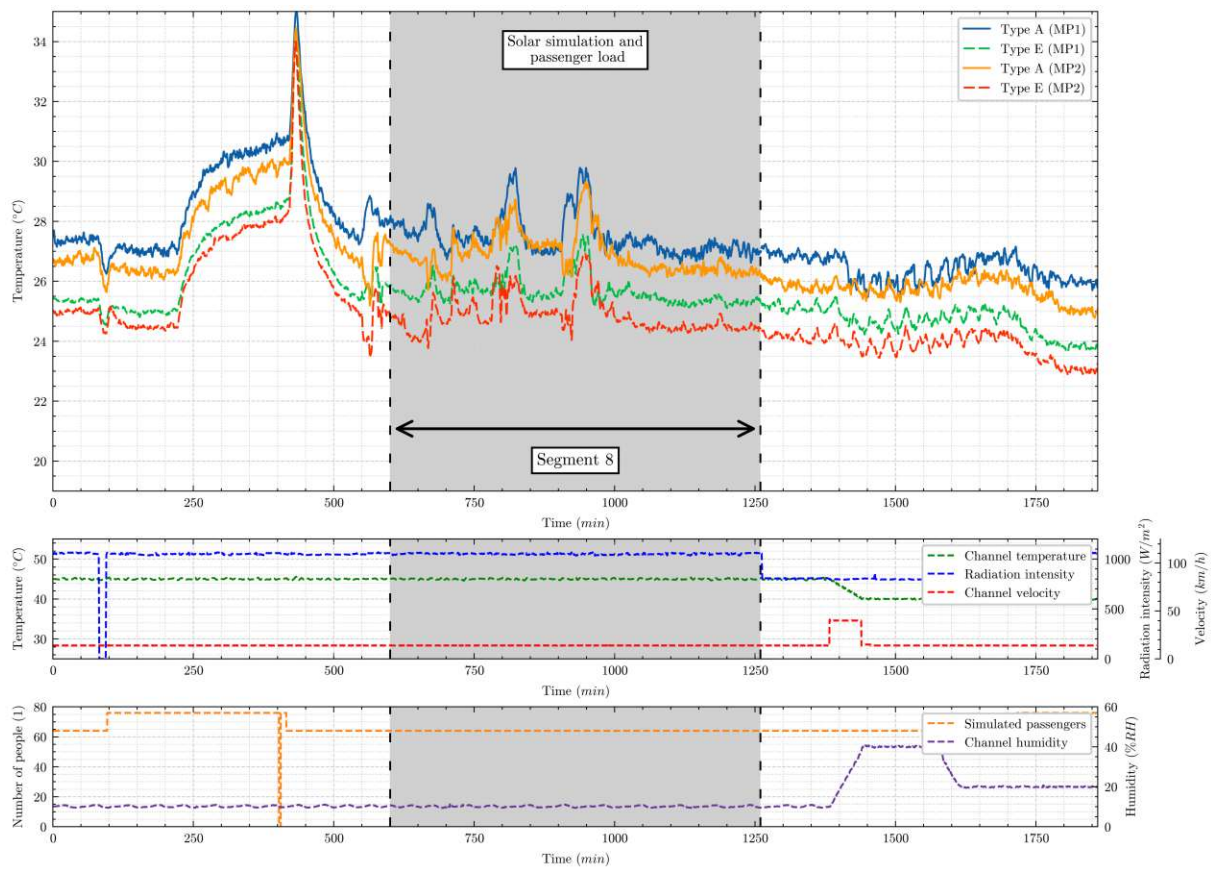## A.2.3. Segment 8: Radiation intensity of 1050 W/m^2

Figure A.15.: Sensor temperatures at measurement places 1 and 2 during a typical test campaign.
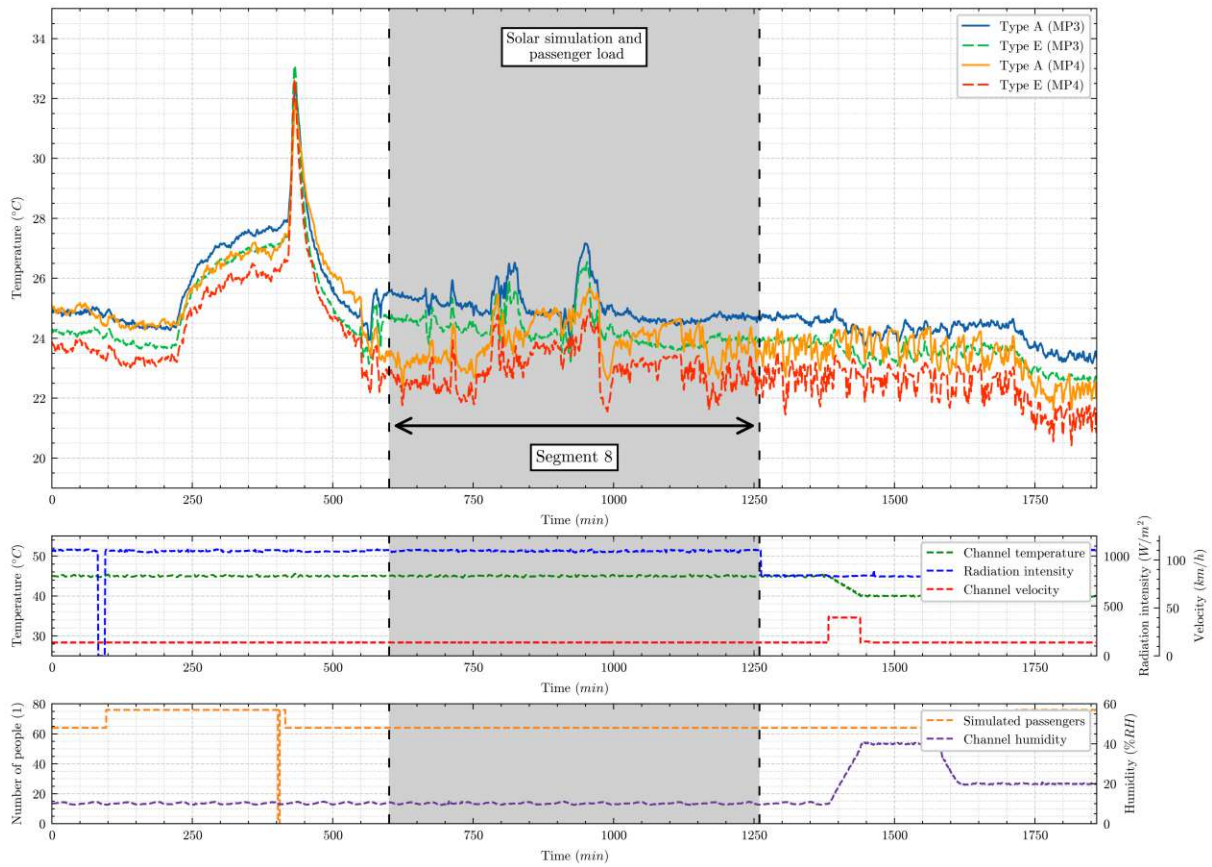
Figure A.16.: Sensor temperatures at measurement places 3 and 4 during a typical test campaign.

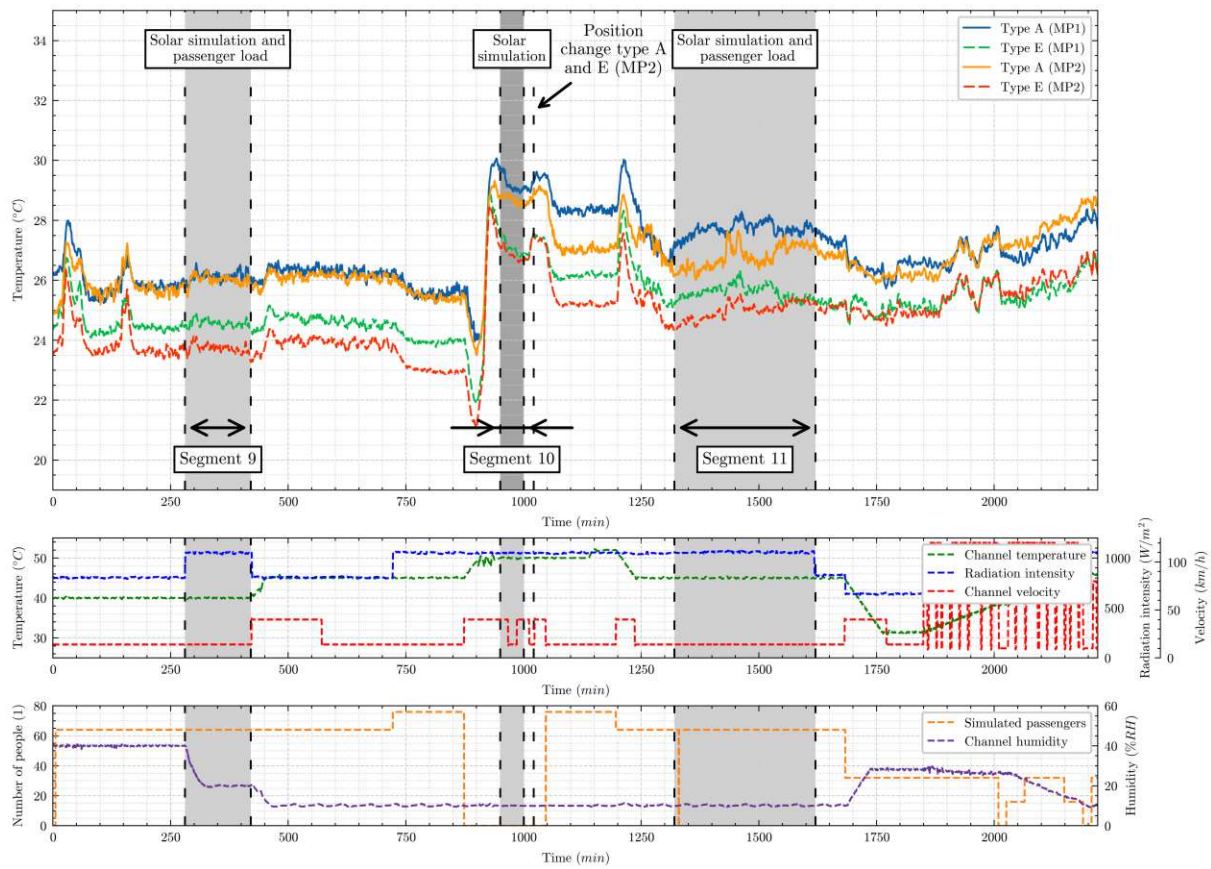## A.2.4. Segment 9 – 11: Position change of type A and E

Figure A.17.: Sensor temperatures at measurement places 1 and 2 during a typical test campaign.
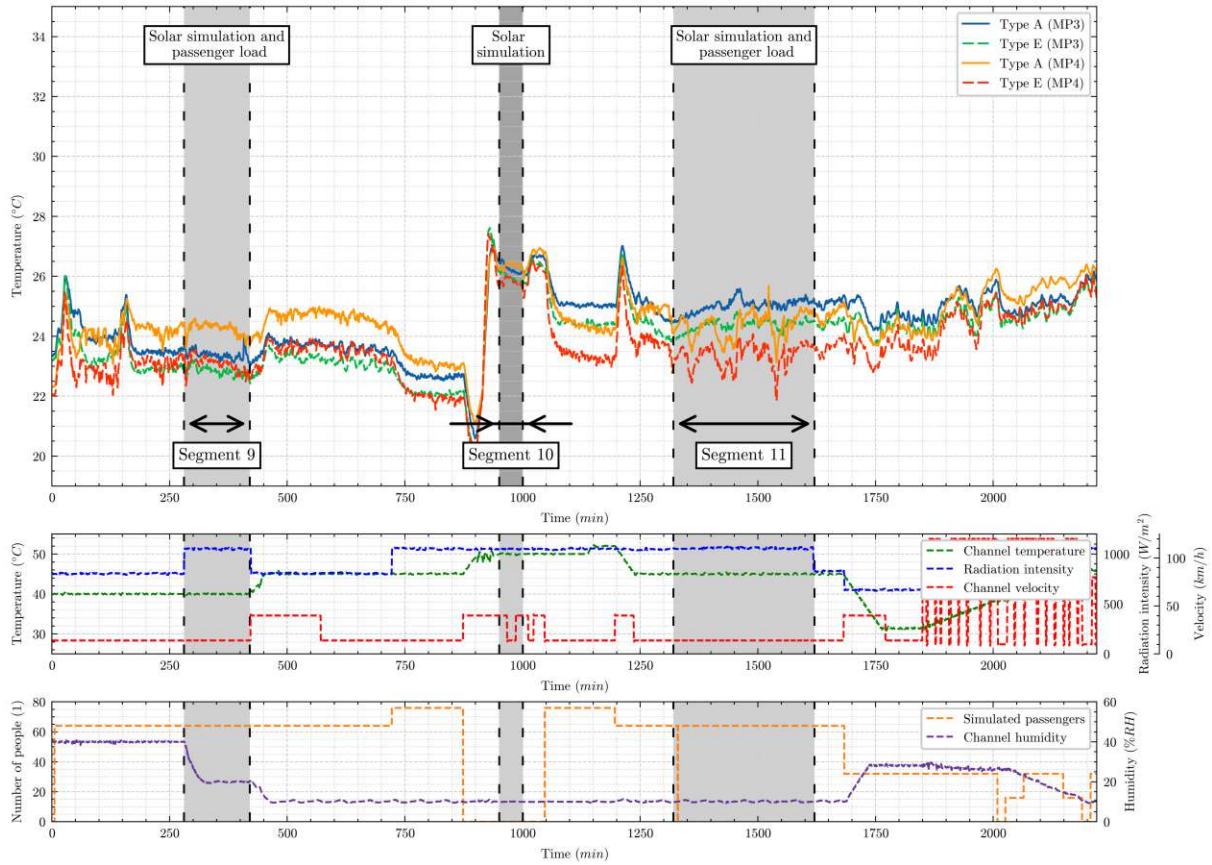
Figure A.18.: Sensor temperatures at measurement places 3 and 4 during a typical test campaign.

Bibliography

[1]   Hannah Ritchie. "Cars, planes, trains: where do CO_2 emissions from transport come from?" In: *Our World in Data* (2020). https://ourworldindata.org/co2-emissions-from-transport. (accessed: 25.10.2024).

[2]   Nadège Vetterli et al. "Energy efficiency of railway vehicles". In: *Proceedings of International Conference CISBAT 2015 Future Buildings and Districts Sustainability from Nano to Urban Scale*. LESO-PB, EPFL. 2015, pp. 955–960.

[3]   *EN 13129:2016: Railway applications - Air conditioning for main linerolling stock - Comfort parameters and type tests*. Standard. European Standard, Aug. 2016.

[4]   RTA Rail Tec Arsenal Fahrzeugversuchsanlage GmbH. *General Information and Guide for Customers*. 2023. URL: https://www.rta.eu/images/stories/pdf/IWT_Vienna_General_information.pdf. (accessed: 25.10.2024).

[5]   Lucas Tretthahn. "Investigation of influencing factors in the measurement of climatic conditions in rail vehicles and identification of optimisation potentials". Bachelor's Thesis. Vienna, Austria: Technische Universität Wien, Mar. 2024.

[6]   H.D. Baehr and K. Stephan. *Wärme- und Stoffübertragung*. Springer Berlin Heidelberg, 2019. ISBN: 9783662584415.

[7]   Martin Dehli, Ernst Doering, and Herbert Schedwill. *Grundlagen der Technischen Thermodynamik: Für eine praxisorientierte Lehre*. Feb. 2023. ISBN: 978-3-658-31726-3. DOI: 10.1007/978-3-658-31727-0.

[8]   Ludwig Prandtl. "Flüssigkeitsbewegung bei sehr kleiner Reibung". In: *International Mathematical Congress Heidelberg* (1904).

[9]   Verein deutscher Ingenieure. *VDI-Wärmeatlas*. Ed. by VDI e.V. 11th ed. VDI-Buch. Berlin Heidelberg: Springer, 2013. ISBN: 978-3-642-19981-3. DOI: 10.1007/978-3-642-19981-3.

[10] G. K. Batchelor. *An Introduction to Fluid Dynamics*. Cambridge Mathematical Library. Cambridge University Press, 2000.

[11] F. Durst. *Grundlagen der Strömungsmechanik: Eine Einführung in die Theorie der Strömung von Fluiden*. Springer Berlin Heidelberg, 2007. ISBN: 9783540313243.

[12] Hendrik Kuhlmann. *Strömungsmechanik Eine kompakte Einführung für Physiker und Ingenieure*. Pearson Deutschland, 2014, p. 304. ISBN: 9783868942538.

[13] Joel Ferziger, Milovan Perić, and Robert Street. *Numerische Strömungsmechanik*. Springer, Jan. 2020. ISBN: 978-3-662-46543-1. DOI: 10.1007/978-3-662-46544-8.

[14] Holm Altenbach. *Kontinuumsmechanik: Einführung in die materialunabhängigen und materialabhängigen Gleichungen.* Jan. 2018. ISBN: 978-3-662-57503-1. DOI: 10.1007/978-3-662-57504-8.

[15] Bengt Andersson et al. *Computational Fluid Dynamics for Engineers.* Cambridge University Press, 2011.

[16] ANSYS Inc. *Fluent Theory Guide.* English. Release 2024 R1.

[17] Y.L. Sinai. *Radiation Heat Transfer Modelling with Computational Fluid Dynamics.* CRC Press, 2022. ISBN: 9780367767884.

[18] Aytekin Duranay et al. "An experimental study on vortex-induced vibrations at TRSL2 and TRSL3 flow regimes". In: Jan. 2022.

[19] J.H. Lienhard. *Synopsis of Lift, Drag, and Vortex Frequency Data for Rigid Circular Cylinders.* Bulletin (Washington State University. College of Engineering. Research Division). Technical Extension Service, Washington State University, 1966.

[20] KM Sowoud, AA Al-Filfily, and B H Abed. "Numerical investigation of 2D turbulent flow past a circular cylinder at lower subcritical Reynolds number". In: *IOP Conference Series: Materials Science and Engineering.* Vol. 881. 1. IOP Publishing. 2020, p. 012160.

[21] Hongyi Jiang and Liang Cheng. "Large-eddy simulation of flow past a circular cylinder for Reynolds numbers 400 to 3900". eng. In: *Physics of fluids* 33.3 (2021). ISSN: 1070-6631.

[22] *EN 14750-1:2006: Railway applications - Air conditioning for urban and suburban rolling stock.* Standard. European Standard, June 2006.

[23] *EN 14813-1:2006+A1:2010: Railway applications - Air conditioning for driving cabs.* Standard. European Standard, Nov. 2010.

[24] *ISO 7726:2001: Ergonomics of the thermal environment – Instruments for measuring and monitoring physical quantities.* Standard. International Organization for Standardization, July 2001.

[25] Hans Dieter Baehr and Stephan Kabelac. *Thermodynamik : Grundlagen und technische Anwendungen.* ger. 16., aktualisierte Auflage. Lehrbuch. Berlin: Springer Vieweg, 2016. ISBN: 3662495678.

[26] *EN 13182:2002+AC:2002: Ventilation for buildings - Instrumentation requirements for air velocity measurements in ventilated spaces (including corrigendium AC:2002).* Standard. European Standard, July 2002.

[27] P.O. Fanger et al. "Air turbulence and sensation of draught". In: *Energy and Buildings* 12.1 (1988), pp. 21–39. ISSN: 0378-7788.

[28] Balazs Both, Zoltan Szantho, and R. Goda. "The problem of turbulence intensity measurement in comfort ventilation". In: *International Review of Applied Sciences and Engineering* 8 (June 2017), pp. 17–23.

[29] *DIN 41624: Tuchel Stecker*. Standard. Revised 1985. Berlin: Deutsches Institut für Normung e.V., 1964.

[30] electrotherm. *Gesamtkatalog*. Feb. 2024. URL: https://markt.technik-einkauf.de/wp-content/uploads/2015/01/Electrotherm-Gesamtkatalog.pdf.

[31] Vaisala. *GMP252 Carbon Dioxide Probe*. V2023. URL: https://docs.vaisala.com/v/u/B211567EN-G/en-US.

[32] *Datasheet Accessories*. v2.6. E+E Elektronik. Oct. 2023. URL: https://www.epluse.com/fileadmin/data/product/accessories/datasheet_accessories.pdf.

[33] TSI. *Air velocity transducer models 8455, 8465, AND 8475*. 2012. URL: https://tsi.com/getmedia/9b666e21-75c9-440c-afe6-da9a58f1e526/8455-65-75-AVT-A4_5001013-UK?ext=.pdf.

[34] *Connectors for frequencies below 3 MHz - Part 9: Circular connectors for radio and associated sound equipment (IEC 60130-9:2011)*. Tech. rep. European Standard, Dec. 2011.

[35] MatWeb. "Material Property Data". 2024. URL: https://www.matweb.com/index.aspx. (accessed: 25.10.2024).

[36] Robert Vaughn Morgan et al. *Emissivity Measurements of Additively Manufactured Materials*. Tech. rep. Jan. 2017.

[37] The Engineering ToolBox (2003). *Surface Emissivity Coefficients*. 2024. URL: https://www.engineeringtoolbox.com/emissivity-coefficients-d_447.html. (accessed: 25.10.2024).

[38] ANSYS Inc. *Fluent User's Guide*. English. Release 2024 R1.

[39] RTA Rail Tec Arsenal Fahrzeugversuchsanlage GmbH. "Aufstellung von Messunsicherheiten der Prüfmittel und deren Anwendung". June 2024.